Multifunctional Ferroelectrics based Devices for Next Generation RF Front-ends

By

Suhyun Nam

A dissertation submitted in partial fulfillment
of the requirements for the degree of
Doctor of Philosophy
(Electrical and Computer Engineering)
in the University of Michigan
2024

Doctoral Committee:

Professor Amir Mortazawi, Chair
Assistant Professor Aline Eid
Associate Professor John Heron
Professor Zetian Mi

Suhyun Nam

suhyunn@umich.edu

ORCID iD: 0000-0001-6161-7459

DEDICATION

To my parents and sister, who have provided nothing but unconditional love and support.

ACKNOWLEDGEMENTS

Throughout my Ph.D. studies I have been fortunate to interact, meet, and forge friendships with a number of individuals in the University of Michigan academic community. I would like to take this opportunity to acknowledge and express my gratitude for them. As I have mentioned privately to many of my close friends, one of the most critical aspect that helped me reach this point was the backing of a strong support group.

First and foremost, I would like to express my sincerest gratitude to my advisor, Professor Amir Mortazawi, for his support and undying diligence to the pursuit of research. Like any advisor-student relationship, his continuous guidance, patience, and unique ways of encouragement are the reason that I am here today, and I consider myself fortunate to be one of his students. The work I have accomplished would not have been possible without his guidance, and I feel honored to have learned how to conduct independent research under his mentorship. Furthermore, I am deeply thankful for my thesis committee members. I extend my gratitude to Professor Zetian Mi for our collaborative efforts with Dr. Ding Wang in the DARPA Compact Front-end Filters at the ElEment-level (COFFEE) program. Their insight and suggestions throughout the program were remarkably accurate and integral to achieving our results. I would also like to thank Associate Professor John Heron and Assistant Professor Aline Eid for their valuable, insightful comments that greatly contributed to enhancing the quality of this thesis.

Moreover, I would like to thank the members of Professor Mortazawi's research group. I would like to first extend my appreciation to Wenhao Peng, who diligently collaborated with me

across multiple conference and journal publications. We worked hand-in-hand, enduring innumerable late nights and early mornings in the Lurie Nanofabrication facilities and Radiation Laboratory (Radlab) office. Additionally, my deepest gratitude goes to my friend, Dr. Milad Koohi, whose valuable discussions not only centered about research but also encompassed life during my initial years of pursuing my PhD. I also want to extend thanks to Abdullah Alothman, Hersh Desai, and Andrew Devries, with a gentle, but firm reminder to Andrew Devries that the Buffalo Bills might not exactly be considered a good football team. I would also like to acknowledge the cleanroom staff in the Lurie Nanofabrication facilities, who have helped me immensely through multiple fabrication processes, tool issues, and general questions. Furthermore, my gratitude extends to my fellow graduate student friends, not only within the Radlab but throughout the University of Michigan. Their support during both the best and toughest times has been immensely valuable to me.

Finally, I want to express my heartfelt appreciation to my beloved older sister, who was the first person to (in a somewhat forceful manner) motivate me to pursue a Doctor of Philosophy in electrical engineering. I could not foresee a world without her nagging, pep talks, strict and unfiltered sibling advice, etc. that has made me the person I am today. I am incredibly proud of her equal pursuit of a PhD in marketing at the Harvard Business School. However, as her sibling, I must remind her that her younger brother is obtaining his degree first. Additionally, I extend my thanks to my parents, both of whom provided unwavering love and support throughout this journey.

TABLE OF CONTENTS

LIST OF TABLES

LIST OF FIGURES

ABSTRACT

Wireless communications, now within its fifth generation (5G), aims to attain connectivity across billions of devices, transcending geographical barriers and fostering advancements across various domains, such as healthcare, manufacturing, and transportation. However, this advancement presents challenges, notably the necessity to accommodate for numerous radio frequency (RF) bands, especially within the overcrowded sub-6-GHz spectrum. Moreover, there is further development toward incorporating millimeter-Wave (mm-Wave) frequencies for high-speed communication. Current RF front-end designs, already complex with over 100 filters and switchplexers, encounter limitations in accommodating these new frequencies within the confined space of mobile devices, demanding innovative solutions.

This dissertation presents designs of acoustic wave resonators based on two different multifunctional ferroelectric materials: Barium Strontium Titanate ($Ba_xSr_{1-x}TiO_3$, BST) and Scandium Aluminum Nitride ($Sc_xAl_{1-x}N$, ScAlN), in order to address different aspects of filter limitations. The first, BST, is employed in the design of ferroelectric based reconfigurable filters that require no external switches to transition between different bands of interest, specifically in the sub-6 GHz. As modules sizes continues to shrink, utilizing filters that are capable of multiple functions provide significant reduction in the overall complexity, cost, and size of the RF front-end. The second material, ScAlN, is employed to overcome frequency scaling challenges of current bulk acoustic wave (BAW) technology. By employing MBE grown film in a multilayer structure, a novel mm-Wave acoustic resonator with validation of polarization switching in the ScAlN layer is presented. Contribution of this work are categorized into three major parts.

First, BST thin film bulk acoustic wave resonators (FBARs) are employed to design intrinsically switchable filters based on electrostrictive transduction. As a proof-of-concept, a systematically designed switchless, quad band acoustic wave filter bank with the lowest insertion loss to date in the literature is fabricated and measured. The filter bank is capable of switching between frequency bands of interest solely through a direct current (DC) bias applied across the associated BST FBARs and demonstrates its capability to streamline future radio systems.

Beyond switching on and off the filter response, the second contribution employs BST's electrostriction effect in a hybrid-based approach to develop filters with the capability to alter their transfer function. The use of reconfigurable frequency-selective components along the RF front-end is highly attractive, as the same component potentially supports functionality across multiple different bands. For the first time, two designs of reconfigurable RF circuits on the BST-on-Si platform (bandstop to an all-pass response and bandpass to all-reject response) are experimentally validated at significantly higher operational frequencies than previously published results at the time. Moreover, this hybrid approach offers a method to attain fractional bandwidth (FBW), not limited to the inherent coupling of the associated resonators.

The final part of this work incorporates thin film ferroelectric ScAlN in the design of a novel mm-Wave higher order mode FBAR. Selective excitation of multiple eigen modes within a multilayer FBAR structure through alternating configurations of positive and negative piezoelectricity (AlN and ScAlN, respectively) is highly advantageous compared to single layer BAW devices, which suffer from increased losses and reduced performance (quality factor, Q, and electromechanical coupling coefficient, k_t^2) with increased operating frequency. For the first time, a composite trilayer piezoelectric-ferroelectric-piezoelectric AlN-ScAlN-AlN FBAR exciting a third order thickness-extensional mode is demonstrated. To the author's knowledge, this is the first

published work that demonstrates complete ScAlN polarization switching within a composite structure. The reported k_t^2 does not follow the same roll-off as typical BAW devices when transitioning between fundamental and third mode, and such resonators can be incorporated in the design of mm-Wave filters with greater FBW requirements.

Chapter 1

Introduction

1.1. Dissertation Motivation

It is evident that wireless communications have continuously impacted and bolstered functionalities not only in everyday lives but across a number of societal sectors, ranging from

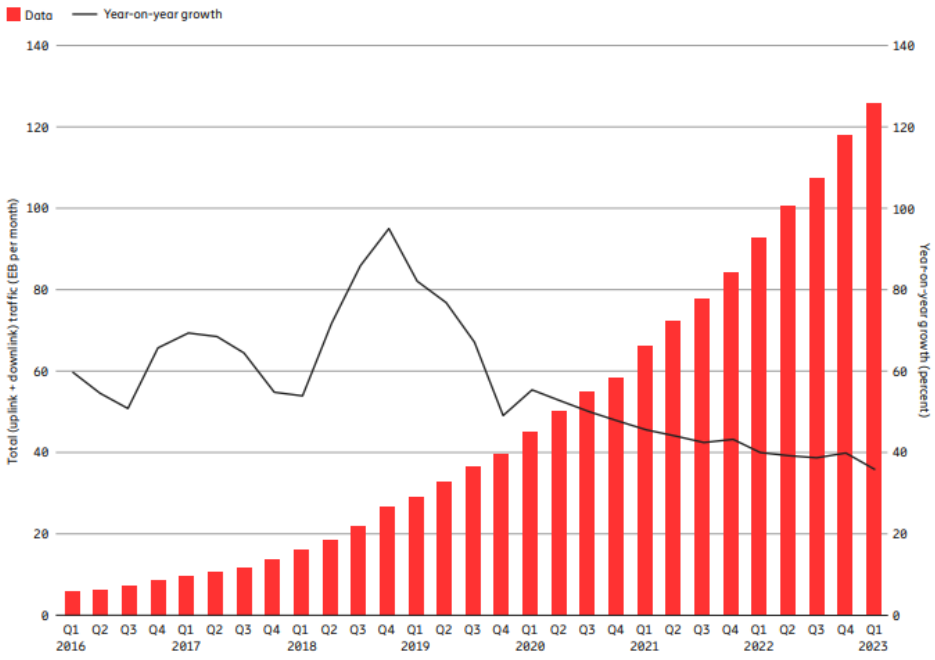

Fig. 1.1: Ericsson traffic measurements as of Q1 2023, which demonstrates the constant year-on-year growth of 40%, as of recently [1].

health care, manufacturing, to transportation with autonomous vehicles. A report conducted by Ericsson states that by the end of 2023, fifth-generation (5G) mobile subscriptions are anticipated to reach 1.5 billion, with mobile network traffic almost doubling in the past two years; within 5 years, it is expected that 5G networks will account for all mobile data growth [1]. The continuous increase in 5G adoption and its associated applications demonstrate a trend towards massive connectivity, low latency, greater network capacity, and higher data rates. To accommodate for these developments, the current radio frequency (RF) front-end in mobile devices requires

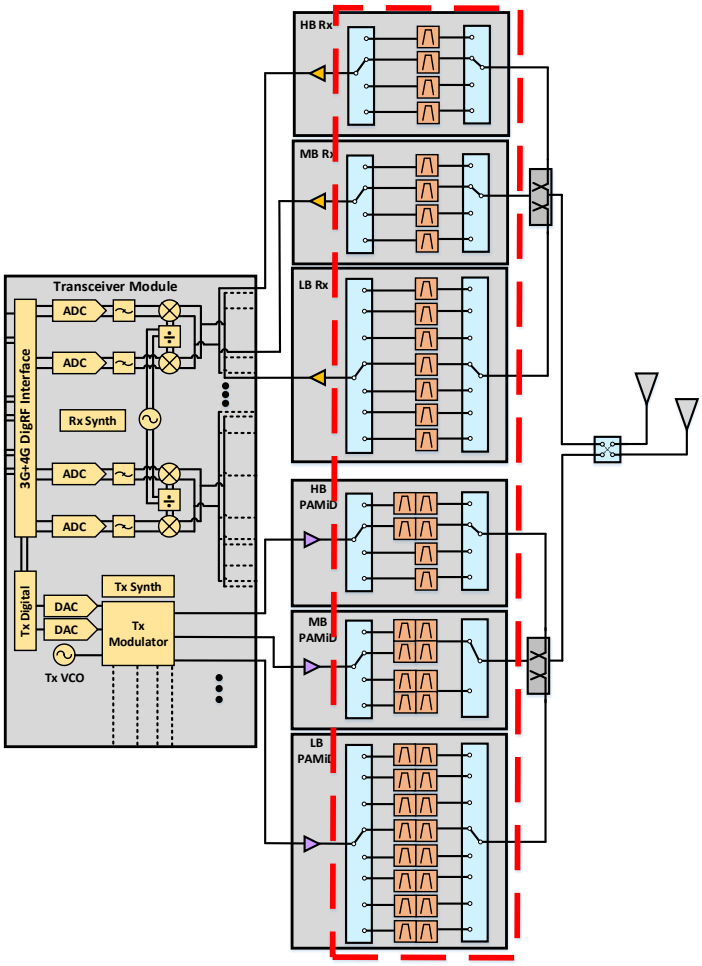

Fig. 1.2: Typical RF front-end for today's mobile devices requiring tens of filters and switchplexers (highlighted in the red dashed box) for their operation.

transformative modifications in order to support the number of services realized in 5G networks and beyond.

In its present state, the RF front-end in end-user wireless devices handles various wireless technologies (i.e. Wi-Fi, Bluetooth, GPS, 3G, 4G, etc.) through a number of fixed frequency filters and switch matrixes (switchplexers). Fig. 1.2 illustrates a block diagram of a typical RF front-end, where there are over 100 filters and switch matrices required to support all the designated bands of interest. To date, the main filter technology utilized within many wireless communication systems employs piezoelectric based filters utilizing surface acoustic wave (SAW) and bulk acoustic wave (BAW) resonators with BAW being the technology of choice for higher frequency operation. There is no other competing filter technology that is capable of meeting all the stringent requirements for mobile wireless communication systems in the sub-6 GHz regime, such as low insertion loss and steep roll off, miniature size, and large fractional bandwidth (FBW). Transitioning into 5G communications however, the design challenges along the RF front-end are twofold. Firstly, there is an exponential increase in the number of combinations of frequency bands and multiplexing methods; therefore, a solution to support these bands aside from incremental additions of acoustic filters and switches in an already limited hardware space is required.

Moreover, the pursuit of greater BW and faster data rates has led to a congested sub-6 GHz spectrum, leaving limited room for the expansion of 5G systems. Resultingly, as shown in Fig. 1.3, allocation of new frequency bands within the 24 GHz – 100 GHz offer the highest potential for supporting demands for greater data rates [2]. However, attempts to scale conventional BAW devices to millimeter wave frequencies leads to a number of issues: 1) smaller resonators area leading to higher dissipated power in a device, and 2) thinner membranes introducing reliability and processing challenges, leading to reduced quality factor (Q) and electromechanical coupling

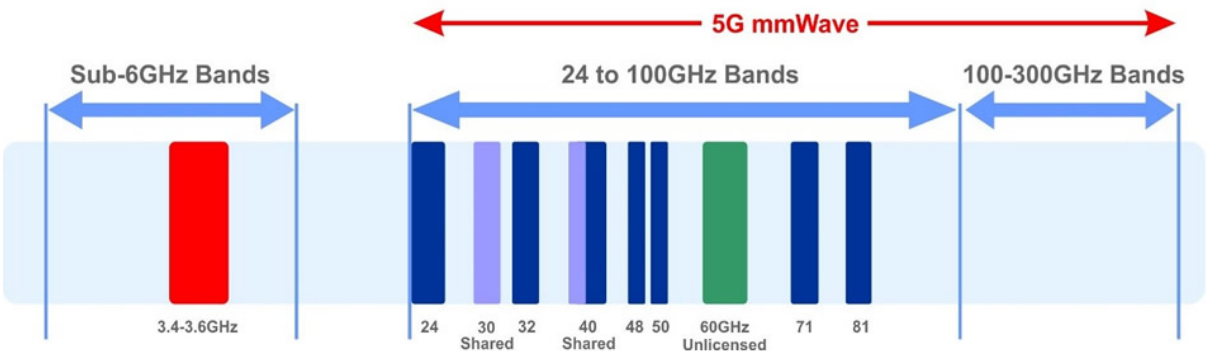

Fig. 1.3: Overview of 5G mm-Wave bands, courtesy of [2].

coefficient (k_t^2) (due to increased negative impact of the electrode/piezoelectric interface from the dead layer, surface roughness) [3]-[7]. Development of new filter technologies that not only provide high performance up to millimeter waves without exasperating RF front-end complexity is of paramount importance for future wireless systems. The next section provides background on ferroelectrics and highlights the advantages of integrating ferroelectrics within RF front-ends.

1.2. Overview of Ferroelectric Films

As shown in Fig. 1.4, ferroelectrics are well-known for their unique property of spontaneous and reversible electric polarization. When an external electric field is applied that is sufficiently high, referred to as the coercive electric field (E_c), the ferroelectric material polarizes to a certain direction. Under a zero bias, this polarization is referred to as the remanent polarization, P_r. As ferroelectric retain their polarization state (P_r or $-P_r$), depending on the history of electric field bias applied to the film, it can be exploited within nonvolatile memory applications, where the two stable polarization states represent different bits of information [8]. It must be noted that the application is dependent on the phase of the ferroelectric material; for memory cells, the ferroelectric is in its polar phase. As will be discussed, other electrical properties of ferroelectrics,

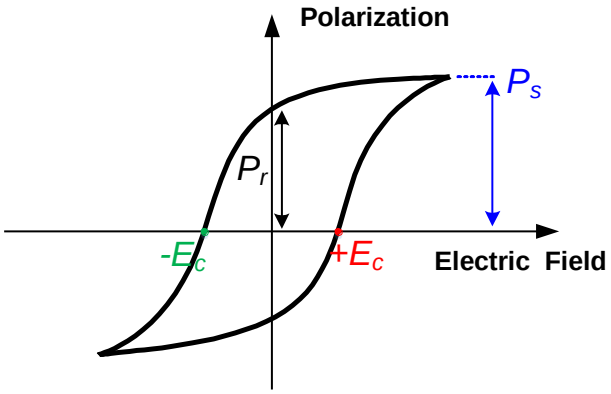

Fig. 1.4: Polarization versus Electric field and hysteresis loop for a ferroelectric material.

such as BST, utilize the nonpolar (paraelectric) phase due to low loss [9]. However, ferroelectrics

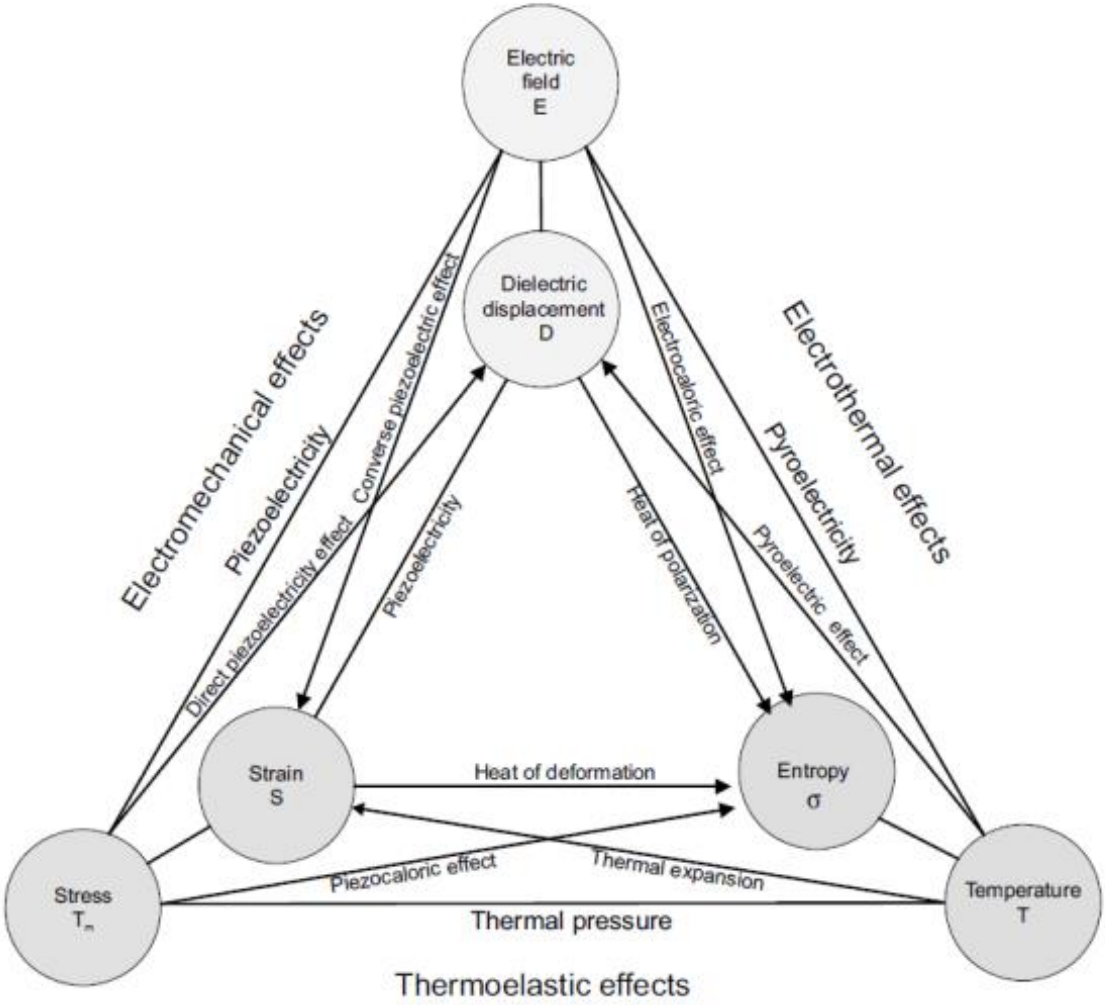

Fig. 1.5: The Heckmann diagram, reproduced from [10].

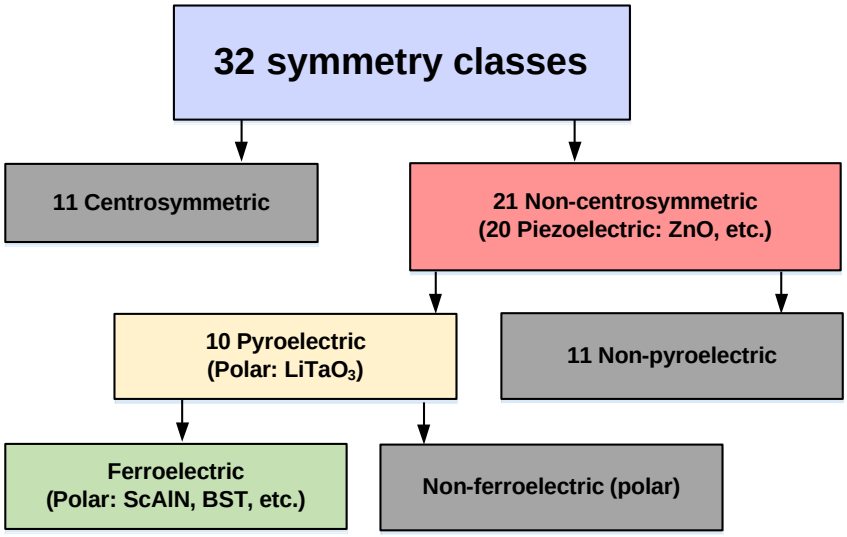

Fig. 1.6: Classification of materials, reproduced from [11].

are also a subset of piezoelectric and pyroelectric materials (Fig. 1.5) with multifunctional properties (thermal, electric, and mechanical) that make it suitable across a number of other electronic applications.

The classification of materials across piezoelectricity, pyroelectricity, and ferroelectricity is denoted in Fig. 1.6. A material exhibits these properties only if it lacks an inversion center within its crystalline structure. Crystal structures fall into 32 classes, of which 21 classes are non-centrosymmetric. Aside from one of the 21 groups, which contains an inversion center, all crystals in the remaining 20 classes exhibit piezoelectricity, which is defined as how the electric polarization changes in response to an applied stress (or vice versa). It is well known that piezoelectric span a vast range of applications, but for use in RF technology, piezoelectric micro-electromechanical system (MEMS) resonators have steadily grown to become a multi-billion-dollar industry, with the most commonly used materials including AlN and Zinc Oxide (ZnO) [7]. The constitutive equations for piezoelectricity are denoted in (1.1) and (1.2):

$$T = c^E S - eE \tag{1.1}$$

$$D = eS + \epsilon^S E \tag{1.2}$$

where D, E, T, S, e, c^E, and ϵ^S refer to the electric flux density, electric field, stress, piezoelectric stress coefficient, elasticity at constant E, and permittivity at constant S.

Piezoelectric materials that also exhibit a change in spontaneous polarization changes with temperature are referred to as pyroelectric materials. Pyroelectric infrared (IR) detectors have been developed to measure thermal radiations, and pyroelectrics have also been employed in energy harvesting devices [7], [12].

For some pyroelectric materials, ferroelectricity occurs when an external electric field allows for the reversal of the spontaneous polarization, thereby exhibiting a hysteresis loop. Within this thesis, the properties of two different ferroelectric materials will be utilized to develop electronically reconfigurable BAW resonators for future front-ends. For BST, acoustic resonators based on electrostrictive transduction will be employed in RF filters. For ScAlN, electric field induced polarization inversion will be utilized, causing the film to effectively behave as if they possess negative piezoelectric coefficients.

1.2.1. Ferroelectric Barium Strontium Titanate

As mentioned in the previous section, ferroelectric BST is a multifunctional material whose electrical properties and applications are dependent on the operating temperature (referred to as the Curie temperature, T_c) that dictates the phase of the material. Ferroelectrics are either in the ferroelectric (polar) or paraelectric (nonpolar) phase, and Fig. 1.7 depicts the T_c variation for BST based on strontium doping concentrations [9]. Already, thin film BST has been widely employed in tunable microwave circuits, due to both high relative permittivity ($\varepsilon_r > 200$) and large electric

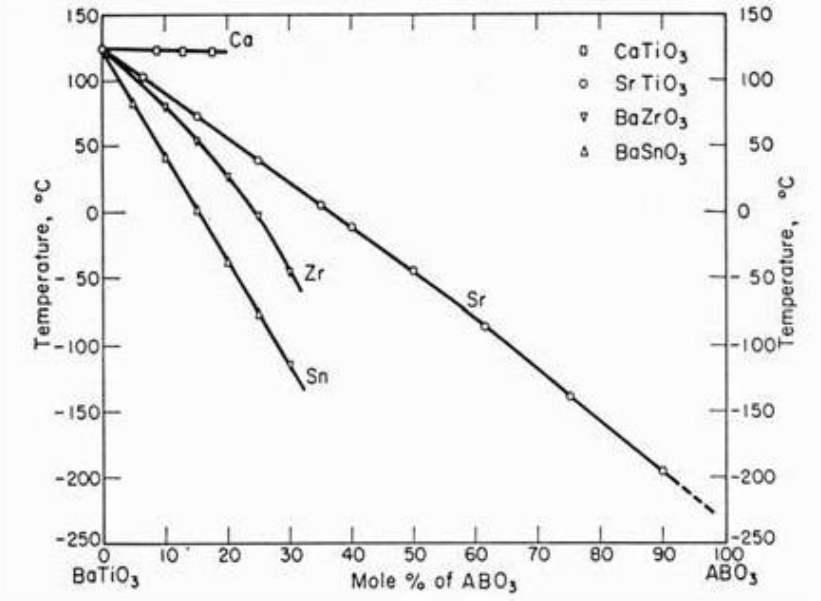

Fig. 1.7: Variation of the curie temperature based on doping of different materials for BST, reproduced from [3].

field dependent tunability greater than 5:1 [14], [15].

In addition to the electric properties, the work conducted herein will exploit the acoustic properties of paraelectric phase BST for resonator operation. The mechanism for

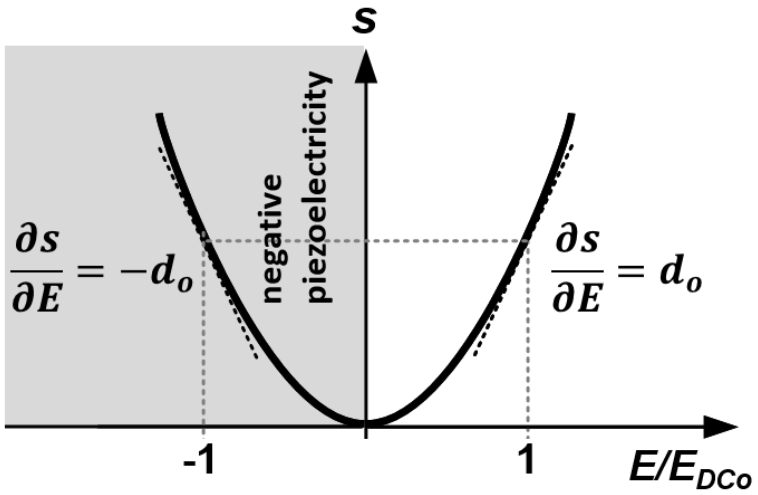

Fig. 1.8: Typical strain (S) versus the normalized electric field (E) curve for ferroelectric materials in paraelectric phase; the slope of the S-E curve at each bias point represents the effective piezoelectric coefficient (do) in the material.

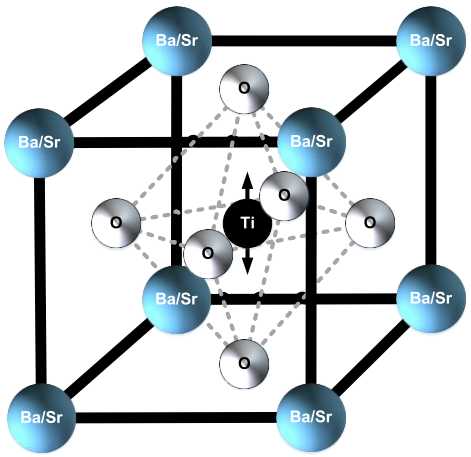

Fig. 1.9: The crystalline structure of perovskite ferroelectric BST in its paraelectric phase, where the arrows indicate Ti ion shift with electric field application.

electromechanical transduction is primarily through the electrostriction effect, also referred to as the electric-field-induced piezoelectric effect. The effective piezoelectric coefficient of the ferroelectric is determined through the slope of the strain curve at a particular applied electric field (E_{dc}) depicted in Fig. 1.8; therefore, ferroelectrics such as BST not only provide E-field induced piezoelectricity but also exhibit an E-field-induced *"negative"* piezoelectricity, when biased in the left region of the strain-E field plot (a negative DC electric field value). From this relation, it is only when there is an external DC voltage across the BST film, that electrostriction occurs. The electric field-induced piezoelectricity is also intuitively described within the material unit cell, as shown in Fig. 1.9. Under zero bias, the unit cell of BST in paraelectric phase is described by a cubic, center-symmetric structure. An applied DC field shifts the center Ti ion, thereby introducing asymmetry to the crystal structure. Hence, both the sign and magnitude of effective piezoelectricity coefficient can be directly controlled in the ferroelectric layer solely based on the magnitude and direction of the applied DC electric field.

The constitutive relations that govern electrostriction effect are denoted in (1.3) and (1.4):

$$S = s^E T + QP^2 \tag{1.3}$$

$$P = P_s + \chi E \tag{1.4}$$

where *S*, *s*, T, *Q*, *P*, χ, and *E* are the mechanical strain, compliance, mechanical stress, charge-related electrostrictive coefficient, electric polarization, susceptibility, and electric field respectively [16]. Solving for strain, (1.5) is obtained:

$$S = \ QP_s^2 + E(2QP_s\chi + Q\chi^2 E) \tag{1.5}$$

In the paraelectric phase of BST, where there is no spontaneous polarization, P_s, the quadratic relation between strain and electric field can be simplified to solely the third term (1.6):

$$S = \ Q\chi E^2 \tag{1.6}$$

(1.6) illustrates that in the paraelectric phase, electromechanical transduction for BST occurs primarily through the electrostrictive or voltage-induced piezoelectric effect. This is in contrast to typical piezoelectric material like aluminum nitride, where the strain versus electric field relationship is almost linear, and the excited acoustic response is not switchable. Switchable resonators controllable solely through an applied DC electric field not only eliminates the need for switches along the RF front-end, but the discrete number of states (dependent upon the number of BST layers) of the device, allows for the design for acoustic filters with reconfigurable transfer function responses.

1.2.2. Ferroelectric Scandium Aluminum Nitride

While ferroelectric BST has been extensively researched and applied in RF applications, the ferroelectricity of ScAlN has only been more recently discovered [17]. Prior to the verification of ferroelectricity however, research interest has still been ongoing for scandium doped aluminum nitride, primarily due to the four to five orders of magnitude increase in piezoelectric coefficient d_{33} from pure AlN films. Fig. 1.10 depicts the relation between piezoelectric coefficient of $Sc_xAl_{(1-}$

$_{x)}$N alloys and Sc doping concentration, where the range is between 27.6 pC/N for 43% doped Sc versus 5.5 pC/N for 0% doping [18]. Large variations in the piezoelectric coefficient are attributed to the phase transition of the crystal structure from wurtzite to nonpolar rock-salt. (1.6) denotes the relation between piezoelectric coefficient and the maximum k_t^2 of a BAW resonator.

$$k_t^2 = \frac{d_{33}^2}{s^E \epsilon^T} \tag{1.6}$$

Micromachined AlN based FBARs are already an industry standard for their high performance (higher Q factors, low temperature coefficients of frequency (TCF), CMOS compatibility, and operation at high temperatures). As the FBW of acoustic filters are restricted by the overall electromechanical coupling coefficient of the piezoelectric, approximately FBW $\leq 0.5k_t^2$, the integration of ScAlN based filters within modern RF acoustic modules with significant enhancement of k_t^2 remains attractive. However, the growth of ScAlN, especially at higher doping

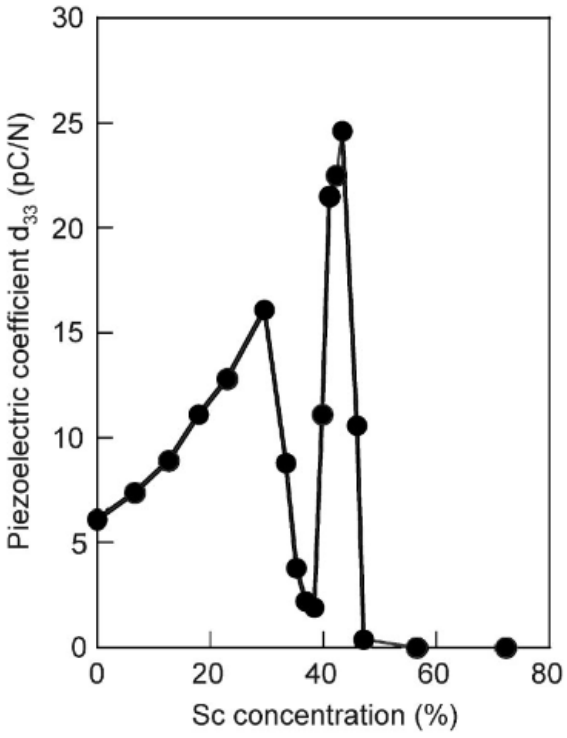

Fig. 1.10: Relationship between piezoelectric coefficient d_{33} and Sc concentration in doped AlN film, taken from [18].

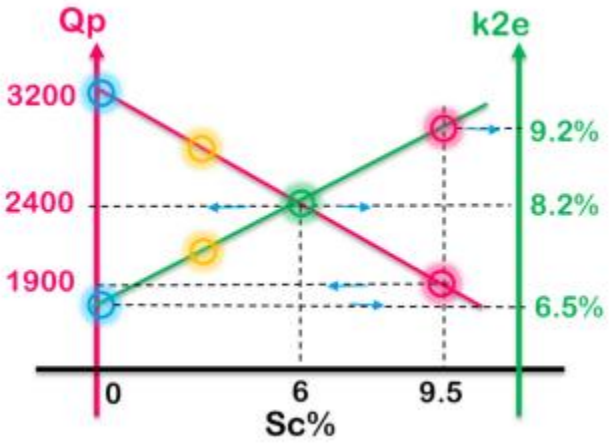

Fig. 1.11: Measured figure of merits for a number of ScAlN based BAW-SMR, taken from [19].

concentrations, is non-trivial, and initial works have shown the degradation of *Q* with Sc, as shown in Fig. 1.11, due to the reduction in crystal quality from secondary effects arising during growth, such as abnormally-oriented grains (AOGs) [19]. Nevertheless, the reported figure of merits (FOM) for ScAlN based resonators continues to improve year-on-year. With the added capability of ferroelectric switching, one can effectively switch the sign of the piezoelectric coefficient within ScAlN. This property will be employed to design a mm-Wave higher order mode FBAR that potentially overcomes limitation of frequency scaling in modern RF acoustics.

1.3.Dissertation Goal and Organization

The main objective of this thesis is to develop reconfigurable bulk acoustic wave resonators and filters in two different ferroelectric films, BST and ScAlN, for future wireless communication systems. The presented design and projects aim to either simplify the RF front-end by employing ferroelectric film to eliminate the need of switches and provide transfer function reconfigurability or design BAW resonators at higher frequencies, specifically at mm-Waves, dictated in 5G communications. The organization of this dissertation is as follows: the following chapters will

discuss both standalone and hybrid ferroelectric BST based filter designs in conjunction with lumped element surface mount components. The designs are based on the strong electrostriction effect, otherwise referred to as electric-field induced piezoelectricity, of BST.

Chapter 2 will discuss the design beginning from a single BST FBAR. Then, intrinsically switchable BST FBAR filter design will be presented before scaling up to the design of an entire four channel BST filter bank. The filters for each path are employed in a 2.5 stage π-network configuration, with center frequency offset at 1.74, 1.85, 1.94, and 2.05 GHz, respectively. By solely applying DC bias voltage of the associated resonator, the filter bank can transition between multiple filter channels with and insertion loss of approximately 6.5 dB and isolation greater than 30 dB. The BST based filters significantly reduce the number of filters and switches in future multi-band RF front-ends.

Frequency adaptive components present notable reduction in complexity and size along the RF front-end, since they utilize the same hardware for operation in multiple bands. Chapter 3 present novel designs of BST acoustic wave lumped-element resonators (AWLRs) based filters that are capable of completely reconfiguring their transfer function. As a proof of concept, two different reconfigurable circuits (a bandstop to all-pass (BS-to-AP) reconfigurable filter and a bandpass to all-reject (BP-to-AR) reconfigurable filter) are co-designed and fabricated, where the filters exhibit fractional bandwidths of 2.5%. By changing the state of the BST FBARs through applied DC electric fields, the filtering response alters. As incremental addition of RF front-end chains for new wireless standards is not sustainable within the restricted circuit area designated for RF components, this approach potentially simplifies future wireless systems.

In Chapter 4, work conducted previously on mode-switchable ferroelectric FBARs [20] will be extended utilizing a different ferroelectric material, ScAlN. The proposed acoustic

resonators will employ thin film ferroelectrics with both positive and negative effective piezoelectric coefficients to overcome the fundamental limit of acoustic resonator's ever-decreasing performance with frequency, specifically the reduced electromechanical coupling factor, K_t^2. The control of piezoelectricity in individual ferroelectric layers within the proposed multilayer acoustic resonators allows for the generation of different patterns of nonuniform piezoelectric coefficients for the design of millimeter wave devices, where the device critical dimensions (*thickness and consequently, the area*) are not scaled down with the frequency of operation. This is highly advantageous as single layer bulk acoustic wave (BAW) devices suffer from increased losses with increased operating frequency and reduced area. As an experimental validation, a trilayer AlN-ScAlN-AlN FBAR for operation at 31 GHz is designed, fabricated, and measured. This is the first demonstration of a dual mode resonator, where the ScAlN polarization switches between first and third mode within a composite multilayer. Moreover, complete ferroelectricity switching of ScAlN is further verified.

Chapter 5 summarizes the work and presents future direction for reconfigurable acoustic wave devices based on multifunctional ferroelectrics with the aim of providing compact filtering across a wide frequency range, spanning 6-GHz up to mm-waves. Finally, journal and conference publications out of this work are listed.

Chapter 2

Design and Characterization of a BST based Switchless Filter Bank

2.1 Chapter Motivation

Wireless communication systems are already highly complex to properly operate within a crowded radio spectrum, but mobile data consumption and demands for greater data throughput

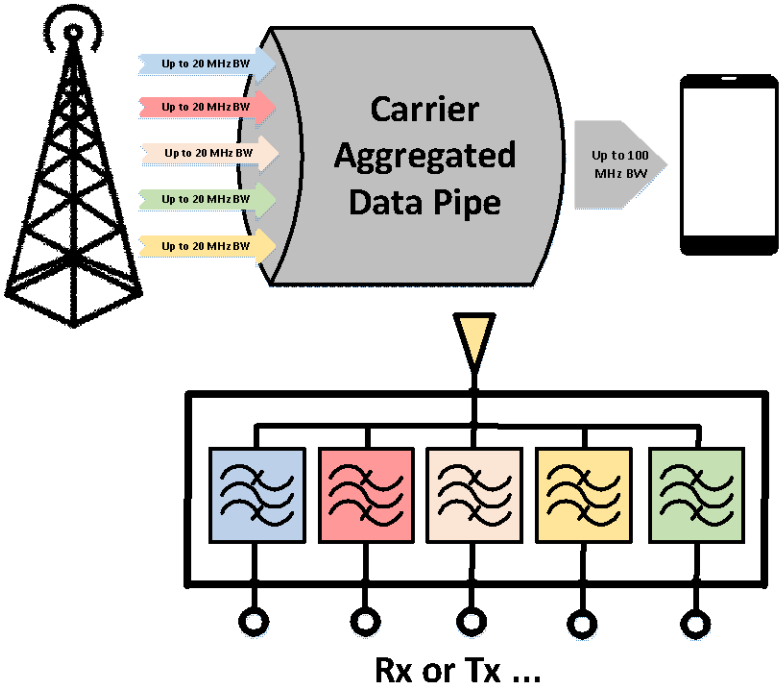

Fig. 2.1: General working carrier aggregation technique and simplified schematic for a multiplexer module, where the filters share a common node at the antenna port.

are not slowing down. Technological advancements, such as carrier aggregation (CA, Fig. 2.1), have been introduced and provides a means to increase data rates and capabilities by transmitting and receiving across multiple bands simultaneously [21]. The challenge of handling multiple frequency bands, including effects of cross-isolation, loading effects of adjacent components, and additional mixing products, only continues to expand as 1) the number of frequency band combinations increase and 2) designs shift from duplexers to more complex multiplexers with greater numbers of filters (tri-, quad-, quint-, etc.).

A promising solution to reduce complexity and minimize hardware footprint involves integrating frequency-agile components throughout the RF front end. One extensively researched approach proposes integrating ferroelectric BST into the design of switchable bulk acoustic wave devices. Electromechanical resonators, characterized both by an air-gap membrane (FBARs) [20], [22]-[30] and solidly mounted resonators (SMRs) [31]-[36], have already been successfully developed. Additionally, the electrostrictive effect of BST has been extended to realize intrinsically switchable filters, both electrically and acoustically coupled [20], [24], [26], [37]-[43].

In this chapter, a comprehensive overview, starting from the design of an intrinsically switchable BST FBAR is presented. Modeling of the FBAR element is further presented. The BST FBARs are then integrated into the design of ladder type, intrinsically switchable filters and ultimately, a quad band filter bank. The filter bank is capable of transitioning between different frequency bands of interests without using switches. The chapter elaborates on the detailed design for the BST resonator structure and filter topology. Finally, the simulation results, fabrication process, and experimental measurements of the intrinsically switchable BST FBAR filter bank are presented.

2.2 Bulk Acoustic Wave Resonator Overview

In general, the operating frequency for a thin film bulk acoustic wave resonator is dictated by the membrane thickness, comprising of a piezoelectric plate with two thin electrodes. Fig. 2.2 depicts a prototypical FBAR operating in the thickness extensional (TE) mode, which are the most

$$\omega_n = (n+1)\left(\frac{\pi v}{2d}\right), n = 0,1,2. \ldots$$

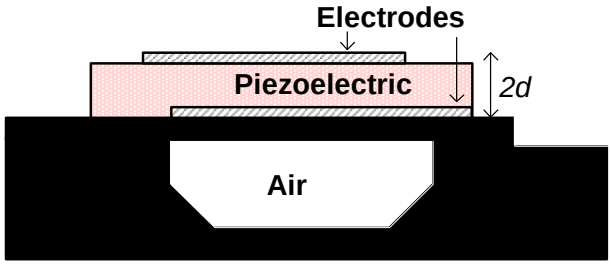

Fig. 2.2: Generalized structure for a FBAR with a plate thickness of *2d* and thickness-extensional mode operating frequency, where *v* represents the acoustic velocity.

commonly utilized modes in commercialized acoustic resonators and filters. RF signals applied across the electrodes is directly converted to produce acoustic waves that propagate within the bulk of the slab [7]. Through appropriate acoustic impedance mismatch (i.e. at the air-electrode interfaces), the waves are confined within the bulk. A one-dimensional (1D) model for the TE modes in the FBAR can be analyzed in order to directly arrive at electric circuit models utilized for simulations. From chapter 1, the piezoelectric constituent relations for electrical displacement are given in (1.1) and (1.2). Typically, FBARs have lateral dimensions that are order of magnitude larger than the thickness of the membrane; therefore, it can be assumed that the plate is laterally infinite and clamped (S_1, S_2, S_4, S_5, S_6 = 0) for plane wave propagation in the thickness direction. For a prototypical resonator with a conventional piezoelectric such as AlN or ZnO (both of which are hexagonally symmetric) the expanded form of relations is provided in (2.1) and (2.2).

$$\begin{bmatrix} T_1 \\ T_2 \\ T_3 \\ T_4 \\ T_5 \\ T_6 \end{bmatrix} = \begin{bmatrix} c_{11} & c_{12} & c_{13} & & & \\ & c_{11} & c_{12} & & & \\ & & c_{33} & & & \\ & & & c_{44} & & \\ & & & & c_{44} & \\ & & & & & c_{44} \end{bmatrix} \begin{bmatrix} S_1 \\ S_2 \\ S_3 \\ S_4 \\ S_5 \\ S_6 \end{bmatrix} - \begin{bmatrix} 0 & 0 & e_{31} \\ 0 & 0 & e_{31} \\ 0 & 0 & e_{33} \\ 0 & e_{15} & 0 \\ e_{15} & 0 & 0 \\ 0 & 0 & 0 \end{bmatrix} \begin{bmatrix} E_1 \\ E_2 \\ E_3 \end{bmatrix} \tag{2.1}$$

$$\begin{bmatrix} D_1 \\ D_2 \\ D_3 \end{bmatrix} = \begin{bmatrix} \varepsilon_1 & 0 & 0 \\ & \varepsilon_2 & 0 \\ & & \varepsilon_3 \end{bmatrix} \begin{bmatrix} E_1 \\ E_2 \\ E_3 \end{bmatrix} + \begin{bmatrix} 0 & 0 & 0 & 0 & e_{15} & 0 \\ 0 & 0 & 0 & e_{15} & 0 & 0 \\ e_{31} & e_{31} & e_{33} & 0 & 0 & 0 \end{bmatrix} \begin{bmatrix} S_1 \\ S_2 \\ S_3 \\ S_4 \\ S_5 \\ S_6 \end{bmatrix} \tag{2.2}$$

Further simplification includes assumptions that there is no electric flux leakage for a piezoelectric medium (D_1, D_2 = 0), and the electrodes are infinitesimally thin (in practice, the electrodes for fundamental mode FBARs are approximately 10% of the piezoelectric thicknesses). The resulting stress and electric field relations take the form shown in (2.3) and (2.4), with the displacement *u* obeying wave equation in (2.5):

$$T_3 = c_{33}^D S_3 - e_{33} D_3 \tag{2.3}$$

$$E_3 = -e_{33} S_3 + \frac{1}{\epsilon_{33}^S} D_3 \tag{2.4}$$

$$\frac{\partial^2 u}{\partial t^2} = \frac{c_{33}^D}{\rho}\left(\frac{\partial u}{\partial z^2}\right) \tag{2.5}$$

where ρ denotes the mass density of the film and denotes the c_{33}^D piezoelectrically stiffened elastic constant. Then, the general solution of particle displacement can be found in (2.6):

$$u = \left(a * sin\left(\frac{\omega z}{v^D}\right) + b * cos\left(\frac{\omega z}{v^D}\right)\right) e^{i\omega t} \tag{2.6}$$

where *a* and *b* are determined by assuming stress free conditions at the top and bottom of the plate and v^D indicates the sound velocity. For a time harmonic electric flux density, substituting the displacement equation (2.6) back into the constitutive equations provides key insights into the

FBAR parameters of the electrical admittance (2.7), static capacitance (2.8), and electromechanical coupling coefficient (2.9).

$$Y = \frac{i\omega C_0}{1 - \frac{k_t^2 \tan\left(\frac{\omega t}{2v^D}\right)}{\frac{\omega t}{2v^D}}} \tag{2.7}$$

$$C_0 = \frac{A\epsilon_{33}^S}{2d} \tag{2.8}$$

$$k_t^2 = \frac{e_{33}^2}{c_{33}^D \epsilon_{33}^S} \tag{2.9}$$

where *A* encompasses the active area of the resonator. Practically, the key parameters highlighted in FBAR design are the quality factor, *Q*, and electromechanical coupling coefficient, k_t^2. The quality factor represents a proportion of the stored energy versus dissipated power per cycle and is a metric to determine how much acoustic, electrical, and other associated losses are in the FBAR; ultimately in acoustic filter design, the quality factor of the FBAR dictates the minimum insertion loss (IL) and roll-off of the filter. As mentioned previously, k_t^2 sets a limitation on the maximum achievable bandwidth of the filter. From (2.9), k_t^2 can be derived based on resonance (f_s) and anti-resonance (f_p) frequencies (setting *Y* and *1/Y* = 0). Assuming small values of k_t^2, which is typically around 5-6% for AlN, (2.10) provides an expression for the effective coupling coefficient of a resonator.

$$k_t^2 = \frac{\pi^2}{4}\frac{f_p - f_s}{f_p} \tag{2.10}$$

2.3 BST FBAR and Design for Optimal k_t^2

Thin film, paraelectric phase BST substituted as the transducer layer for a conventional FBAR realizes an intrinsically switchable resonance controlled solely through an applied DC bias

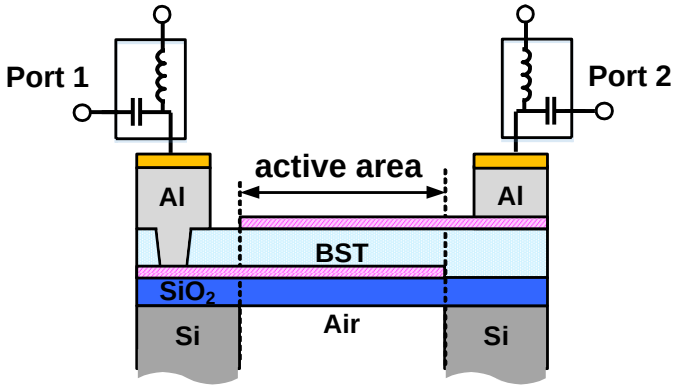

Fig. 2.3: BST FBAR structure, where the devices are released after XeF_2 etching.

voltage (Fig. 2.3). Fig. 2.4 depicts a standard impedance response for the BST FBAR in both states: 1) Without any bias voltage, the resonator acts as a simple metal-insulator-metal (MIM) capacitor. 2) With a nonzero DC bias voltage applied across the electrodes, an induced piezoelectric effect is exhibited, and an RF excitation results in mechanical deformation. The electrical response of the BST FBAR in both states can be presented with an equivalent circuit, as depicted in Fig. 2.4. The on state of a BST FBAR is accurately represented with a well-known modified Butterworth-Van Dyke (mBVD) model [44]. The motional branch, which dictates the resonance frequency of the FBAR, is modelled with a motional capacitance (C_m), motional inductance (L_m), and mechanical loss (R_m) in series. The combination of the motional and electrical branch, which consists of an electrical capacitance (C_e) and dielectric along with spurious mode losses (R_e), define the anti-resonance of the structure. Additional conductor losses are modeled through a resistor (R_s). (2.11)

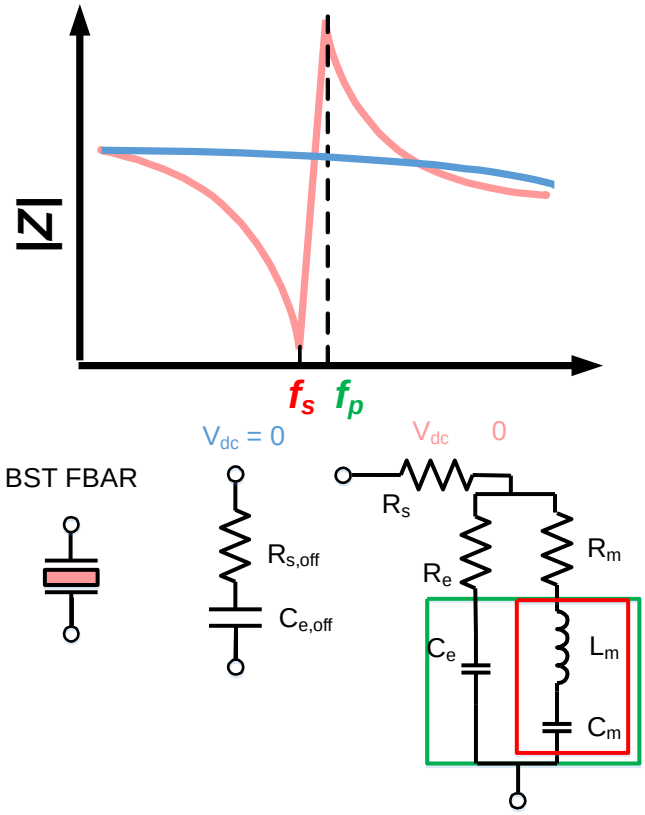

Fig. 2.4: Generalized impedance response for a BST FBAR close to resonance in the on (depicted in red) and off (depicted in blue) state.

and (2.12) provide the corresponding resonant and anti-resonant frequencies derived from the mBVD model.

$$f_s = \frac{1}{2\pi\sqrt{L_m C_m}} \tag{2.11}$$

$$f_p = f_s \sqrt{\frac{C_m + C_e}{C_e}} \tag{2.12}$$

While the mBVD model allows for quick and accurate prediction of the acoustic resonator's response within a filter circuit, another model that has been widely employed to accurately predict the electrical impedance response of piezoelectric transducers, while also accounting for thicknesses of each layer at microwave frequencies where the original assumptions of infinitesimally thin electrodes are no longer valid, is the Mason model [45]. Previous work to

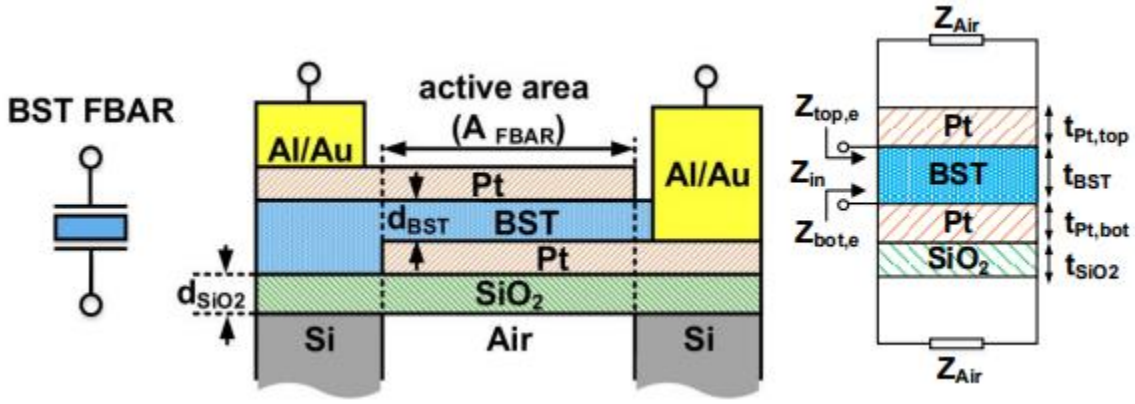

Fig. 2.5: 1-D Acoustic transmission line model for a BST FBAR, reproduced from [46].

optimize the k_t^2 for BST FBARs utilizes a 1D acoustic transmission line model approach, as depicted in Fig. 2.5 [46]. By using the acoustic parameters of each layer, the intrinsic electromechanical coupling coefficient for BST could be extracted and optimized based on variation of different layer thicknesses, frequency of operation. As shown in Fig. 2.6, the Mason model utilizes a similar approach, employing both the acoustic parameters (propagation constant, thicknesses, characteristic impedances) and piezoelectric constants to predict the impedance response of a resonator. Two mechanical ports defined by force and acoustic velocity along with

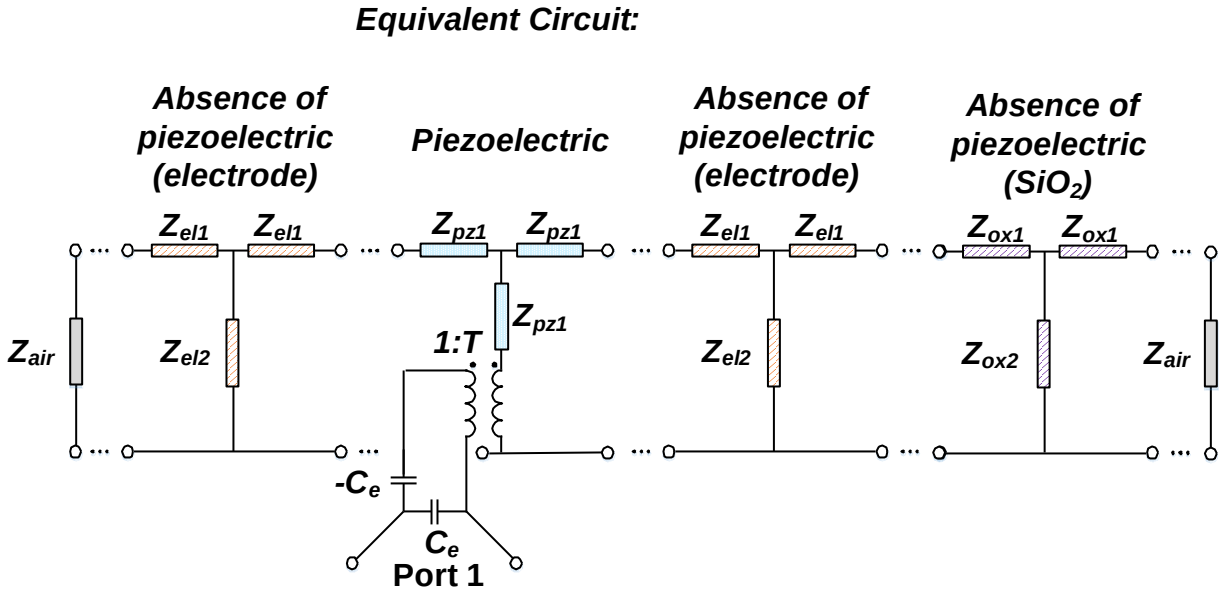

Fig. 2.6: Mason Model implementation of a BST FBAR.

one electrical port defined by voltage and current comprises of the three-port piezoelectric layer. The corresponding impedances, Z_1 and Z_2, are denoted in (2.13) and (2.14):

$$Z_1 = jZ_m \tan\left(\frac{k_1 d}{2}\right) \tag{2.13}$$

$$Z_2 = -jZ_m \csc(k_1 d) \tag{2.14}$$

It must be noted that losses associated with the resonator can also be incorporated by introducing a complex propagation constant for each layer.

The BST resonator structure comprises of BST, two platinum electrodes, and a SiO_2 layer. Platinum electrodes are selected due to their chemical inertness at a high-temperature oxidizing ambient that is required for optimal BST deposition [47]. However, a SiO_2 layer is then required prior to bottom electrode deposition in order to prevent the diffusion of Pt through the Si substrate during high temperature growth. The acoustic material parameters utilized for each of the layers

Table 2.1
Acoustic Material Parameters for the different BST FBAR layers

Material	***Q***	***Z_0* (kg/m^{2}s)**	***v_l* (m/s)**
Pt	260	69.4 x 10^6	3236
BST	500	35.3 x 10^6	6307
SiO_2	1000	12.8 x 10^6	5848
Si	2000	19.6 x 10^6	8445

are provided in Table 2.1. The piezoelectric properties of BST are then optimized in the Mason model to fit previous measurements of on state BST FBARs, and the intrinsic coupling coefficient for BST is set to be approximately 9.5%. Fig. 2.7 indicates the simulated maximum coupling coefficient for a 2 GHz BST FBAR represented with a Mason model based on the ratio of Pt to BST thicknesses and corresponding acoustic parameters. It can be seen the boost of achievable k_t^2 when high acoustic impedance electrodes such as Pt are utilized, as the shape of the stress field for the mode matches the electric field profile [48]. The finalized thicknesses of the BST FBARs

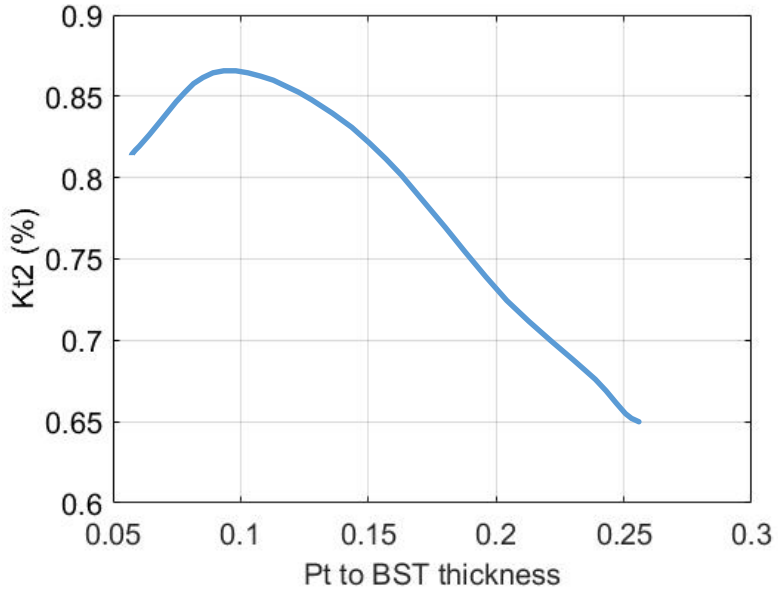

Fig. 2.7: Corresponding simulated k_t^2 relation with the platinum electrode thickness, reaching a maximum at approximately 100 nm Pt.

Table 2.2
2 GHz BST FBAR finalized structure

Layer	Thicknesses (nm)
Pt_{top}	100
BST	700
Pt_{bot}	100
SiO_2	300

employed in a number of different RF reconfigurable filters (center frequency shifting, transfer function reconfigurability, etc.) discussed in the next sections are listed in Table 2.2. For large signal model analysis of BST FBARs, approaches based on phenomenology of electrostriction have been incorporated in a modified Mason model design [86].

2.4 BST FBAR Ladder Type Filter Design

There are a number of acoustic filter topologies with applications in the microwave regime. The filters are classified into two main categories based on coupling between interconnected

acoustic resonators, which are either acoustically or electrically connected. There are a number of advantages for each type; for instance, acoustically coupled filters provided greater out-of-band rejection due to smaller feedthrough capacitances [7]. One of the most commonly utilized filters for BAW/FBAR are electrically ladder type filters, owing to its simplicity in design process and sharp near-in selectivity [21]. Fig. 2.8 indicates the schematic and corresponding impedance response of each series and shunt BST FBAR (when switched on) comprising of a ladder type filter. The shunt resonators are downshifted to operate at a slightly lower resonance frequency than the operating frequency of the series connected BST FBARs. Typically, this is conducted by

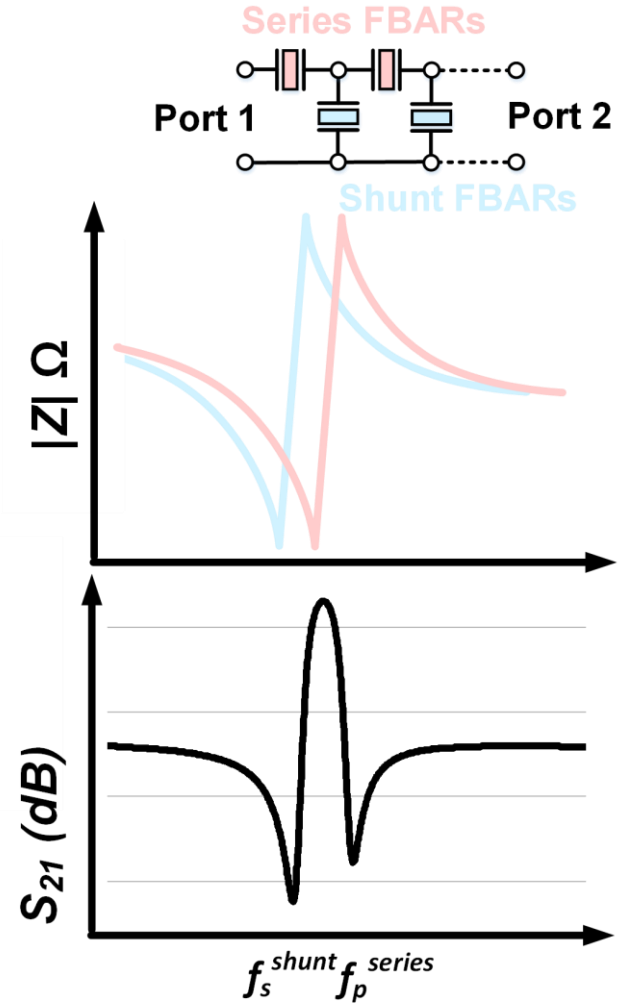

Fig. 2.8: BST ladder type filter response based on resonance and anti-resonance frequencies of the BST FBARs when switched on.

adding compensation layers of metal after top electrode deposition (for BST FBAR filters within this work, additional platinum is deposited).

The operation principle is dictated by the impedance response of the corresponding resonators, where two transmission zeros are given by the series resonance of the shunt resonator (f_s^{shunt}) and parallel resonance of the series resonator (f_p^{series}). When an RF signal is excited at f_s^{shunt}, the signal bypasses to ground due to the shunt resonator's low impedance. Conversely, a high impedance between port 1 and 2 from the series connected FBAR at f_p^{series} prevents RF signal from passing through. In the passband center frequency, where the anti-resonance of the downshifted shunt FBAR (f_p^{shunt}) matches resonance frequency of the series FBAR (f_s^{series}), a high impedance to ground is provided by the shunt FBARs where there is a low impedance path between port 1 and port 2 provided by the series FBARs. Far away from the operating frequencies of the two FBARs, the resonators act as capacitors, and the associated impedance determines the out-of-band rejection.

Based on the finalized thicknesses for a 2 GHz BST FBARs, a systematic design approach relying on image parameter method [37] for a BST FBAR based ladder type filter with a passband centered 2 GHz is conducted. The approach is a classical synthesis technique for distributed element filters, that initially designs a repeatable filter unit cell to achieve a desired response. Unit cells are then cascaded together without variation in the overall impedance or filter response. As greater requirements in terms of out-of-band rejection and performance, thereby leading to higher number of stages, are required for acoustic filters along the RF front-end, filter design based on deriving image impedance and propagation constant is a quick and standard approach to accurately

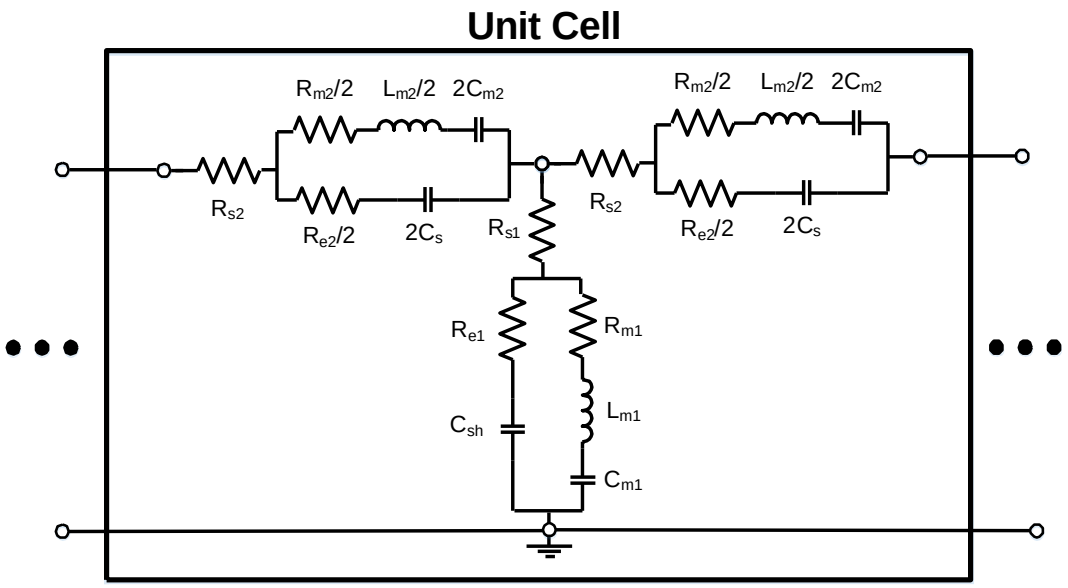

Fig. 2.9: 1.5 stage filter unit cell for BST FBARs in the on state for which image parameter method can applied.

optimize such filters. More information regarding the image parameter method for BST FBAR ladder filters is discussed in [37]. Fig. 2.9 depicts the filter unit cell, which consists of a T-network of two series and one shunt BST FBARs. As mentioned in the previous section, an equivalent mBVD model is utilized to simulate the electrical response of the on-state BST resonators with electrical and acoustic characteristics of Q_m, Q_e, and electromechanical coupling coefficient (k_t^2) of 300, 80, and 7%, respectively. These electrical and acoustic parameters are derived from previous fabrication results of BST FBARs with similar structures. A lossy capacitor circuit models the off state frequency response of a BST FBAR with relative permittivity approximately 2-2.5 the value of the permittivity required to switch on the resonator. Firstly, the electrical capacitances of the series (C_s) and the shunt (C_{sh}) BST FBARs when switched on are determined in order to meet the required design constraints. The associated set of design equations determining the series and shunt FBARs' electrical capacitances in the unit cell based on FBW, center frequency (f_c), and system impedance (Z_0) are provided in (2.15) and (2.16), respectively:

$$C_s = \left(\frac{1}{\omega_c Z_0 \sqrt{M}}\right) \div \sqrt{\frac{(M-1)^2}{FBW^2 M}\left(1+\sqrt{1+FBW^2}\right)-2} \tag{2.15}$$

$$C_{sh} = \left(\frac{1}{2\omega_c Z_0 \sqrt{M}}\right) \times \sqrt{\frac{(M-1)^2}{FBW^2 M}\left(1+\sqrt{1+FBW^2}\right)-2} \tag{2.16}$$

where M is a constant related to the k_t^2 of the BST FBARs.

The unit cell is then cascaded for a ladder-type 2.5 stage filter are designed for a system impedance of Z_0 = 50 Ohms, f_c = 2 GHz, and FBW of 3%, and the filter schematic along with biasing network required to switch on the BST FBARs is provided in Fig. 2.10. Keysight PathWave Advanced Design System (ADS) is utilized to simulate the impedance response, where one note is that the center FBAR is split into two larger equivalent FBARs in order to simplify the DC biasing, such that three terminals, two bias tees and one additional DC probe pad are required to turn on all six BST FBARs. The biasing resistance for the center two series FBARs is determined to be approximately 2000 Ohms to ensure minimal degradation in on state filter's insertion loss, while maintaining the fast-switching speed of the BST FBARs [46].

Simulation results for both states of the intrinsically switchable BST filter at 2 GHz are provided in Fig. 2.11. The electrical capacitances for the series and shunt elements are 1.6 and 3

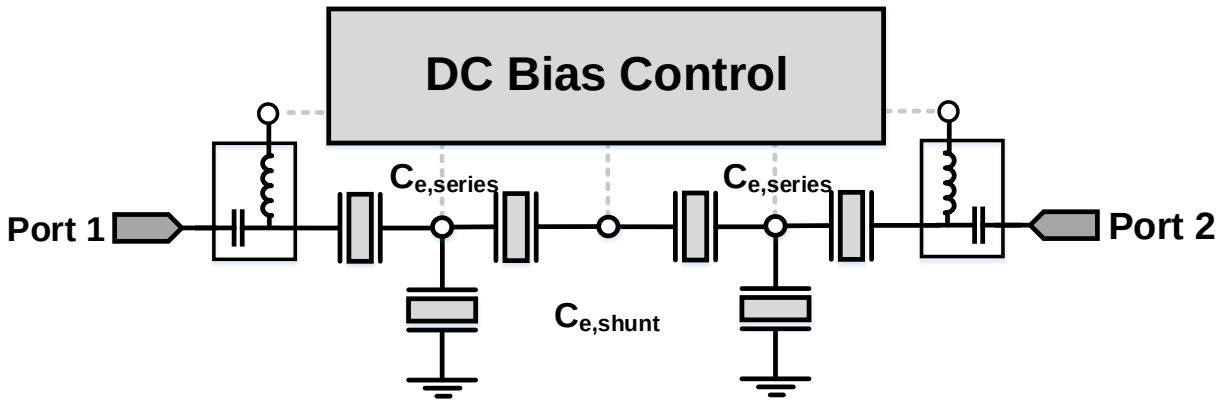

Fig. 2.10: Standalone 2.5 Stage BST FBAR Filter with associated DC biasing network. The middle node is connected to a high resistivity biasing line of 2 kΩ.

pF, respectively. When the BST FBARs are switched on, a characteristic band-pass transmission response is shown with minimum IL of 3 dB and out-of-band rejection of 24 dB. The return loss of filter when switched on also demonstrates greater than 15 dB across the pass-band, indicating that the filter is well-matched to 50 Ω. Subsequently when zero DC bias is applied, all resonators in the structure turn off and behave as capacitors, presenting an isolation of approximately 30 dB across the entire frequency range, as shown in Fig. 2.12. With the design of the BST ladder type

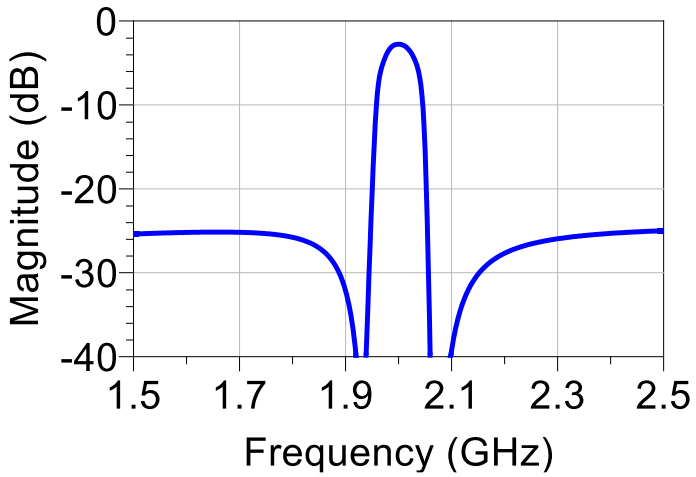

(a)

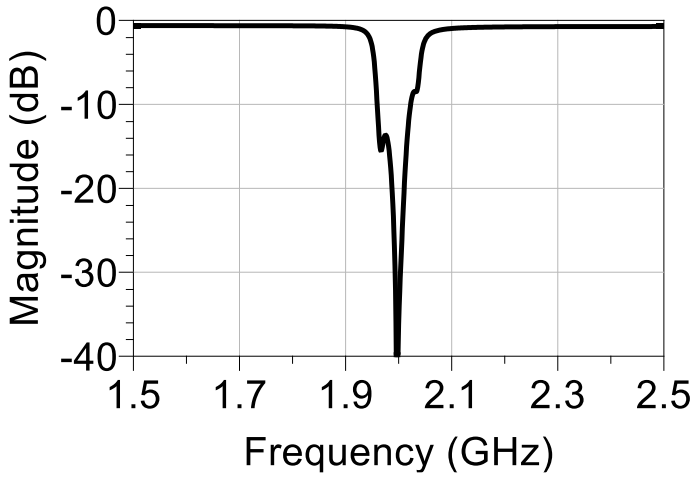

(b)

Fig. 2.11: The simulated ladder type filter (a) transmission and (b) reflection response when the BST FBARs are switched on.

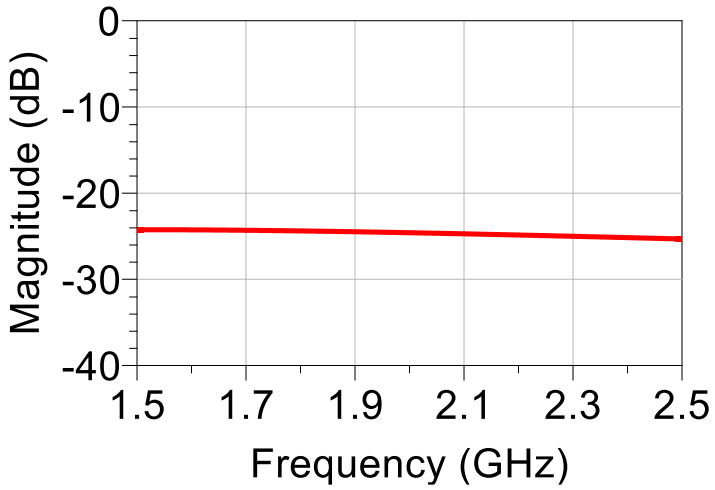

Fig. 2.12: The simulated ladder type filter transmission response when the BST FBARs are switched off.

filters established, a filter bank comprised of a number of intrinsically switchable filters is then established for multi-band operation.

2.5 BST FBAR Filter Bank Design

A quad band intrinsically switchable filter bank based on BST FBARs has been designed, fabricated, and measured for the first time, with lower reported insertion loss compared to previous intrinsically switchable BST filter banks to date [41]. Unlike the previous implementation, the design does not use varactors to achieve isolation and matching response between different filter channels, which directly contributes to the transmission loss. Instead, the design incorporates phase delay elements in a circuit topology similar to conventional manifold multiplexers in order to minimize the loading effect of the off-channel filters.

Four 2.5 stage filters based on BST FBARs, operating across neighboring frequency bands (1.7 to 2 GHz at 100 MHz increments) are connected in shunt to form the intrinsically switchable filter bank, as shown in Fig. 2.13. Each filter can be selectively switched on or off by applying DC voltage at their respective nodes, A_i, B_i, and C_i, to turn on all corresponding resonators of the

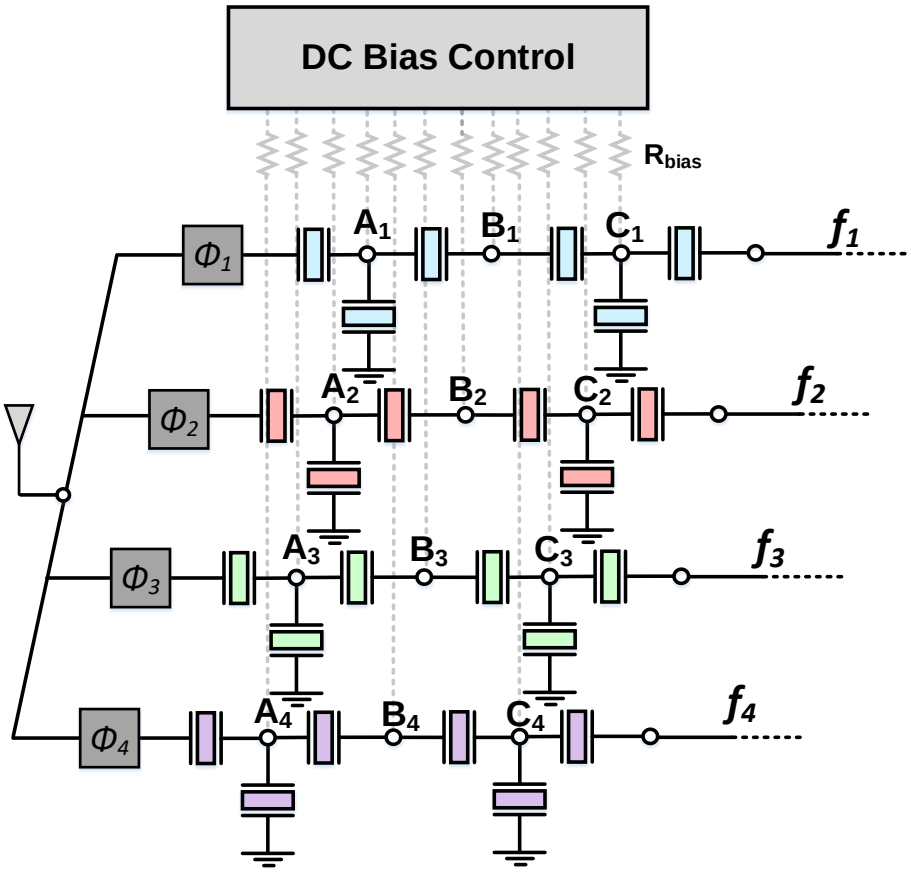

Fig. 2.13: Schematic of the designed four band 2.5 stage BST FBAR filter bank. DC biasing network is indicated with dashed grey lines and each filter is controlled through three distinct nodes.

selected filter path. For each filter path, a MIM BST capacitor is connected at the input side in order to improve the overall matching of the filter bank in conjunction with a single shunt inductor. Based on previous findings with simultaneous BST capacitor and resonator fabrication [41], this implementation reduces the electrical loss coming within the filter path while ensuring that each filter presents a relatively high impedance in its out-of-band frequency.

In each of the four filter paths, the shunt resonators of the ladder type configurations are mass loaded with Pt in order to downshift their resonance response, where thicknesses are determined the associated Mason Model. For Band 1 operation (f_c = 2 GHz), the thickness of the BST transduction layer within the FBAR is identical to previous sections (770 nm) with the Pt

electrodes are set at 100 nm [6]. Table 2.3 lists the finalized BST areas for all BST FBARs and

Table 2.3
Design Parameters for the BST devices across the Four Band Filter Bank

Filter Path	**Series FBAR A (μm^2)**	**Shunt FBAR A (μm^2)**	**Input Capacitor A (μm^2)**
Band 1 (f_c = 2 GHz)	1110	2108	986
Band 2 (f_c = 1.9 GHz)	1170	2196	816
Band 3 (f_c = 1.8 GHz)	1230	2356	660
Band 4 (f_c = 1.7 GHz)	1290	2440	660

capacitors in the quad band filter bank, which is based on (2.17) after applying image parameter method and optimization.

$$A = \frac{Cd_{BST}}{\varepsilon_0 \varepsilon_r} \tag{2.17}$$

Similar to previous sections, the simulated parameters for the mBVD models are set to Q_m and k_t^2 values of 300 and 6%, based on previously measured results.

The simulated filter response with a shunt matching inductor ($L = 1.6\ nH$) at the input is

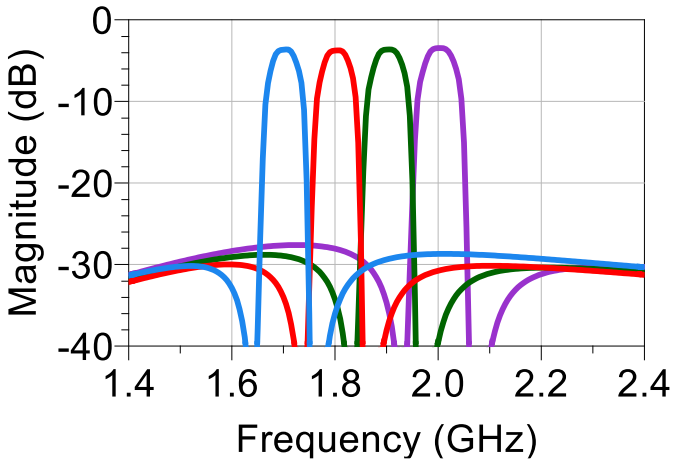

(a)

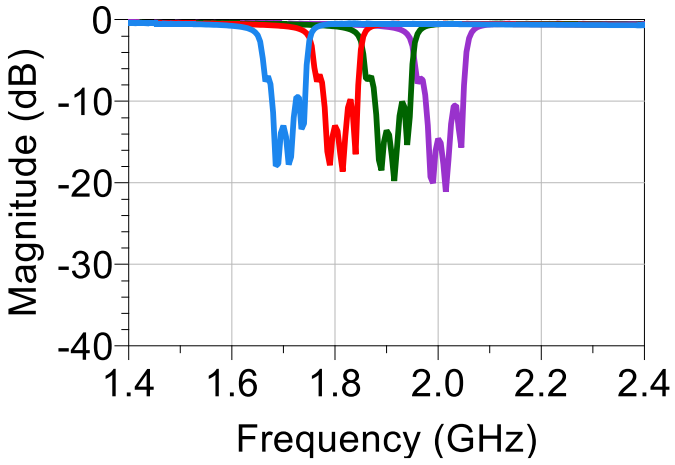

(b)

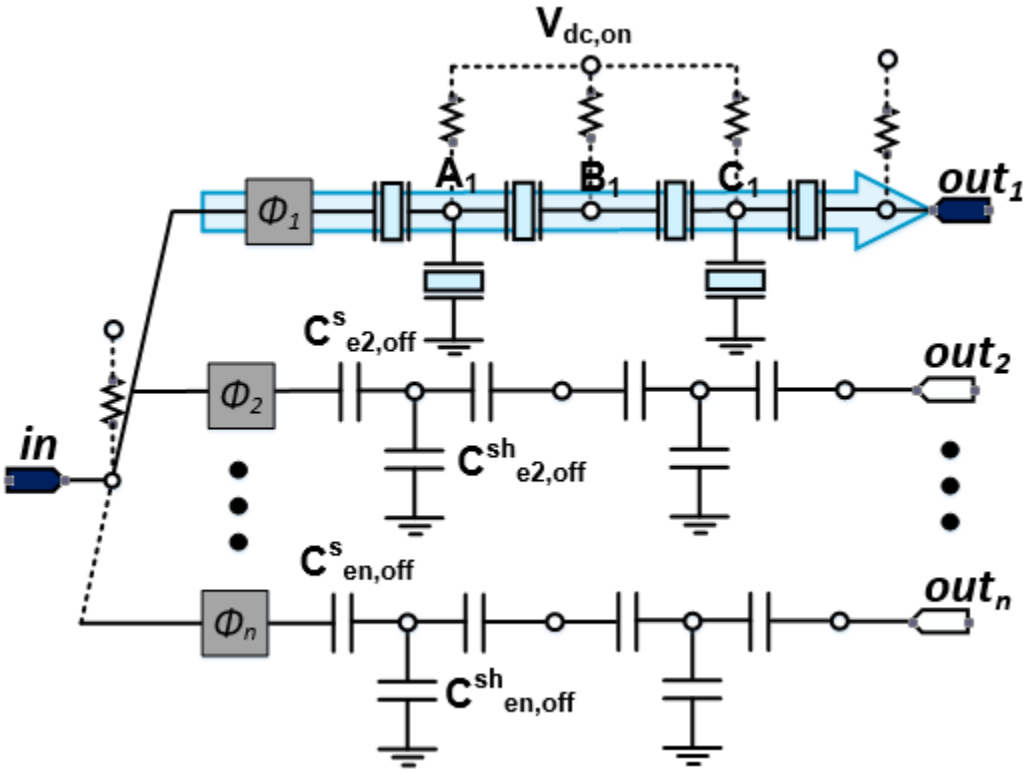

(c)

Fig. 2.14: The simulated (a) transmission and (b) reflection response for each of the 2.5 stage BST filters in the filter bank. (c) Equivalent circuit schematic and biasing for one band operation (n = 4).

provided in Fig. 2.14 for all four bands. Fig. 2.14 (c) depicts the biasing configuration and corresponding circuit schematic when solely one of the bands is switched on. The frequency response for each of the filters are superimposed on top of each other (i.e. each response is depicted

when only one of the four bands are switched on with the corresponding BST FBARs and biasing). The four BST FBAR based filters are selectively switched on to provide a minimum insertion loss of 4 dB with out-of-band rejection greater than 27 dB. Matching is also provided in Fig. 2.14(b) with greater than 10 dB in the passband for each of the filters. When all resonators and bands are switched off, the simulated quad bank filter demonstrates an isolation of approximately 30 dB, as depicted in Fig. 2.15.

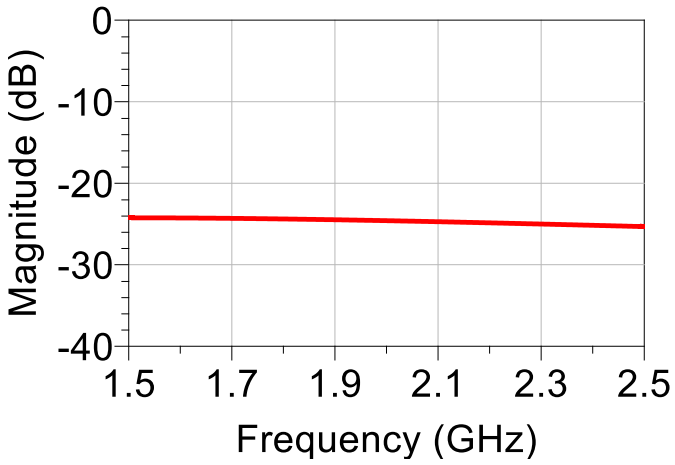

(c)

Fig. 2.15: The simulated transmission response when all BST FBARs are switched off.

2.6 Fabrication Process and Measurement Setup

The four channel BST FBAR filter bank, along with BST FBARs, are fabricated based on the following steps, as depicted in Fig. 2.16:

1) The fabrication process for the BST FBARs, where 300 nm of SiO_2 is first wet thermally grown on a Si (100) wafer.
2) The first 100 nm Pt bottom electrode deposition is conducted through an evaporation and lift-off procedure.

3) $Ba_{0.5}Sr_{0.5}TiO_3$ is grown using an RF magnetron sputtering system at a substrate temperature of 650°C. The system parameters are listed in Table 2.4.

Table 2.4
RF Sputtering System Parameters

Layer	Values
Pressure	45 mTorr
Ar/O_2	4:1
RF Power	300

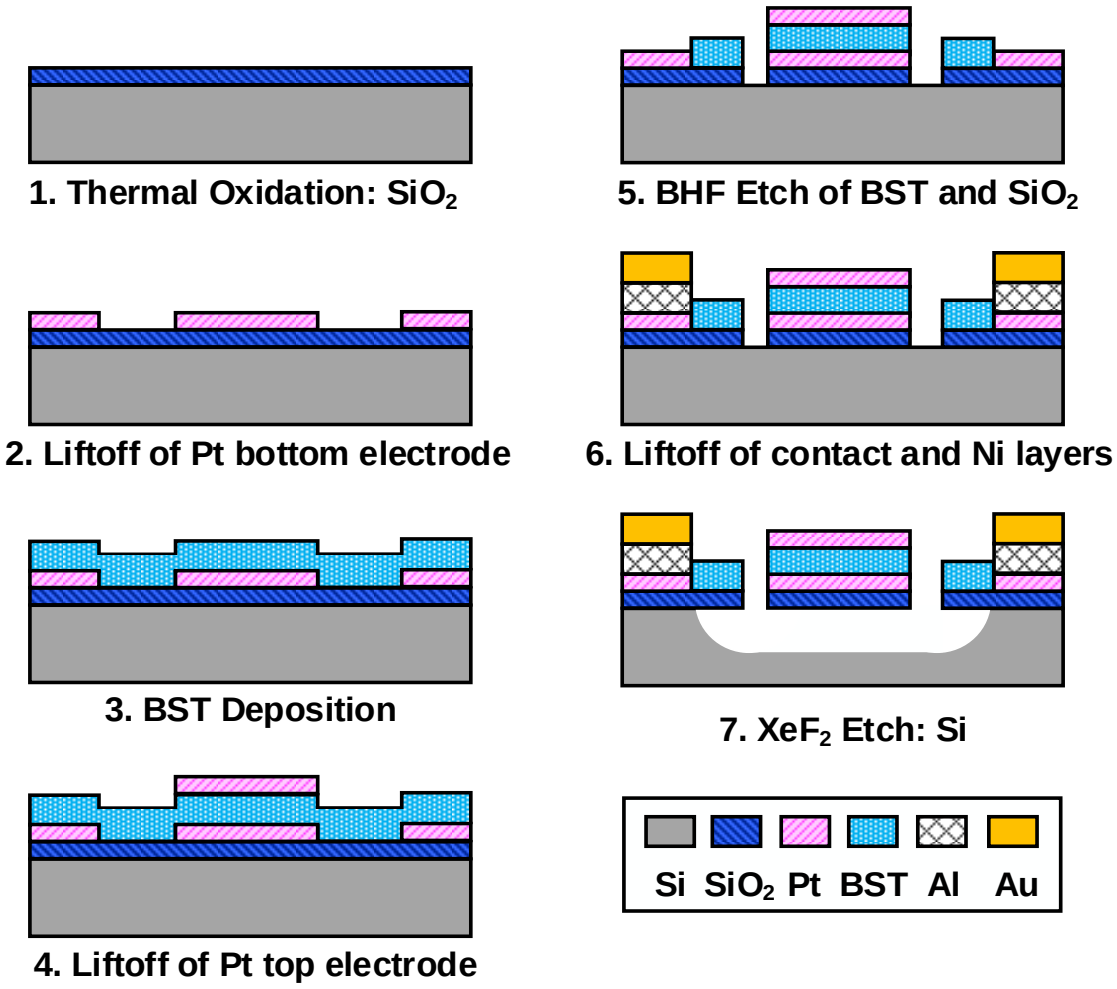

Fig. 2.16: Fabrication process for the BST FBARs and corresponding filters.

4) Top platinum electrode of 100 nm is deposited using a lift-off procedure. All subsequent Pt compensation layers are deposited using the same sequence. After top electrode deposition, the films are annealed at 500°C for 30 minutes in a O_2 environment.

5) A timed buffered hydrofluoric acid (BHF) etch is employed to etch BST and define both the release windows for the FBARs and expose bottom Pt. Subsequent to this, biasing lines of 50 nm NiChrome are deposited using an evaporation and lift-off process.
6) Ti/Al/Au (50/1500/100 nm) are then deposited as a contact layer for the ground-signal-ground (GSG) probes using an evaporation and lift-off procedure.
7) Finally, the FBARs are released using a front-side gaseous XeF_2 etch in 3.0 Torr environment.

A photograph of the fabricated reconfigurable quad band filter bank is presented in Fig. 2.17, where the size of the total active area is 340 µm x 840 µm. The measurement setup of the BST FBAR filters is shown in Fig. 2.18. The filter's S- parameters are measured using a two port Keysight network analyzer connected to a Cascade Microtech probe station with 150 µm-pitch GSG probes. DC biasing is applied to the resonators through bias tees in the input and output GSG

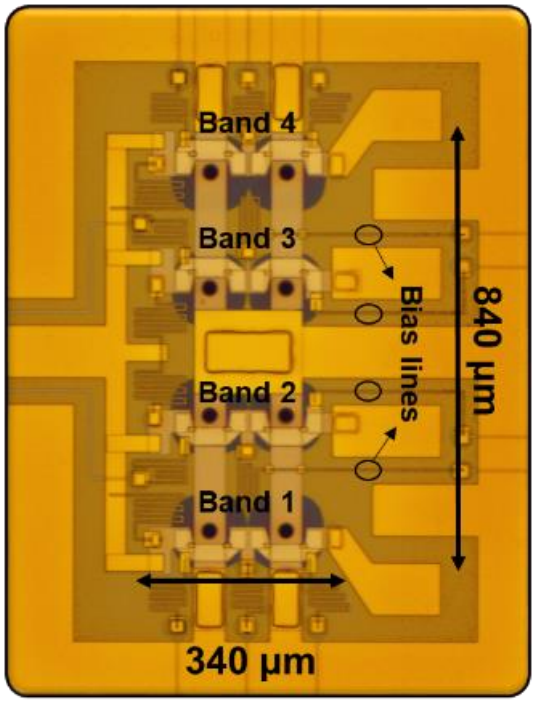

Fig. 2.17: A optical photograph of the fabricated BST FBAR quad channel 2.5 stage filter bank.

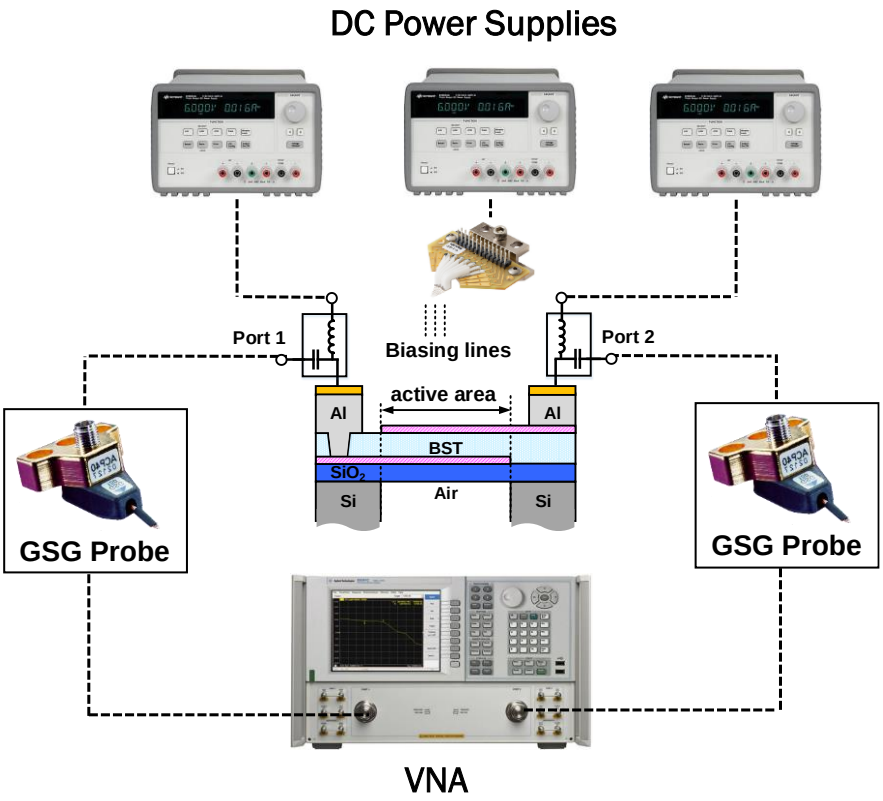

Fig. 2.18: Complete measurement setup for the BST FBARs and corresponding filters.

probes and a Cascade Microtech multicontact DCQ probe. Open-short-load calibration is conducted for a 50 Ω system impedance from 0.1 to 6 GHz.

2.7 Measurement Results and Discussion

2.7.1. Ferroelectric BST FBAR Measured Performance

Prior to filter bank measurements, individual BST FBARs on the same chip are measured to verify that the assumed electrical and acoustic parameters utilized for simulation are in line with the measured chip. Fig. 2.19 shows a photograph along with the corresponding mBVD model and

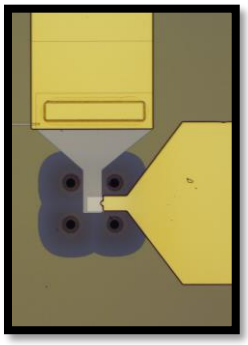

(a)

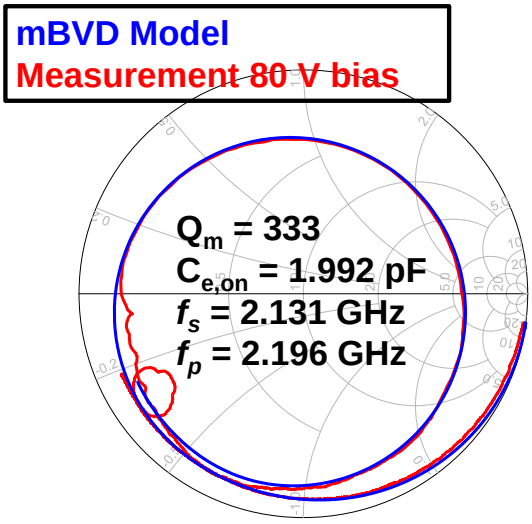

(b)

Fig. 2.19: (a) Photograph of a 2 pF BST FBAR and (b) measured frequency response with mBVD model parameters on the Smith Chart.

measured response around 2 GHz, where the variation in frequency is attributed due to fabrication tolerances (thicknesses of different layers across the chip). The active area of the fabricated BST FBAR occupies an area of 38 by 38 μm, and the fitted mBVD model provided Q_m and k_t^2 values similar to the ones of the previous design section. The spurious resonance seen the S-parameter response is attributed to the smaller size of the measured FBAR; however, through apodization, this resonance can be smoothened out [49]. While the FBAR with an approximate BST thickness of 770 nm required 80 V of DC bias to fully switch on, it must be noted that the applied electric field is dependent upon the fabrication process, deposition conditions of BST, and structure.

Moreover, previous works have demonstrated that the bias can be further reduced to less than 20 V [33] or boost converters utilized in mobile devices can be employed to achieve the required bias voltages [50].

2.7.2. Quad Bank Switchless BST Filter Bank Measurements

From the BST FBARs, post-fabrication, measured frequency response for the quad bank filter bank are depicted for each of the filter band's on-state frequency response (f_c = 1.74, 1.85, 1.94, and 2.05 GHz) in Fig. 2.20. Each of the four filters are selectively switched on while the remaining three bands are switched off. Table 2.5 describes the DC bias voltages required for controlling configuration for all states of the filter bank. Table 2.6 summarizes the results for each

Table 2.5
DC Biasing Configurations for Each of the Four Bands

Filter Path	**Input Node**	**Nodes A1/B1/C1**	**Nodes A2/B2/C2**	**Nodes A3/B3/C3**	**Nodes A4/B4/C4**	**Out**
f_c = 2 GHz	0	80/0/80	0/0/0	0/0/0	0/0/0	0
f_c = 1.9 GHz	0	0/0/0	80/0/80	0/0/0	0/0/0	0
f_c = 1.8 GHz	0	0/0/0	0/0/0	80/0/80	0/0/0	0
f_c = 1.7 GHz	0	0/0/0	0/0/0	0/0/0	80/0/80	0

filter band's on-state frequency response, and the DC bias voltage applied to the resonators in the filter bank is 80V to ensure that the k_t^2 of BST resonators reaches its maximum value. Compared to the simulation results, the insertion loss of the measured filter bank increased by an additional 2 dB. This can be attributed to a result of a number of different factors: i) thickness tolerances in the mass loading and BST layers thereby leading to frequency response variation, ii) greater than

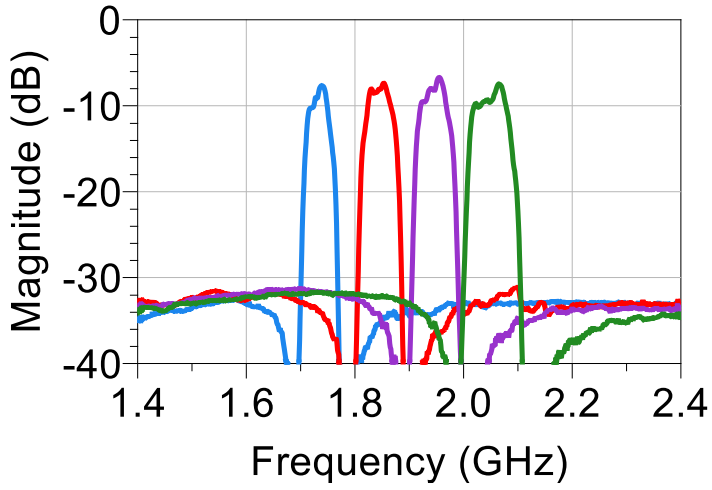

(a)

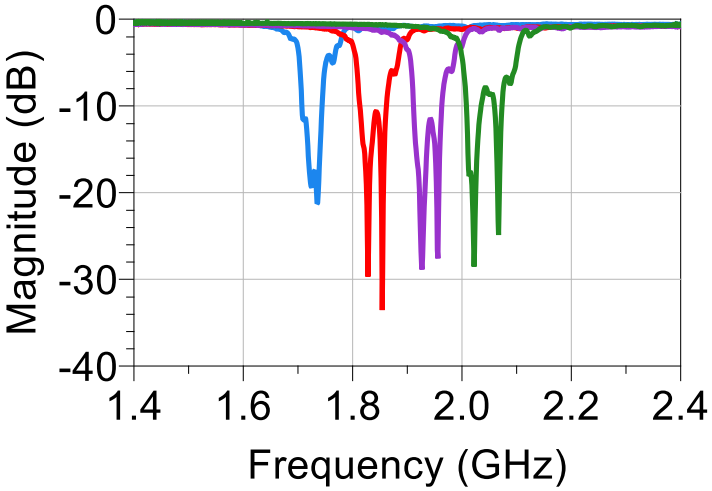

(b)

Fig. 2.20: Fabricated BST FBAR quad channel 2.5 stage filter bank: Measured (a) transmission and (b) reflection response when the BST FBARs are switched on for the respective filter.

expected BST loss, and iii) losses due to the interconnects between resonators. Loss improvement can occur through optimization of the BST resonator stackup, design of raised frame structures, and growth conditions [7].

Another key factor in the loss increase can be associated to additional dielectric loss from the BST capacitor utilized in conjunction with a shunt inductor of 1.9 nH as a phase delay element. While the BST FBARs maintained similar performance to simulation results, the fabrication conditions used for resonator operation are not optimal for relatively thicker, unbiased BST

Table 2.5
Measured Specifications for the BST Four Band Filter Bank

Specifications	*Band 1* *(2 GHz)*	*Band 2* *(1.9 GHz)*	*Band 3* *(1.8 GHz)*	*Band 4* *(1.7 GHz)*
f_c *(GHz)*	2.049	1.941	1.85	1.742
Min. IL (dB)	6.522	6.288	6.754	7.29
Rejection (dB)	30	30	30	30
3 dB FBW (%)	3.2	2.4	2.55	2.31

capacitors; the input MIM capacitor can also be implemented through an oxide or nitride layer or as external element to further reduce the insertion loss in such a switchable filter bank configuration. Compared to previous BST filter banks [41], the removal of a varactor, the lowest *Q* element in the design, at the output node also ensured that filters experience an overall less loss arising from both the on-channel filtering path and the adjacent off channels. It has been noted that in a multiplexed structure, losses from off-resonance frequencies can create a leakage path that degrades the passband IL performance [21], [51]. Due to additional mass loading beyond 60 nm of Pt to downshift the resonance frequency, the FBW also slightly decreases with the filter frequency operation. The return loss of the corresponding resonators maintains a value of approximately 10 dB or greater. Under zero DC bias excitation, all resonators are switched off, and the filter bank provides an isolation greater than 30 dB for all four filter paths across the frequency range of 1.4 – 2.4 GHz, as shown in Fig. 2.21.

For CA applications, two additional measurements are presented. For the quad channel BST filter bank, simultaneous multi-band operation is demonstrated in Fig. 2.22 when two channels (band 1 and band 3) of the quad band filter bank are switched on. There are no adjustments to the biasing voltages for BST FBARs in each of the filters or phase delay elements,

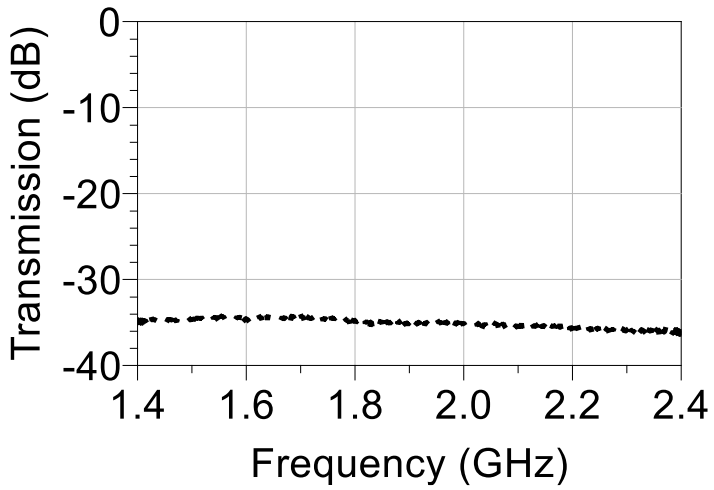

Fig. 2.20: Measured transmission response of the quad band bank to one output port, when all filters are switched off.

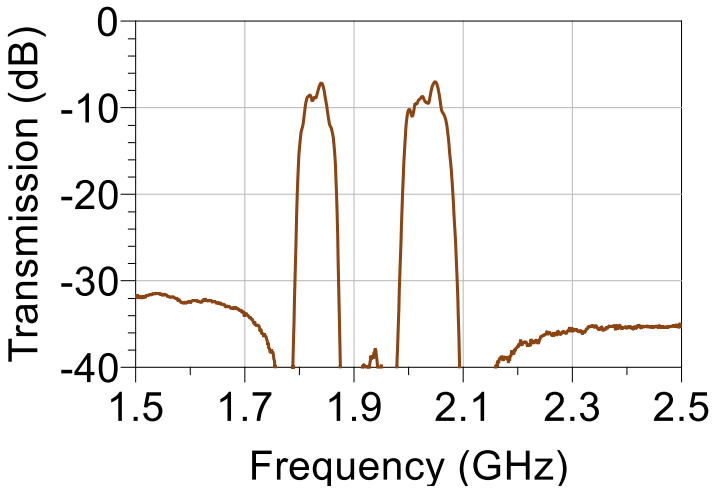

Fig. 2.22: Measured transmission response when channel 1 (2 GHz) and channel 3 (1.8 GHz) are simultaneously switched on.

and the minimum insertion loss does not degrade. The out-of-band response of band 1 and band 3 also provide comparable results to a standalone BST FBAR filter operating at those frequencies. For the high linearity requirements for CA multiplexers, work by the author extrapolated linearity and power handling measurements of a 2.5 stage BST FBAR filter, providing an IIP3 of 47 dBm [30]. More information is provided in the reference. A practical method to further linearity

improvement for BST based devices can be conducted by cascading equivalent larger area resonators.

The presented quad band filter bank incorporates a manifold-coupled multiplexing topology, where a phase delay at the input of each of the filter bands is utilized based on a combination of BST MIM capacitor and shunt inductor at the antenna node. Table 2.7 describes a comparison of this filter bank to other reconfigurable implementations. Compared to previous

Table 2.7
Comparison of performance of different reconfig. filter banks

Work	**Size** (mm^2)	***Channel IL (dB)***	***Stopband Rejection***	***Technology***
This	0.286	6.7	>30	BST
[41]	0.12	8.7	>27	BST
[87]	2.39	7 - 8.8	>50	CMOS SOI
[88]	33	3.2	>40	$LiTaO_3$ SAW + VO_2 switches

implementation [41], there is a noticeable reduction in the loading effect of the adjacent filter bands on the frequency response of the on-state filter away from its corresponding pass-band. Compared to a standalone BST FBAR based filter designed at the same frequency, there is no apparent degradation in the wideband transmission response at the passbands of the other three filters. Moreover, the minimum insertion loss across the four filters, despite the addition of an additional filter path, improves as a result of the removal of tunable elements. The greater than expected electric loss from the BST capacitor from measurement to simulation contributes to approximately 1.5 – 2 dB of insertion loss. Compared to other present reconfigurable filter banks, the presented topology occupies a small area as a result of BST intrinsic high permittivity. It must be noted for [88], the filter bank design is set for two channels. While the IL for this implementation is low, the corresponding isolation is limited to approximately 10 to 20 dB using the vanadium oxide switches, compared to the BST filter bank presenting an isolation close to 30 dB. The presented

design in this thesis utilizes both the electric-field induced piezoelectricity of BST and phase shifting matching technique [52] to selectively operate across multiple frequency bands from 1.7 to 2 GHz.

2.8 Chapter Conclusion

In this chapter, an entire overview of bulk acoustic wave resonator and RF filter design have been described. Starting from the single element, the FBAR, the principle and design for an acoustic resonator and subsequently, a ferroelectric BST based intrinsically switchable resonator has been presented. The BST resonators are the key enabling devices for the development of electronically reconfigurable BAW filters and filter banks. Measured results for fabricated BST FBARs demonstrated acoustic performance that matches the currently published ferroelectric BST values. However, there is still ongoing research to improve ferroelectric-based resonator performances at microwave frequencies in order to match modern standard piezoelectric resonators, which are on the orders of 10 magnitude greater. Systematic design approach for conventional ladder type filter design employing BST FBARs has been described.

Following this, a complete design, fabrication, measurement results for a quad band, switchless filter bank based on a manifold configuration is presented. Each of the four 2.5 stage BST FBAR filters provides switchability through DC bias control with IL ranging 6-7 dB and out-of-band rejection > 30 dB. Compared to a previously fabricated BST filter bank, no additional tuning varactors are employed to reduce loading effect of the off-state filters, which allows this configuration to achieve lower insertion loss. Instead, a manifold multiplexer configuration is used to achieve filter performance comparable to standalone filters. For CA applications, multiple bands, instead of one frequency band, have been turned on simultaneously by simply controlling

the DC bias voltages across the respective BST FBARs. This switchless ferroelectric implementation offers the potential to reduce system complexity and improve spectral efficiency along the RF front-end.

Chapter 3

Design and Characterization of BST Based Reconfigurable Filters

3.1. Chapter Motivation

Future transceivers within the RF front-end are expected to accommodate for a growing number of communication bands within a limited hardware area. While demands for wireless connectivity grows, nearly all frequency bands below 6 GHz that are suitable for mobile communications are already highly congested. Ensuring effective operation within an extremely congested radio spectrum has made the modern wireless communication systems highly complex and presents substantial challenges to system designers. One potential solution to resolve the limitation in space in end-user devices and facilitate efficient utilization of the available frequency spectrum involves the incorporation of frequency-agile components onto the RF front-end architecture. From the previous chapter, the ferroelectric BST based FBARs have been employed in the design of intrinsically switchable filter banks, where the filtering and switching functionalities are combined onto a single element. In this chapter, BST intrinsic property of electric-field induced piezoelectricity is further exploited in the design of RF reconfigurable filters, where FBW tuning or a complete change in the transfer function of the filter are demonstrated.

The first section of the chapter discusses BW reconfigurable filters without the use of additional tuning or external components. As there are inconsistency with 5G frequency allocations in different regions across the world, an acoustic filter with adjustable filtering characteristics to cover multiple bands remains an attractive prospect on the front-end [53]. The second part of the chapter incorporates a hybrid-based approach with external off-chip components directly connected onto a BST-on-Si platform to realize RF filters with adjustable filtering characteristics across two sets of design. RF filtering topologies using lumped-element (LE) resonators offer good trade-offs in terms of circuit size and tuning.

3.1. BST Bandwidth Reconfigurable Filters

As described in the previous chapter, the resonance frequency for BAW resonators is determine based on the thickness of the membrane and is fixed subsequent to the fabrication process. A number of approaches have been employed to attain frequency tuning abilities in SAW and BAW devices [54], [55]; for instance, methods involve changing piezoelectric properties through temperature and electric field variation have been proposed with limited tuning ranges [56]. Introducing external inductors and capacitors is one practical approach that has been demonstrated, considering the number of laminate inductors and MIM capacitors already deployed onto modern RF acoustic modules [21]. Fig. 3.1 depicts a mBVD model for a BAW resonator with external capacitors and the associated frequency shift. For inductors, the frequency offsets due to

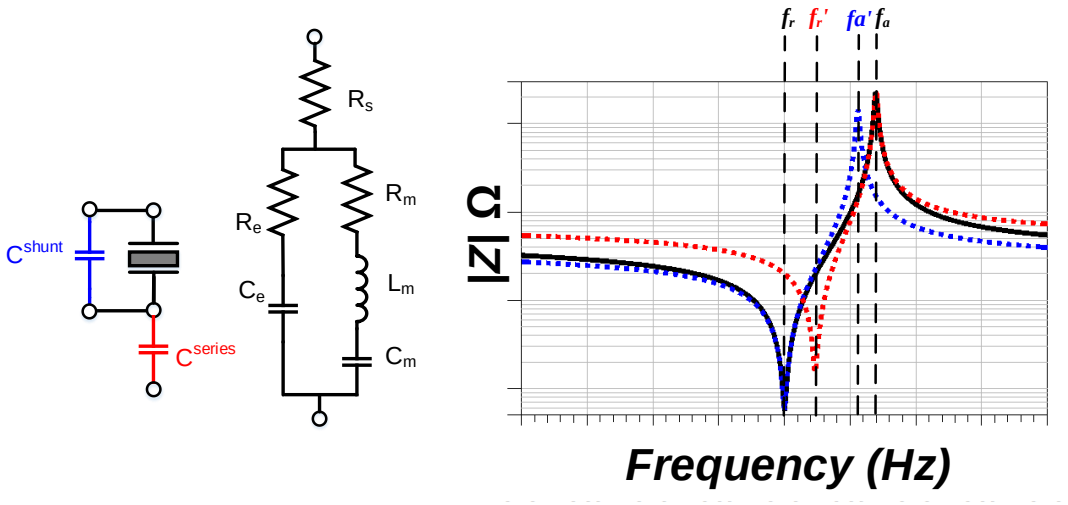

Fig. 3.1: Combination and effect of capacitors with a BAW resonator. Substituting inductors for the capacitors would reverse the frequency shift but is no longer limited by the associated k_t^2 of the device.

shunt and series elements are reversed (i.e. outwards instead of inwards).

Using the same principle, intrinsically switchable BST FBAR filters can be designed to achieve bandwidth variation, through additional shunt or series connected FBARs. The governing

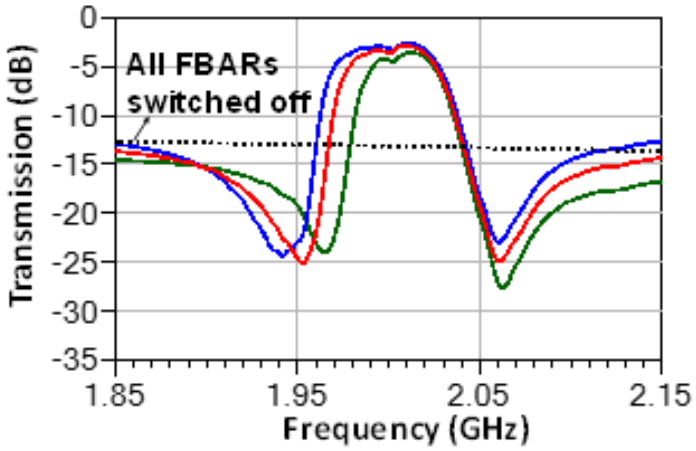

Fig. 3.2: Measured transmission response for the measured bandwidth reconfigurable four state FBAR filter unit cell across all of its states.

equations for the shift in series resonance (f_r') and anti-resonance (f_a') frequencies are denoted in (3.1), (3.2), and (3.3):

$$f'_r = f_r\sqrt{1+\gamma/(1+\alpha C_{e2}/C_{e1})} \tag{3.1}$$

$$f_a' = f_a\sqrt{1-\frac{\gamma}{\gamma+1}/(1+C_{e1}/\alpha C_{e2})} \tag{3.2}$$

$$\gamma \cong 8K_t^2/\pi^2 \tag{3.3}$$

Fig. 3.2 depicts the measured transmission response of the device, where the fabricated BST filter not only switches on or off through an applied DC bias voltage but also transitions between three different FBW states of 3%, 2.5%, and 2%, respectively. More information regarding the design, fabrication process, and results is discussed in greater detail in [42].

3.2. BST Acoustic Wave Lumped Element Resonators

From the previous section, the use of external capacitors in BAW filters provide moderate tuning capabilities that are limited to the k_t^2 of the associated resonator. When the external inductors are instead substituted in for the capacitors, f_s' shifts to a lower frequency and conversely, f_a' shifts to a higher frequency, which allows for a potential increase in the overall effective coupling. Fig. 3.3 denotes the schematic and coupling matrix diagram (CMD) for a BST based acoustic wave lumped resonator (AWLR), where the BST FBAR is coupled with an inductor, L_p, and an additional trimming capacitor, C_t. While the standalone BST FBAR exhibits a tightly coupled series and shunt resonance, this limits the overall k_t^2 and sets the FBW for FBAR based filters [57]. By creating an AWLR module, the resulting impedance response exhibits a single high Q reflection pole (R_H) at the original resonance frequency of the FBAR and two distinct

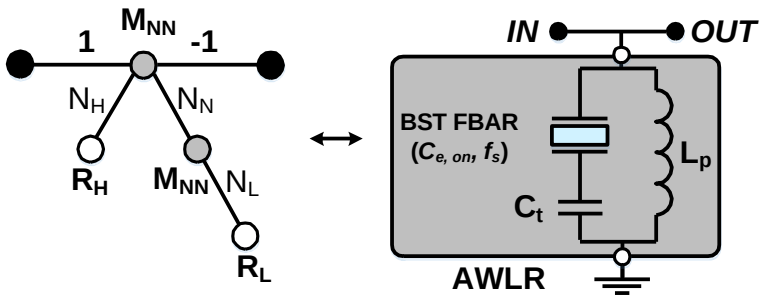

(a)

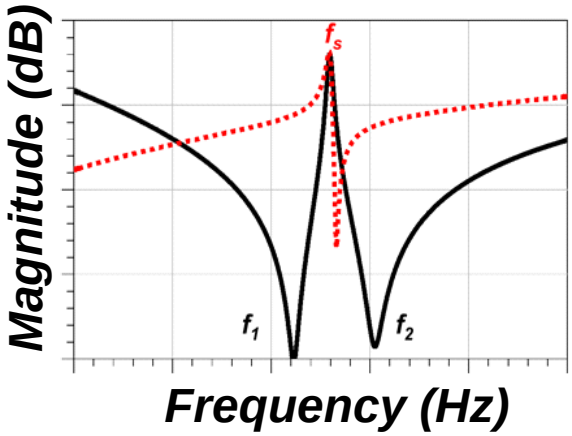

(b)

Fig. 3.3: (a) Coupling Diagram and schematic (b) and corresponding frequency response of the BST-based AWLR, where $C_{e,on}$ denotes the electrical capacitance extracted in the mBVD model and C_t and L_p are external components within the AWLR.

transmission zeros, f_1 and f_2. The original high Q resonance of the acoustic resonator remains persevered and the quality factor does not degrade from L_p. The two transmission zeros appear at the locations where there is cancellation between the impedances of the series (L_m, C_m, and C_t) and parallel (L_p and C_p) resonators. In other words, through appropriate selection of the L_p and C_t, the locations are the transmission zeros are adjustable and denoted by (3.4) [58]:

$$f_{1,2} \tag{3.4}$$

$$= \frac{1}{2\pi}\sqrt{\frac{\omega_s^2}{2} \pm \sqrt{\frac{\left(C_m L_p \omega_s^2 \omega_p^2 + \omega_s^2 - 2\omega_s\omega_p + \omega_p^2\right)\left(C_m L_p \omega_s^2 \omega_p^2 + \omega_s^2 + 2\omega_s\omega_p + \omega_p^2\right)}{2} + \frac{\omega_p^2}{2} + \frac{C_m L_p \omega_s^2 \omega_p^2}{2}}}$$

R_L denotes the low-Q resonance associated with the parallel combination of Lp and C_m of the mBVD model, and the coupling coefficients can be extracted by fitting to circuit simulations. The AWLR serves as the base element, where also exploiting BST's electrostriction property gives rise for a number of reconfigurable filtering transfer functions.

3.3. BST AWLRs Filter Simulations

The two filter designs presented in this work are based on an all-pass network that are cascaded with coupled BST AWLRs. Fig. 3.4 depicts the generalized circuit schematic and a transmission response graphic. The filters consist of AWLRs resonators coupled to source-to-load transmission lines with impedances Z, coupled to each other with coupling coefficient k_{xy}. As stated in the previous section, the location of the reflection (Design 1) and transmission (Design 2) zeros are determined by BST AWLR elements, and the impedance inverters, Z_{in}, Z_{ip}, Z_{12}, $Z_{N-1,N}$ are utilized to modify the coupling coefficients and overall filter characteristics.

For the two filter designs (Bandstop-to-all-pass and bandpass-to-all-reject filter) presented in this work, the BST FBARs are simulated with their corresponding mBVD model considering electromechanical coupling coefficient and electrical quality factor as: k_t^2 = 7%, Q_m = 300, and Q_e = 60. The impedance inverters are realized in its π-equivalent form using lumped element equivalent components, where the capacitors shared at the end of each inverter are combined to reduce the overall number of external components in the circuit. Simulations has been conducted for both designs utilizing, on-chip capacitors and inductors, but expected quality factors at 2 GHz results in a significantly degraded filtering response. Therefore, the two designs employed off-ship surface mount device (SMD) 0201 sized components from Murata. A combination of ADS and Ansys High Frequency Structure Simulation Software (HFSS) are utilized to account for all layout

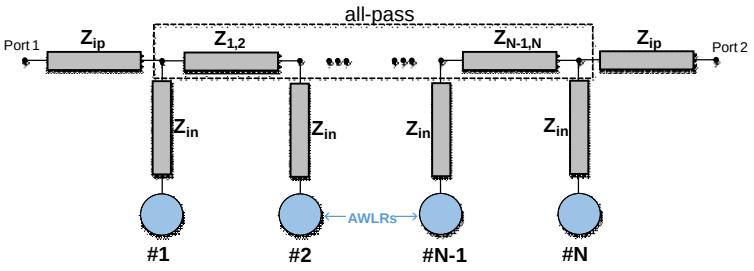

(a)

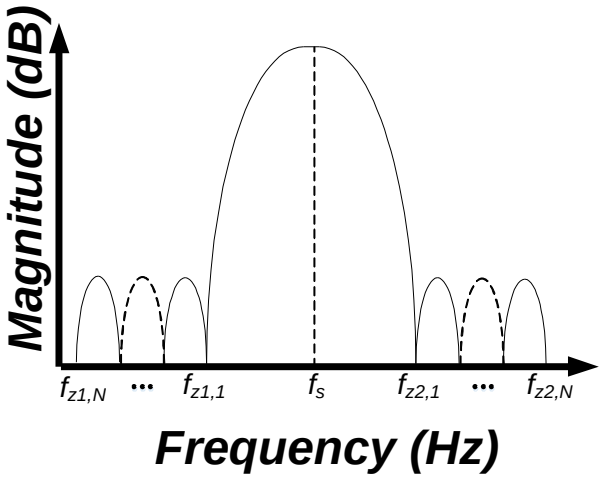

(b)

Fig. 3.4: (a) Schematic for Nth order AWLR filter based on all-pass network and impedance inverters (b) conceptualized frequency response for the all-pass network portion.

parasitics and mutual coupling effects of adjacent inductors. Initial designs are conducted assuming an on state electrical capcitance of 2 pF and resonance frequency of 2 GHz for BST FBARs; however subsequent to fabrication, direct measurement of BST FBARs near the location of the filters are utilized to 1) determine the fabricated resonant frequency, which shifts slightly due to fabrication tolerances and 2) reoptimize the SMD values.

3.3.1. Bandstop-to-All-Pass (BS-to-AP) Filter

Fig. 3.5 depicts the finalized circuit schematic for the design and Table 3.1 list the corresponding SMD components. For both designs, the high resistivity biasing lines used to switch

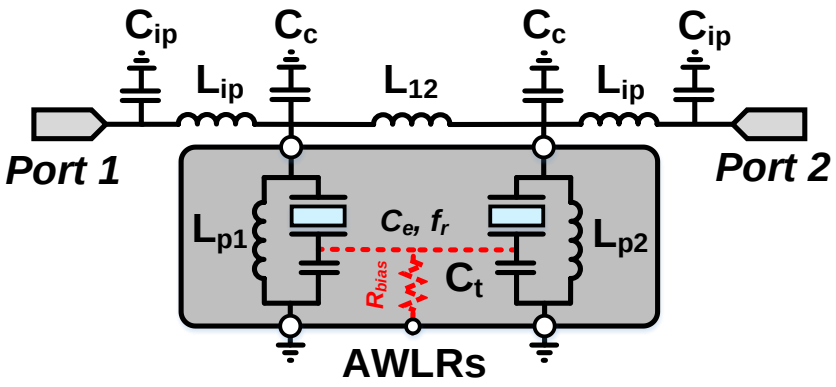

Fig. 3.5: Circuit schematic of the BST FBAR-based bandstop-to-all-pass circuit.

Table 3.1
SMD Component List

Parameter	**(BS-to-AP) Model #**
L_{ip}	LQW04AN5N0C00
C_{ip}	GJM0335C1ER90WB01
L_{12}, L_p	LQW04AN6N6C00
C_c	GJM0335C1E1R8WB01
C_t	G RM0335C2A1R4WA01

on and off the BST FBARs is increased to 4 kΩ to improve the overall filtering response. The corresponding frequency response for both states is provided in Fig. 3.6. For the BS-to-AP circuit, three impedance inverters, Z_{12} and Z_{ip}, are used to couple with the AWLR modules. When a DC bias voltage is applied across the BST FBAR, the resonator is switched on, and the circuit displays

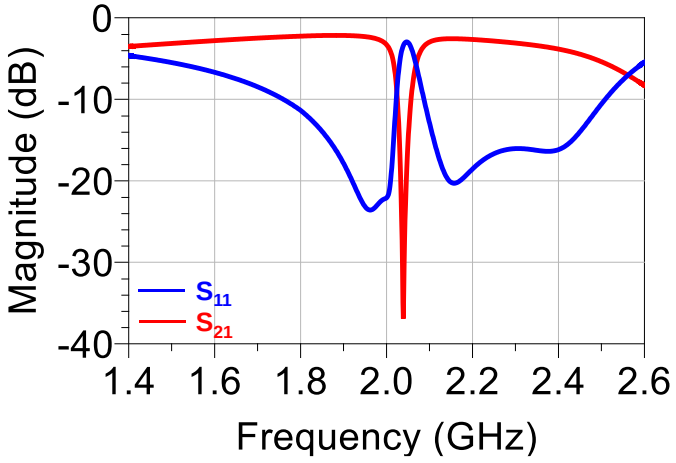

(a)

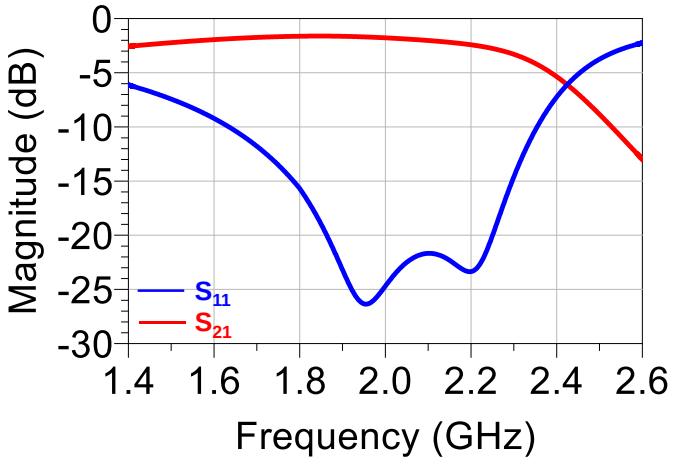

(b)

Fig. 3.6: Simulated reflection (blue) and transmission (red) response of the BST AWLR based bandstop-to-all pass circuit when the BST FBARs are switched (a) on or (b) off.

a bandstop response at a center frequency of 2.039 GHz with a notch magnitude exceeding 35 dB and 10 dB FBW of 3%. In the second mode of operation (zero DC bias), the resonator acts as a pure capacitor and the circuit exhibits an all-pass response with an IL of 2.2 dB. It must be noted that there is a tradeoff between the matching of the all-pass state and BW of the bandstop state, due to the variation in electrical capacitance between on and off BST FBARs.

3.3.2. Bandpass-to-All-Reject (BP-to-AR) Filter

Fig. 3.7 depicts the finalized circuit schematic for the design and Table 3.2 list the corresponding SMD components. For the BP-to-AR circuit, an additional set of impedance inverters, Z_{in}, is used to couple the AWLR. Thus, a bandpass mode of operation centered at 2.15 GHz with FBW of 2.5% is shown when the BST resonators are switched on, as demonstrated in Fig. 3.8. In the second state when zero DC bias is applied to circuit, the resonator acts as a pure capacitor and the circuit exhibits an all-reject response. Design

Table 3.2
SMD Component List

Parameter	(BP-to-AR) Model #
L_{in}	LQW04AN8N6C00
C_{in}	GJM0335C1ER30BB01
L_{ip}	LQW04AN4N7C00
C_{ip}	GGJM0335C1E1R3WB01
L_{12}	LQW04AN4N3C00
C_c	GJM0335C1E1R8WB01
L_{p1}	LQW04AN11NJ00
L_{p2}	LQW04AN18NJ00
C_t	GRM0335C2AR50WA01

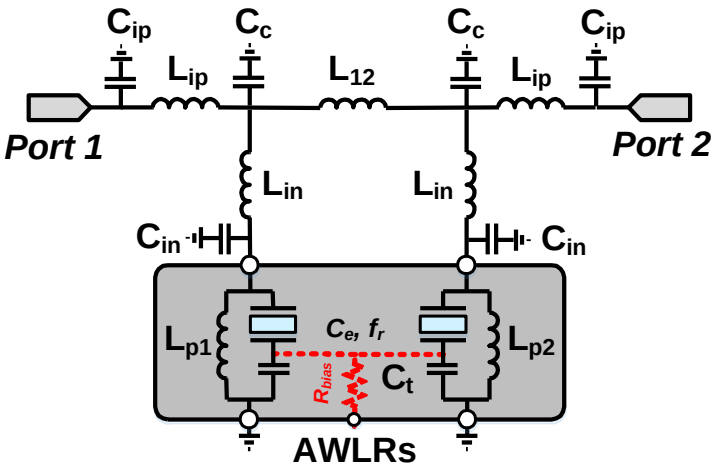

Fig. 3.7: Circuit schematic of the BST FBAR-based bandpass-to-all-reject circuit.

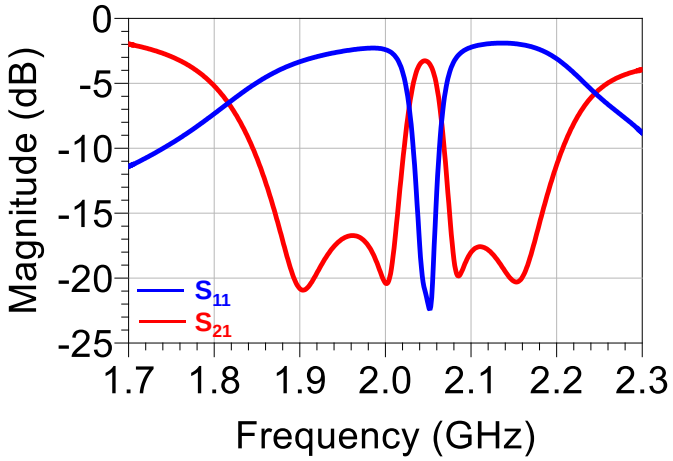

(a)

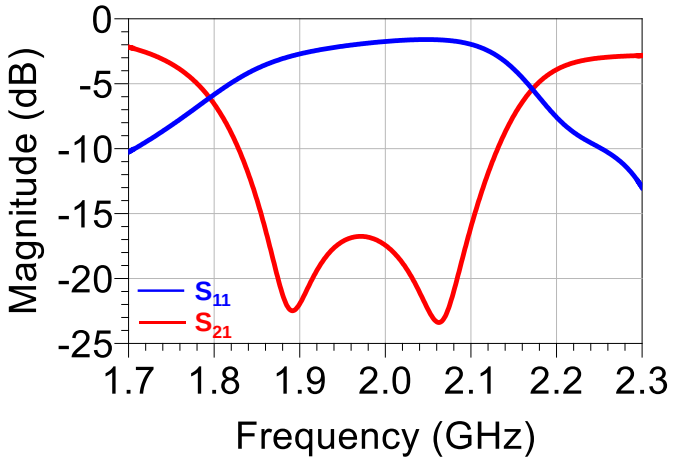

(b)

Fig. 3.8: Simulated reflection (blue) and transmission (red) response of the BST AWLR based bandpass-to-all-reject circuit when the BST FBARs are switched (a) on or (b) off.

tradeoffs for this filter are between the isolation of the all-stop state and BW of the bandpass state, which through adjustment of the corresponding shunt inductors, L_{p1} and L_{p2}, for the AWLR elements could achieve greater than 17 dB across the entire frequency range.

3.4. Fabrication and Experimental Results for BST AWLR Filters

The reconfigurable BST FBAR filters are fabricated following the same procedure that is described in chapter 2. Subsequent to fabrication, individual BST FBARs are measured to determine electrical and acoustic characteristics. Surface mount components are then silver epoxied onto the substrate, and the BST chip is heated to 110°C for 5 minutes. A vector network analyzer and Cascade microtech probe station with 250 µm pitch GSG probes. Bias voltages of 80 V are solely applied through bias tees and a single DC probe pad utilized to bias both resonators in the circuit. The off-chip SMDs passive components are manually mounted onto the Si substrate using silver epoxy. Fig. 3.9 depicts a photograph of the fabricated bandstop-to-all-pass filter and bandpass-to-all-reject filter prior to SMD component integration. The active area of each

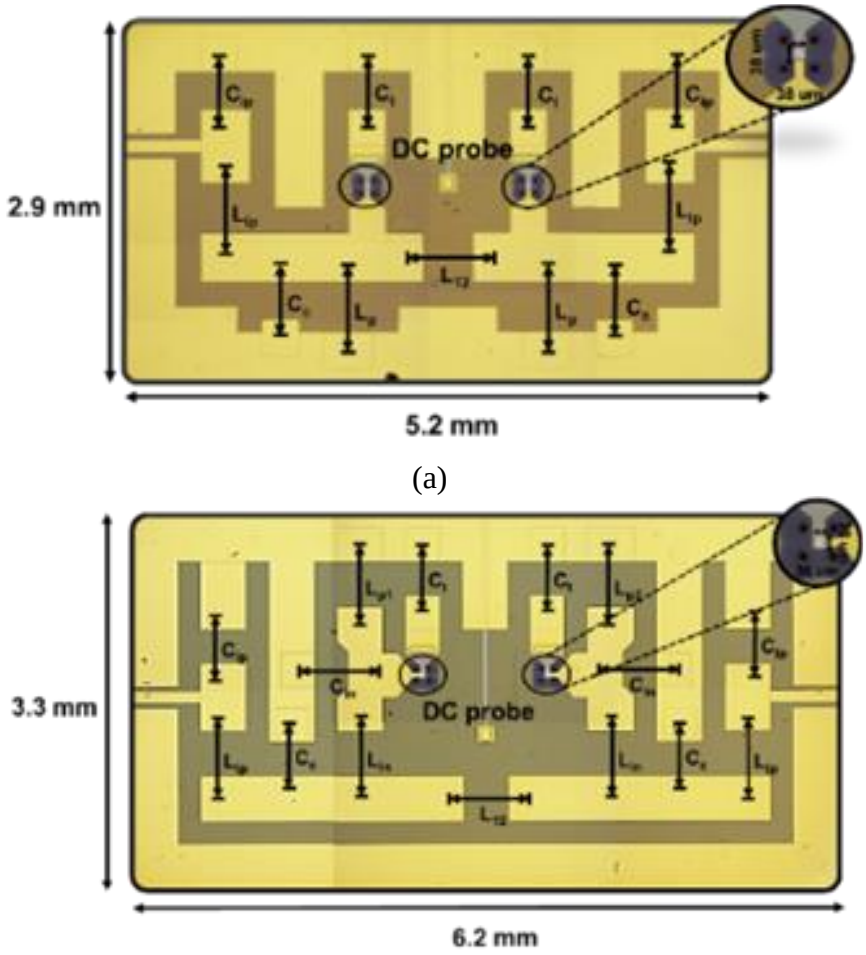

Fig. 3.9: Manufactured prototype, excluding the surface mount LC components, of the BST FBAR based (a) BS-to-AP circuit and (b) BP-to-AR circuit with inset view of the active resonator area.

fabricated BST FBAR in both designs occupies an area of 38 by 38 μm, while the total area of the BS-to-AP and BP-to-AR networks are 5.2 mm by 2.9 mm and 6.2 mm by 3.3 mm, respectively.

The measured S-parameters of the AWLR FBAR based circuits in the on and off state are displayed in Fig 3.10 and 3.11, respectively. In particular, Fig. 3.10 demonstrates the BS-to-AP circuit and its RF performance is summarized as follows. In the bandstop mode of operation when the AWLRs are on, the circuit exhibits a notch at 2.043 GHz with a maximum rejection of 27 dB, 10 dB FBW of 1.86% and 3.2 dB of insertion loss in its passband areas. In the all-pass state, the AWLRs are off and the overall circuit exhibits an all-pass response with a minimum insertion loss

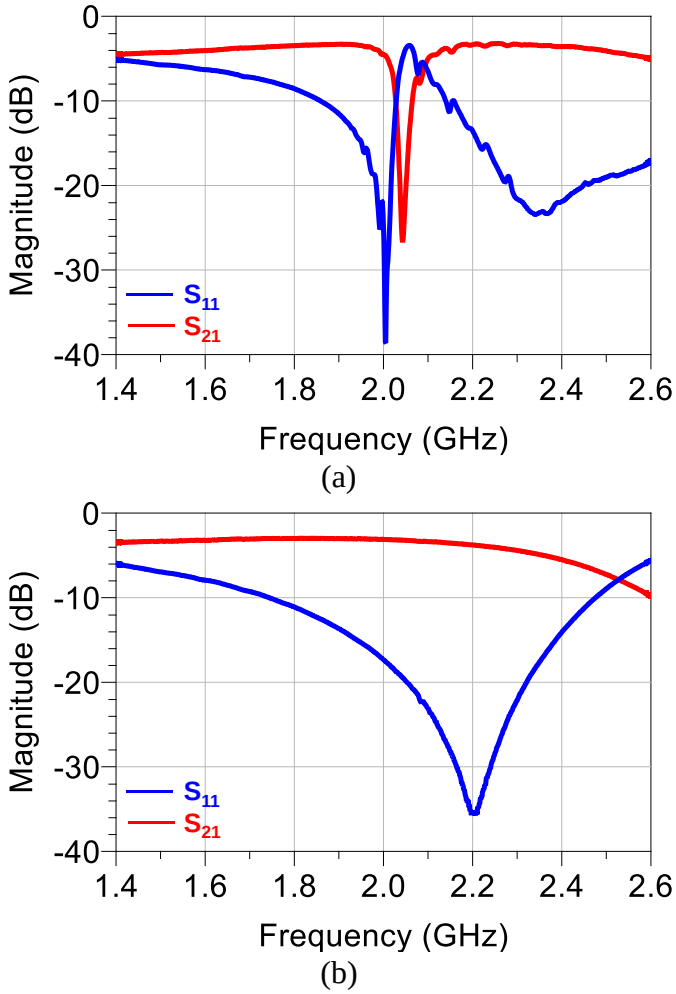

Fig. 3.10: Measured reflection (blue) and transmission (red) response of the BST AWLR based bandstop-to-all-pass circuit when the BST FBARs are switched (a) on or (b) off.

of 3.5 dB between 1.8 and 2.2 GHz. The second circuit in Fig. 3.10 exhibits a bandpass mode of operation with a passband centered around 2.13 GHz with a FBW of 2% when the AWLR is on. Under zero DC excitation, an isolation >15 dB is obtained between 1.92 and 2.23 GHz. For both circuits, the transmission and reflection peaks are in close proximity with the simulated results.

Overall, the minimum insertion loss of the BS-to-AP and BP-to-AR circuits increased by approximately 1 dB. This discrepancy can be attributed to a number of factors: specifically, greater than expected electrical and mechanical losses in the BST layer and interconnect losses. As mentioned previously, a quality factor of 300 is reasonable with current BST resonators used in

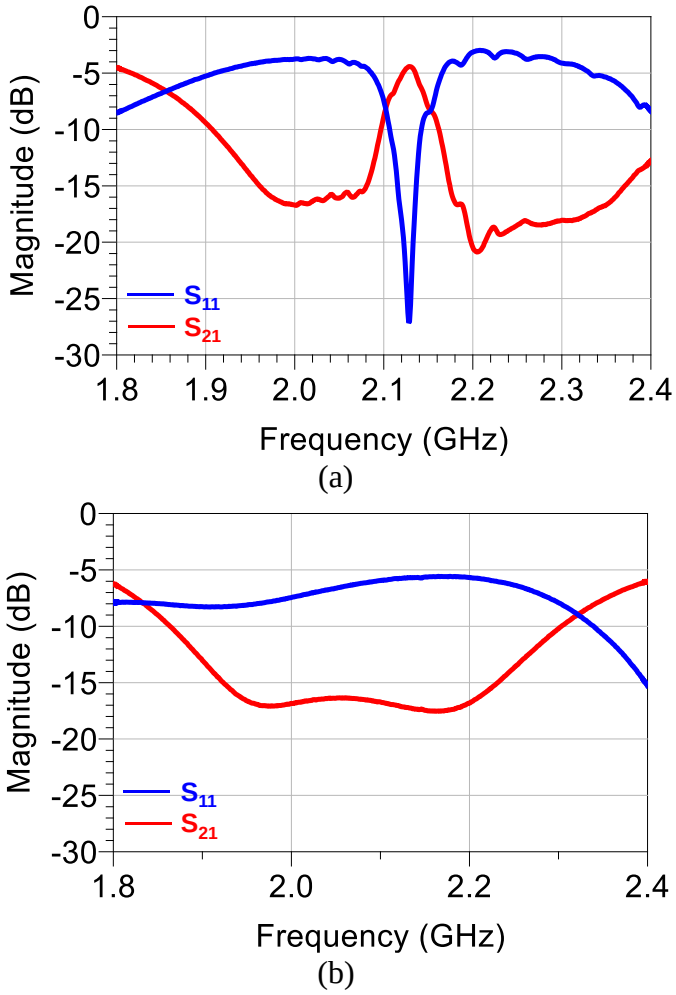

Fig. 3.11: Measured reflection (blue) and transmission (red) response of the BST AWLR based bandpass-to-all-reject circuit when the BST FBARs are switched (a) on or (b) off.

reconfigurable filter topologies; however, small unwanted active regions that occur as a result of misalignment during the fabrication process lead to spurious resonances and loss contribution of the BST FBAR. Compared with the simulation results, the measured results are in good agreement, accounting for the LC component tolerances (±2%). As a result of heating the substrate during the mounting process with silver epoxy, the values of the LCs can further shift, but the circuits still successfully validate the reconfigurable AWLR-based transfer function concept. Further optimization of the BST deposition parameters along with the contact layer for the BST-on-Si platform can be conducted to improve the performance of the filters.

3.5. Absorptive Filters based on BST FBARs

The previous section demonstrated experimental results for BST based reconfigurable filters that could reflect undesired signals away from the frequency band of interest and also reconfigure into a different state based on the state of the associated BST FBARs. In some cases however, the reflection of signals to another part of the RF front-end is not ideal. Similar to the bandstop-to-all-pass filter design presented, BST FBARs could also be applied in an absorptive or reflectionless bandstop filter [59]. Rather than attenuating signals or noise, the filters operate by absorbing and dissipating the undesired frequencies, usually through lossy components in the circuit. Applications of absorptive filters can be seen as power limiters [60], [61], which mitigate unwanted electromagnetic interference and maintain signal integrity in electronic systems.

Fig. 3.12 depicts the conceptualized diagram for an invert-coupled section that could realize an absorptive bandstop filter, which utilize a hybrid coupler topology. Each of the coupled ports of the topology consist of a set of BST acoustic resonators that reconfigurably switch on or off through an applied DC bias voltage to excite different acoustic resonances. It must be noted that chains of BST FBARs, each with distant anti-resonance frequencies, can also be substituted in to realize multi-bandstop, absorptive operation. The design of the filter starts

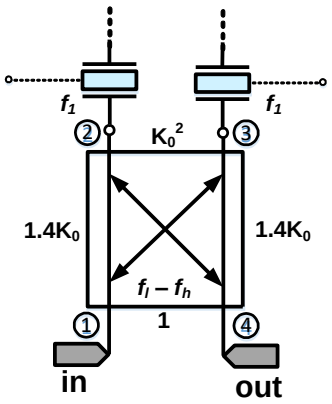

Fig. 3.12: Conceptual schematic of the absorptive notch filter with AWLR BST FBARs setting the notch frequency.

with the resistance at the anti-resonance frequency, f_p, of one BST FBAR while the rest of the resonators in the chain are switched off, determined by (3.5) for series connected chains. The size of the resonator are set such that the resistance at f_p match and can be calculated based on the required electrical capacitance. From the resistance of the FBAR chain at anti-resonance, the inverter impedance and subsequent first order LC equivalent are determined.

$$R_{p,x} = real\left\{\frac{(j\omega L_m + \frac{1}{j\omega C_m} + R_m)(\frac{1}{j\omega C_e} + R_e)}{\frac{1}{j\omega C_e} + R_e + R_m + j\omega L_m + \frac{1}{j\omega C_m}}\right\} + R_{e,chain} \tag{3.5}$$

Fig. 3.13 demonstrate the preliminary results for a simulated AWLR based absorptive

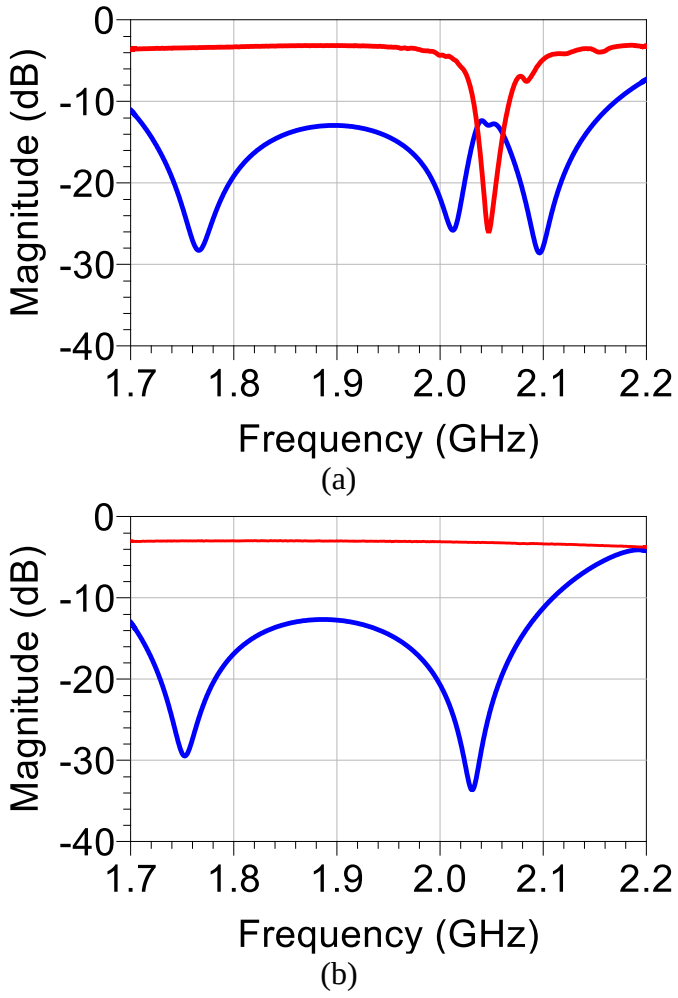

Fig. 3.13: Measured reflection (blue) and transmission (red) response of the BST AWLR based absorptive filter when the BST FBARs are switched (a) on or (b) off.

notch filter, which utilized lumped element components to realize the coupler. For improved miniaturization and additional notch FBW, off-chip coupler could be utilized. When both BST FBARs are switched on, a bandstop frequency at 2.013 GHz with a depth exceeding 22 dB is realized. Moreover, the return loss of the circuit is greater than 11 dB across the frequency range of the coupler even at the notch frequency, verifying the absorptive filter property. The minimum insertion loss from either bandstop or all-pass state is approximately 3.8 dB due to the number of limited *Q* SMD components.

3.6. Chapter Conclusion

Within this chapter, multiple designs for intrinsically switchable BST FBAR based filters with filtering transfer function variations are designed and presented. The first design incorporated chains of series or shunt connected BST FBARs in a ladder type acoustic filter design, which allows for filter passbands with bandwidth reconfigurable states. The primary benefit of this approach allows for an adjustable passband that does not require external tunable elements such as varactors or switches. As these elements are typically magnitude greater in size or reduced quality, the BW reconfigurable BST filter maintains both electrical and physical characteristics similar to a standalone filter.

The second portion this chapter utilizes the electrostriction property of BST in order to realize with transfer-function adaptivity in terms of transfer function type in two separate reconfigurable filters. For the first time, RF filters with unique reconfigurable transfer function characteristics (all-pass-to-bandstop response and bandpass-to-all-reject response), bandwidths that not limited by the coupling of the acoustic resonator components, and at significantly higher operational frequencies than what has been demonstrated previously at the time (2 GHz, which is

four times higher than in [62], [63]). The reconfigurable filter prototypes are directly integrated onto the Si wafer after BST thin film growth and are able to reconfigure their filtering response through application of a DC bias voltage. While not demonstrated with the first two prototype designs, appropriate design trade-offs between the number of AWLRs and impedance inverters and circuit topology would allow for a highly increased effective FBW of the filter, without noticeable degradation of the effective *Q*.

Chapter 4

mm-Wave Mode-Switchable FBAR Based on Ferroelectric ScAlN

4.1. Chapter Motivation

With the development of wireless communications into the millimeter wave bands, acoustic based filters must operate not only at higher frequency, but also provide wider FBW to support increasing data rates. However, scaling conventional BAW devices to address these requirements leads to a number of issues [64]. The operating frequency of conventional BAW resonators is dictated by the piezoelectric material membrane thickness. In BAW devices, the thickness of the entire membrane (electrodes plus piezoelectric transduction layer) is approximately one half acoustic wavelength; hence as the frequency of operation increases, the membrane thickness must be reduced. At the same time, in order to maintain low ohmic losses, the thicknesses of the electrodes must be comparable to the skin depth. At higher frequencies, reducing the piezoelectric/transduction layer while maintaining electrode thicknesses will lead to a significant degradation in k_t^2, as more of the acoustic energy becomes confined in the electrodes. Therefore, there is a tradeoff between the coupling efficiency and electric loss when determining the thicknesses of the piezoelectric and electrode layers, especially at mm-Wave frequencies that require very thin resonator membranes. Moreover, thinner piezoelectric membranes introduce

reliability and processing challenges for conventional sputtering techniques, as summarized in [53] with additional acoustic loss arising from poorer film quality. The combination of these effects makes the frequency scaling of the BAW resonators not practical at high microwave and mm-wave frequencies.

To overcome material limitations, several alternative piezoelectric/transducer materials have been extensively studied in order to improve the overall figure of merit (FOM = $Q \bullet k_t^2$) of acoustic devices. Lithum niobate ($LiNbO_3$) with its large electromechanical coupling and wide range of phase velocities within an acoustic resonator structure has been one widely explored material. Utilizing $LiNbO_3$ in tandem with an overtone resonator design is a potential solution to produce acceptable k_t^2 devices [65], [66]. As mentioned in the first chapter, another unique ferroelectric that has continued to receive interest involves doping AlN with Sc in order to significantly improve the piezoelectric coefficient, which correlates to the coupling [18],[67]. AlN based bulk acoustic wave resonators provide modest k_t^2 values ranging from 5-6%, but transitioning to scandium aluminum nitride based devices for improved FBW offers compatible fabrication requirements.

To overcome frequency scaling limitations of single layer FBARs, one approach relies on the excitation of higher-order modes (Fig. 4.1); however, such devices still suffer from a large drop off in k_t^2 as a function of their operating frequency [20],[64]. For instance, Fig. 4.1 shows two resonators operating at the same frequency, one operates at the fundamental mode (left) while the other is excited at its n^{th}, in this case 3^{rd}, order mode (right). In the overmoded structure, although the ratio of strain energy inside the electrodes to the energy inside the piezoelectric material is reduced, the electromechanical coupling coefficient is still $1/n^2$ of the fundamental mode. Due to the spatial correlation between the applied uniform RF field within the bulk of the resonator and

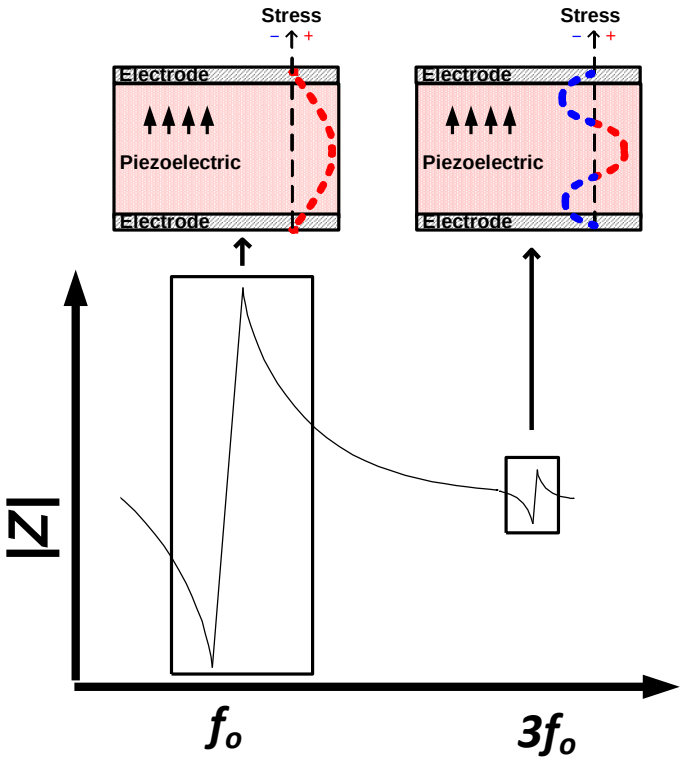

Fig. 4.1: High frequency scaling limitation of conventional fundamental (left) and higher order mode (right) BAW resonator.

the stress profile of the higher order mode, which has multiple zero crossings, the coupling between the RF field and higher order mode acoustic resonance is drastically reduced. Hence the coupling between the electrical and the acoustic domain for the n^{th} order mode effectively occurs in $\frac{1}{n}$ of the resonator thickness. To rephrase, the k_t^2 for an overmoded FBAR drops due to charge cancellation arising from multiple zero crossings in the stress profile within the piezoelectric.

The work conducted in this chapter demonstrates an alternative approach, employing an alternating combination of AlN and ScAlN layers in a polarity controlled multilayer FBAR. Fig. 4.2 depicts a conceptualized graphic behind the stress and resulting charge fields with this approach, where the piezoelectric coefficient profile correlates to the stress profile of an excited higher order mode, avoiding charge cancellation. The initial section discusses the theory behind the multilayer FBAR. Subsequent to that, the design and simulation results of a Trilayer AlN-

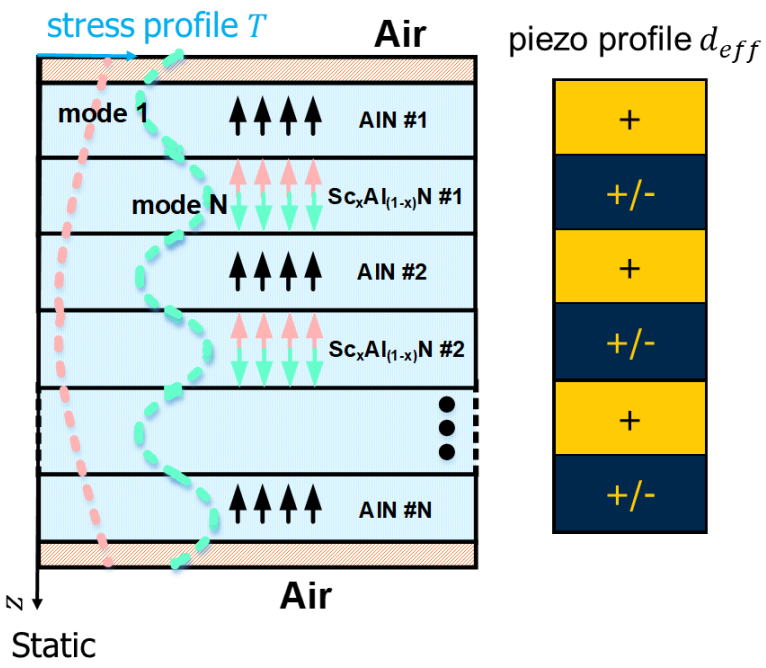

(a)

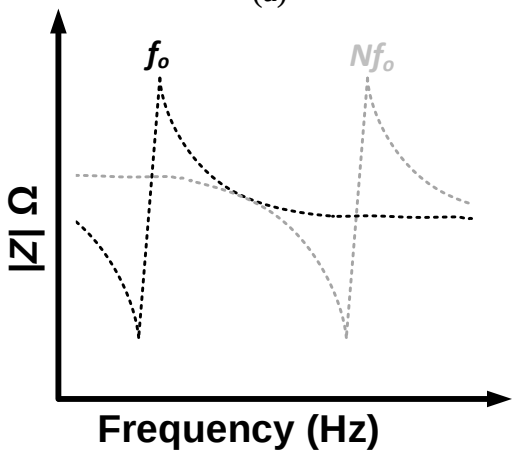

(b)

Fig. 4.2: (a) Polarity controlled multilayer FBAR structure, where charges add up coherently. The piezoelectric profile is denoted in blue and yellow, where ScAlN switches polarization to obtain the frequency response (b).

ScAlN FBAR along with finalized thicknesses are discussed. The work done for this thesis also investigates fabrication processes and techniques used for nitride based films. A quick overview of different etching techniques is presented prior to the fabrication process. Following that, measurement and polarization switching results along with a discussion are provided.

4.2. Piezoelectric Crystal Quality at mm-Waves

As mentioned in chapter 1, there are a number of factors, which limit current frequency scaling of single layer BAW devices, one of the major ones noted as the degradation of crystal quality with thinner piezoelectric films. Fig. 4.1 denotes the quality factor scaling of reported BAW resonators across a number of reported sputtering deposition techniques. Fig. 4.1 (b) depicts reported x-ray diffraction (XRD) measurements of sputtered AlN films as the thicknesses reach sub 200 nm. It must be noted that acoustic losses scale with $1/f^2$, due to the reduction in not

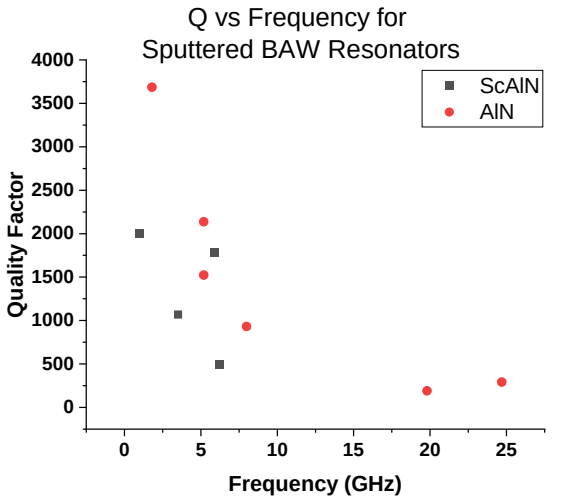

(a)

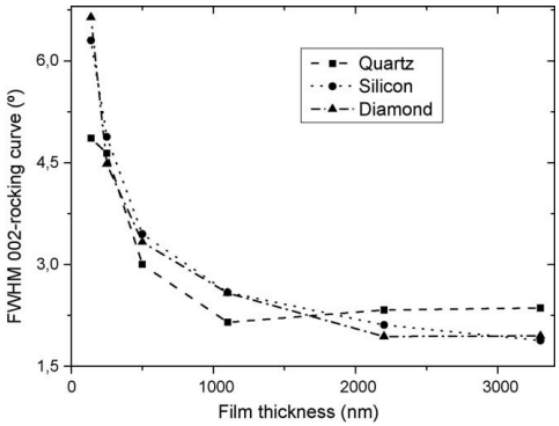

(b)

Fig. 4.3: (a) Reported state-of-the-art ScAlN and AlN BAW resonators FOM based on sputtering deposition techniques and (b) FWHM measurement for sputtered AlN with thicknesses, taken from [89].

only the thickness but also area, in order to maintain the same impedance [19]. Moreover, additional effects, such as spurious lateral modes, contribute to the loss from a resulting reduction in area-to-perimeter ratio.

By utilizing a polarity controlled multilayer structure, the overall thickness of the membrane is comparable to current single layer piezoelectric BAW resonators at sub-6 GHz, which thereby changes quality factor scaling to 1/*f*. However, each layer within a multilayer structure is still below conventional thicknesses at RF frequencies. To address concerns of sputtered films, which gradually lose crystallinity as the thickness reduces, molecularly beam epitaxial (MBE) films are employed. Already, it has be reported that under optimized growth conditions, ScAlN films exhibit a full width at half maximum (FWHM) of 400 arcsec for (002) plane rocking curve scan, while maintaining wurtzite phase at high Sc concentrations of 34% [90]. On metal/Si templates, research work demonstrates the (002) plane XRC FWHM of 2200 arc sec, which is still a significant improvement compared to conventional sputtered techniques (> 2°) [91]. Finally, ferroelectricity has been demonstrated at down to 5 nm MBE grown thicknesses [92].

4.3.k_t^2 Analysis for an Alternating Polarization Excited Harmonic Resonance

As shown in Fig. 4.2 (a), the multilayer BAW resonator designed in this work is comprised of alternating layers of piezoelectric AlN and ferroelectric ScAlN, where there are no intermediate electrodes between each layer. This structure is capable of switching between two modes, the fundamental mode and N_{th} mode, where a DC electric field is only required during the polarization switching process within the ferroelectric layers. Piezoelectric AlN layers exhibit a positive piezoelectric profile, while the ScAlN layers provide either a positive or negative piezoelectric

profile depending on the poling electric field applied by a DC bias across the top and bottom electrodes. Previous work conducted with multilayer BST FBARs demonstrated theoretically and experimentally that individual higher-order modes can exhibit effective k_t^2 that match the coupling of the fundamental mode [20].

In chapter 2, a 1D model analysis of thickness-extensional mode in a single layer FBAR is provided. From a general solution for the particle displacement, the k_t^2 is presented as a function of measurable quantities, the series and parallel resonance. While this formula is widely used due to ease of determining frequency values during measurement, in the context of a multilayer FBAR, no insight is provided in the contribution of different layers onto the overall k_t^2. Another approach, referred to as Berlincourt's formula, determines the effective electromechanical coupling coefficient can based on the field quantities, stress (*S*) and electric field (*E*), and the boundary conditions of the resonator [68]:

$$K_{eff}^2 = \frac{U_m^2}{U_e U_d} \tag{4.1}$$

$$U_m = \frac{1}{2}\int_V d_{eff}(TE)dV \tag{4.2}$$

$$U_e = \frac{1}{2}\int_V sT^2 dV \tag{4.3}$$

$$U_d = \frac{1}{2}\int_V \epsilon E^2 dV \tag{4.4}$$

where U_m, U_e, and U_d describe the mutual, elastic, and electrical energy while s and ϵ are the compliance and permittivity. In the case of an AlN-ScAlN FBAR, where there are piezoelectric and ferroelectric layers with different piezoelectric properties, determining the electromechanical coupling for a certain mode within a complex structure remains challenging. Starting from the stress-charge form of the piezoelectric constitutional relations given in (1.1) and (1.2), a

generalized expression for the electromechanical coupling coefficient of *n* TE modes within such an FBAR has been computed in (4.5), based on modal analysis relating to mode shape and resonance and anti-resonance frequencies [69]-[71].

$$k_{t,n}^2 = \frac{\pi^2}{8}\left(\frac{\left\langle u_{,z}^{(n)} \middle| e/\epsilon \right\rangle^2}{\int (1/\epsilon)\, dz * \left\langle u_{,z}^{(n)} \middle| c u_{,z}^{(n)} \right\rangle}\right) \tag{4.5}$$

From (4.5), $\langle f(z)|g(z)\rangle = \int_\Omega f(z)g(z)dz$ define the inner product for real functions f and g across the entire domain of the FBAR from top and bottom free surfaces, Ω. The expression $u_{,z}^{(n)}$ is derived from (4.6):

$$u(z,t) = \sum_j a^j(t)\, u^{(j)}(z) \tag{4.6}$$

, which describes the displacement response for all modes and $a^j(t)$ are the modal amplitudes determined by the wave equation and the resonance and anti-resonance frequencies. The excitation from a time harmonic electric flux density is given by (4.7):

$$\rho(-\omega^2) \sum_j a^j(t)\, u^{(j)}(z) = T_{,z} \tag{4.7}$$

For a multilayer, multimode FBAR, (4.5) quantitatively analyzes the contribution of each layer to electric loading ($\int (1/\epsilon)\, dz$), mechanical loading ($\left\langle u_{,z}^{(n)} \middle| c u_{,z}^{(n)} \right\rangle$), and piezoelectric coupling in the complete structure. It shows that in order to efficiently excite a desired mode, mutual energy should be maximized by placing the zero strain crossings at the interfaces of the piezoelectric/ferroelectric. The expression verifies that within a polarization inverted ferroelectric layer, such as ScAlN, the effect of the inversion absorbs into the sign of the piezoelectric stress constant, and the film behaves like a negative piezoelectric layer [20].

4.4.Design and Simulation of Trilayer AlN-ScAlN FBAR

As shown in Fig. 4.4, the ScAlN film bulk acoustic wave resonator described in this work operates with three transduction layers (AlN–$Sc_{0.3}Al_{0.7}N$–AlN) placed between two electrodes. This allows for electric field control over the sign of piezoelectricity solely in the middle ferroelectric layer. The resonators are designed using a 1-D Mason Model [45] with a thin Sc_2O_3 layer underneath the bottom Mo electrode, where the first piezoelectric AlN layer and substrate thickness are designed for a half acoustic wavelength. The subsequent ScAlN and AlN layers thicknesses are set to ensure zero strain locations occur at the material interfaces. It has previously been reported that variation in ScAlN properties (piezoelectric coefficients d_{33} and d_{31}, dielectric constant, material stiffness) based on doping concentration can be modeled with good fitting based on Density-Functional Theory (DFT) [72]. The material parameters for the ScAlN and AlN layers in the Mason model are initially derived from [72], [73] as a baseline, then optimized and fitted to

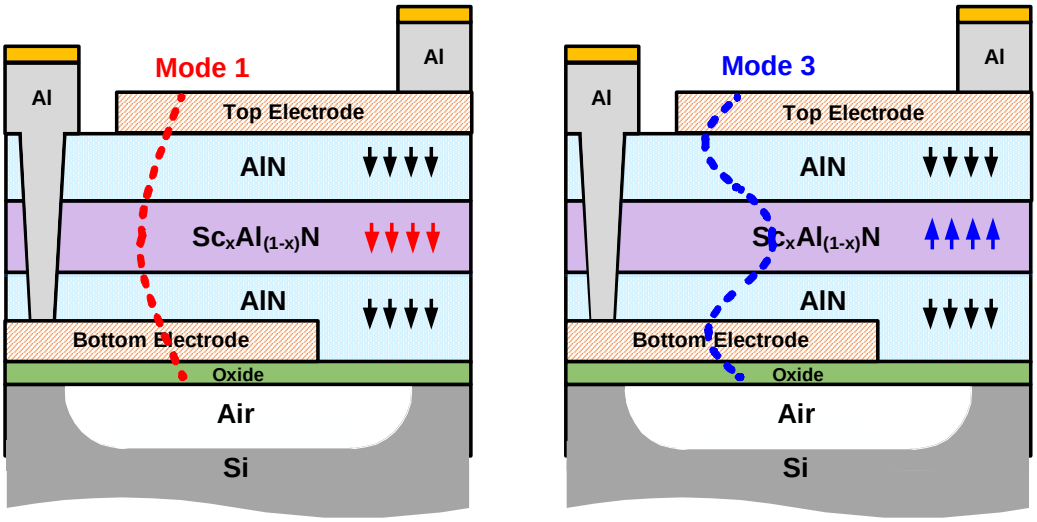

Fig. 4.4: Structure of the trilayer ferroelectric AlN-ScAlN-AlN FBAR in fundamental mode and higher order mode.

prior film measurements, and Table 4.1 lists the thicknesses of the resonator layers.

Table 4.1
Trilayer AlN/ScAlN/AlN finalized structure

Layer	Thicknesses (nm)
AlN1	95
ScAlN	85
AlN2	120

Through the application of low-frequency electric field bias on the electrodes, the ScAlN layer can switch polarization direction, selectively operating at different resonant modes. Fig. 4.5

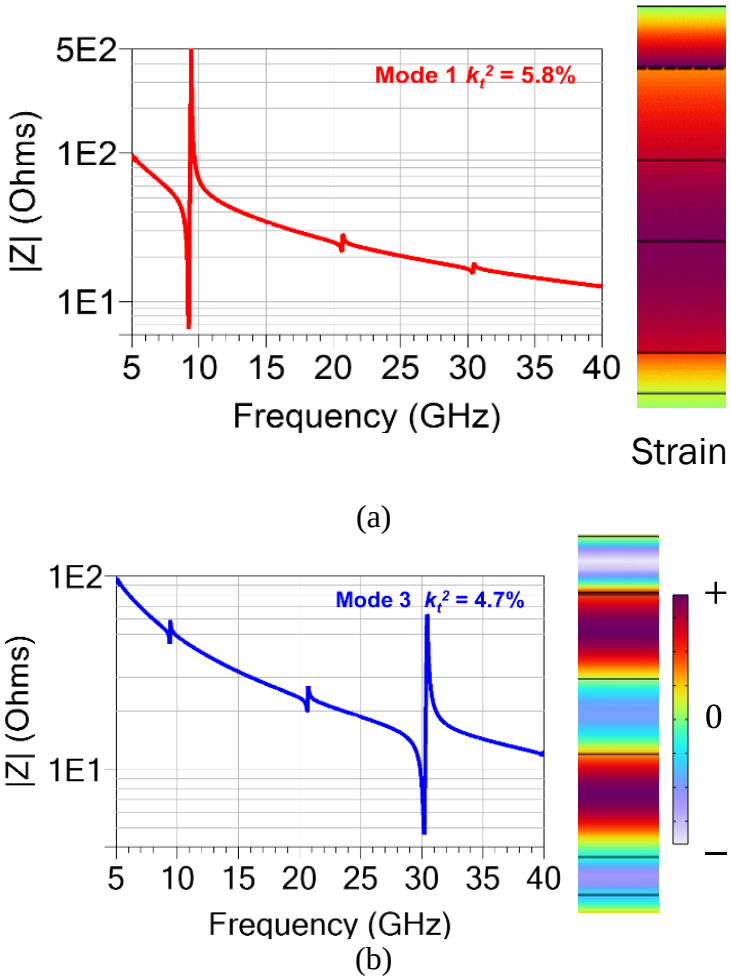

Fig. 4.5: Simulated Mode 1 and 3 for the trilayer AlN-ScAlN-AlN FBAR along with corresponding strain profiles extracted from COMSOL Multiphysics.

shows the simulated response of the trilayer resonator for the two polarization directions of the

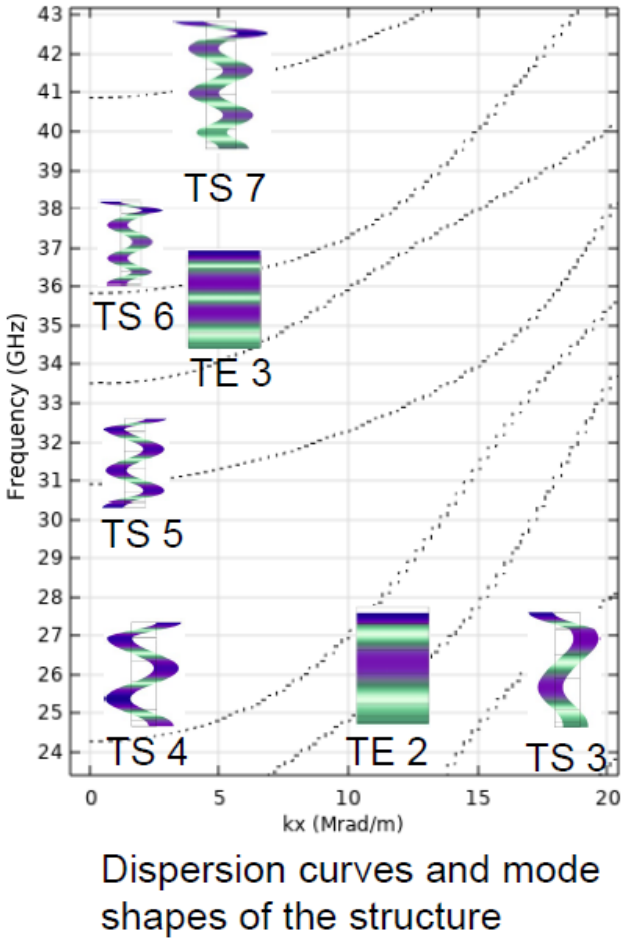

Fig. 4.6: Dispersion curves and their displacement mode shapes for the trilayer AlN-ScAlN-AlN FBAR.

ScAlN film. It should be noted that while operating in the higher order mode of the resonator, the fundamental mode is also suppressed, because the piezoelectric pattern is orthogonal to the strain profile of the mode.

As a higher order multilayer structure supports a number of additional lateral modes, the structure is also further analyzed in COMSOL Multiphysics in order to suppress the contribution of these undesired modes. Piezoelectric simulation where the columns of the structures are simulated assuming Floquet periodicity are conducted. Optimization of the thicknesses to achieve the dispersion curves shown in Fig. 4.6 is based on the findings from previous works [74]-[76].

4.5. Fabrication Process

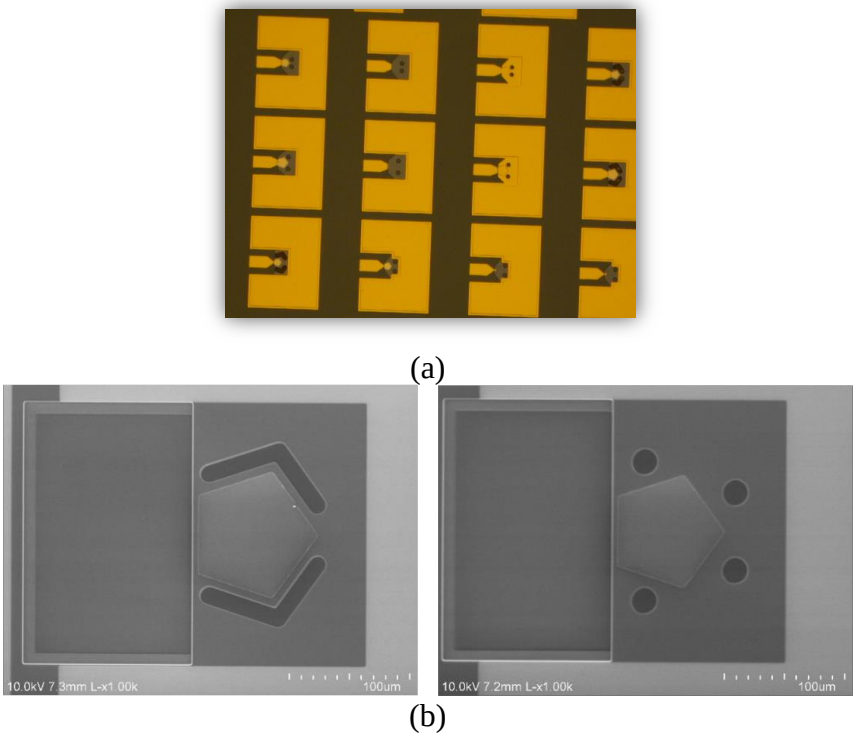

Fig. 4.7: (a) Layout and (b) scanning-electron microscopy (SEM) image of the AlN-ScAlN-AlN FBARs, where the defined released windows of the resonators must not expose Mo.

During the development of a ScAlN based FBAR fabrication process, one of the main challenges involve determining the etching technique to define the ground (GND) vias of the resonators, while not damaging surrounding ScAlN/AlN deposition that acted as a masking layer to prevent exposure of molybdenum during XeF_2 etching (Fig. 4.7). Moreover, the etching of ScAlN needs to be both timely and selective to the bottom Mo etch. While there are an extensive number of research works describing different etch techniques for AlN [77], it must be noted that highly doped ScAlN becomes more resistant to conventional reactive etch processes (dry etching: BCl_3, wet etching: TMAH/KOH based). Therefore, a process similar to ion beam etching described in [78] is utilized. Another associated challenge involves the stress buildup on multiple different layers of AlN and ScAlN growth on top of each other, due to differences in in-plane lattice

constants. In order to maintain wurtzite phase and a crack-free surface, growth conducted by collaborators in this work optimized molecular beam epitaxial (MBE) growth conditions, specifically substrate temperature. The fabrication process for the trilayer AlN-ScAlN-AlN FBAR is depicted in Fig. 4.8, starting with Mo/Sc_2O_3 layers on high resistivity Si substrate.

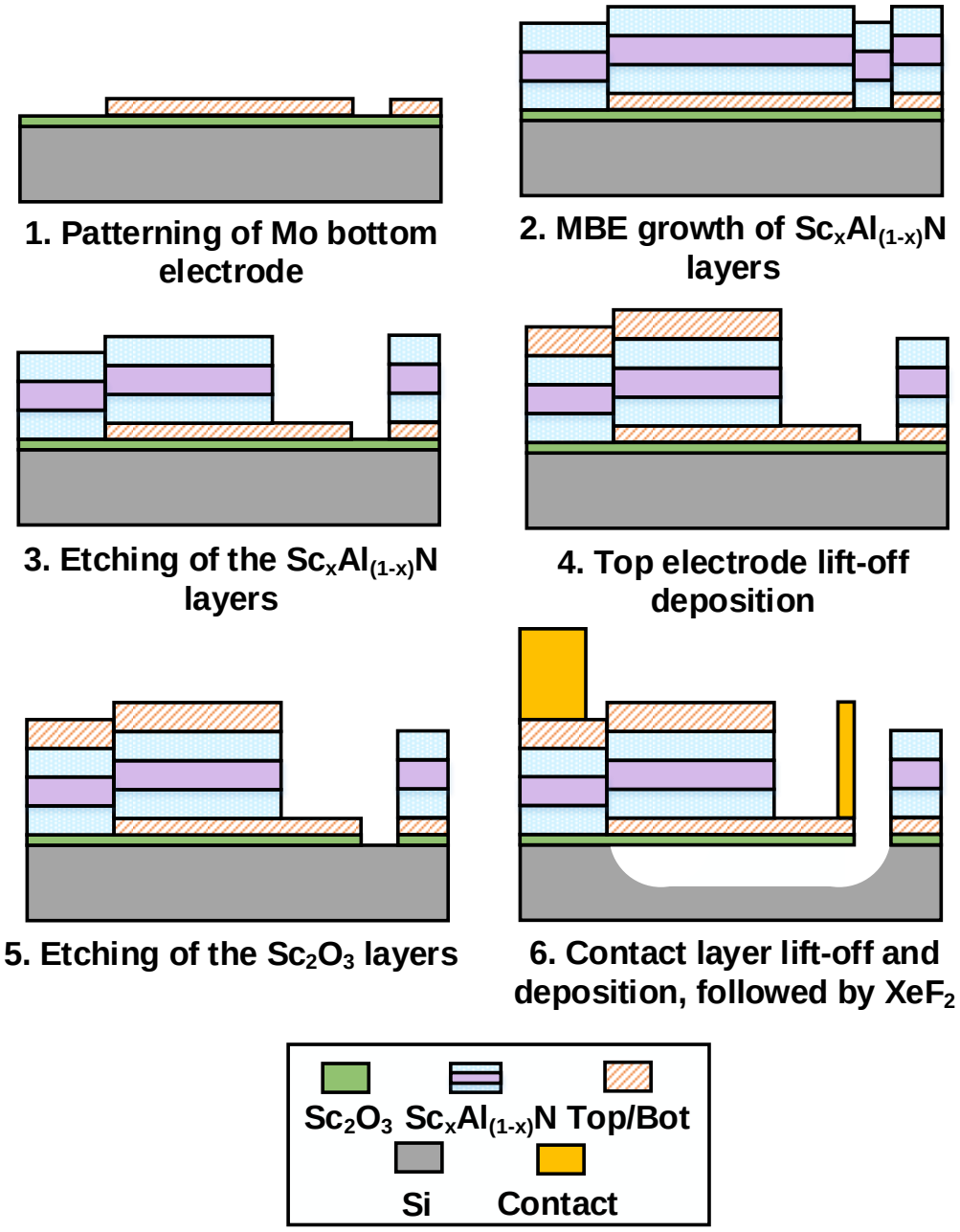

Fig. 4.8: The fabrication process for the trilayer ScAlN FBAR.

1) The bottom Mo layer is patterned using dry etching.

2) The piezoelectric-ferroelectric-piezoelectric layers are molecular beam epitaxially (MBE) grown in a Veeco Genxplor MBE system, where the grown $Sc_xAl_{(1-x)}N$ film had a composition ratio of x = 0.3. SEM image of the surface on patterned Mo substrate is shown

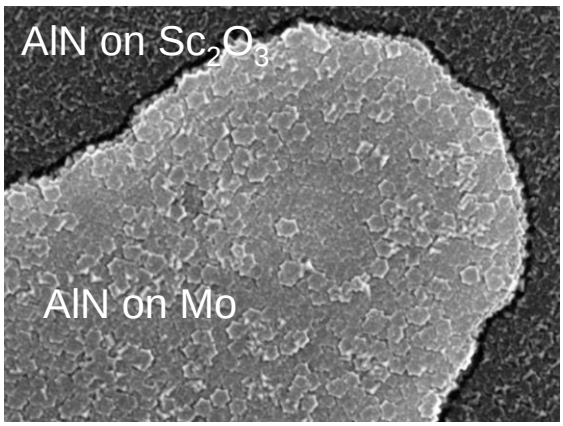

Fig. 4.9: SEM image of top AlN surface of the trilayer AlN-ScAlN-AlN structure, directly after growth.

in Fig. 4.9.

3) Following growth, the ScAlN and AlN layers are etched using a combination of timed ion milling and wet etching with AZ 726 developer solution in order to create the GND vias.

4) Subsequently, a thin layer of top electrode is deposited and patterned by evaporation and lift-off.

5) An additional timed ion milling using Ar is then conducted to etch through the Sc_2O_3 layers to create the release windows. All masking for the ion milling and wet etches use an SPR 220 (3.0) photoresist. Unlike ferroelectric BST FBARs, there is no NiChrome deposition for biasing lines.

6) Finally, a contact layer of Ti/Al/Ti/Au (20/600/5/100 nm) is patterned using evaporation and lift-off before the devices are fully released by etching the Si substrate in a 3.0 Torr XeF_2 environment.

4.6.Measurement Setup and Ferroelectric Switching in Trilayer Structure

The entire measurement setup for both the S-parameter response and polarization switching measurement is depicted in Fig. 4.10, along with a cross-sectional view of the device under test

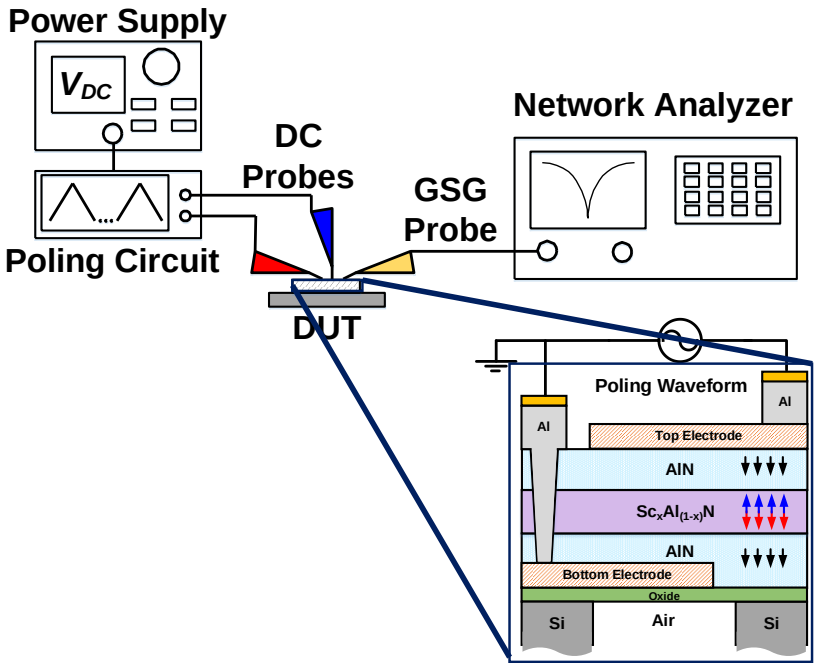

Fig. 4.10: The measurement and poling setup for the trilayer ScAlN FBAR.

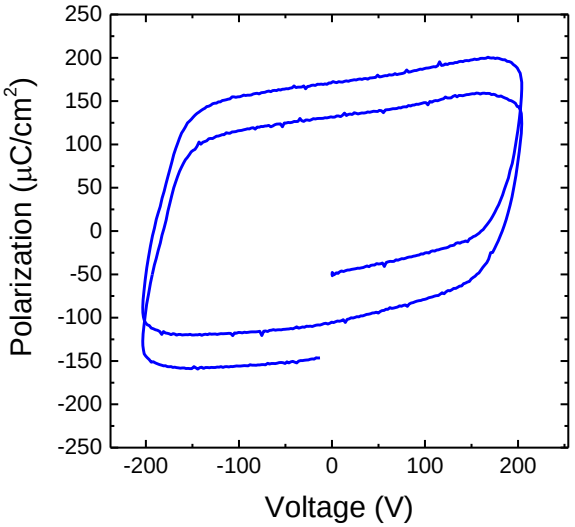

(a)

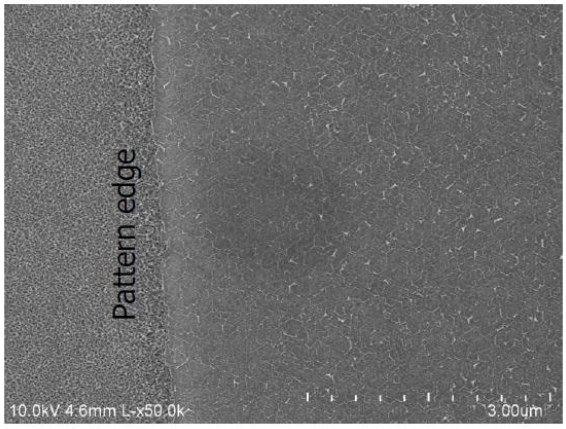

(b)

Fig. 4.11: Polarization-electric field loop for a trilayer AlN-ScAlN-AlN capacitor and (b) SEM image of the patterned edge for this sample.

(DUT). The fabricated ScAlN FBARs are measured using a PNA E8364C network analyzer connected to a Cascade Microtech probe station with 125 µm-pitch ground-signal-ground (GSG) probes. One port open-short-load calibration is conducted for a 50 Ω system impedance to shift the reference plane of the measurement to the tip of the probes. Additional on-wafer open and short structures on the same wafer are used to de-embed the effects of the on-waferpad and the associated parasitics. S-parameters measurements are taken and used to extract the impedance response in ADS. For polarization switching, the poling circuit and voltages are applied through two DC needle probes connected to top and bottom electrodes.

For the trilayer FBARs mentioned in this article, experiments have been conducted using a Radiant Multiferroic II Tester to verify ScAlN polarization switching. Polarization-electric field (PE) loops have been taken for unreleased FBARs on the same chip. Fig. 4.11 depicts the corresponding polarization of the trilayer devices, and the polarization and coercive voltages are similar to previously reported $Sc_xAl_{(1-x)}N$ films with remanent polarization values in the range of 130 µC/cm^2. Positive-Up-Negative-Down (PUND) measurements on unreleased trilayer ScAlN devices on the same chip have also been conducted and Fig. 4.12 shows the measured

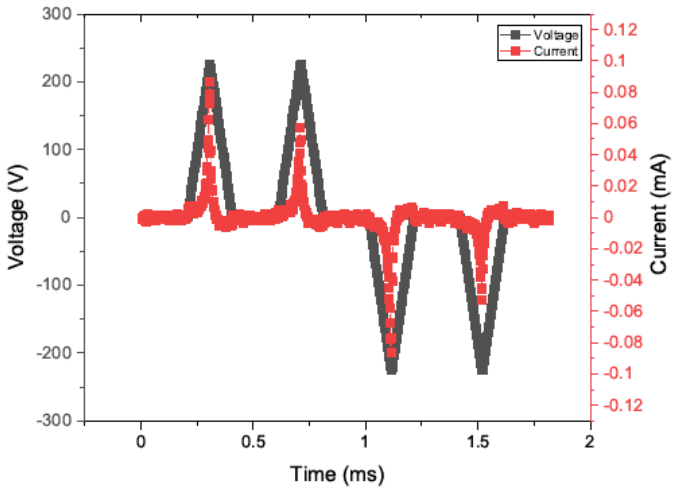

Fig. 4.12: Voltage and current waveform employed on a trilayer AlN-ScAlN-AlN capacitor. There is a noticeable drop in the second pulses for each polarity, indicating switching versus leakage current.

instantaneous current for the applied voltage pulses, where triangular pulses with pulse widths of 150 μs are applied.

One previous method that has been applied to verify complete ferroelectric ScAlN

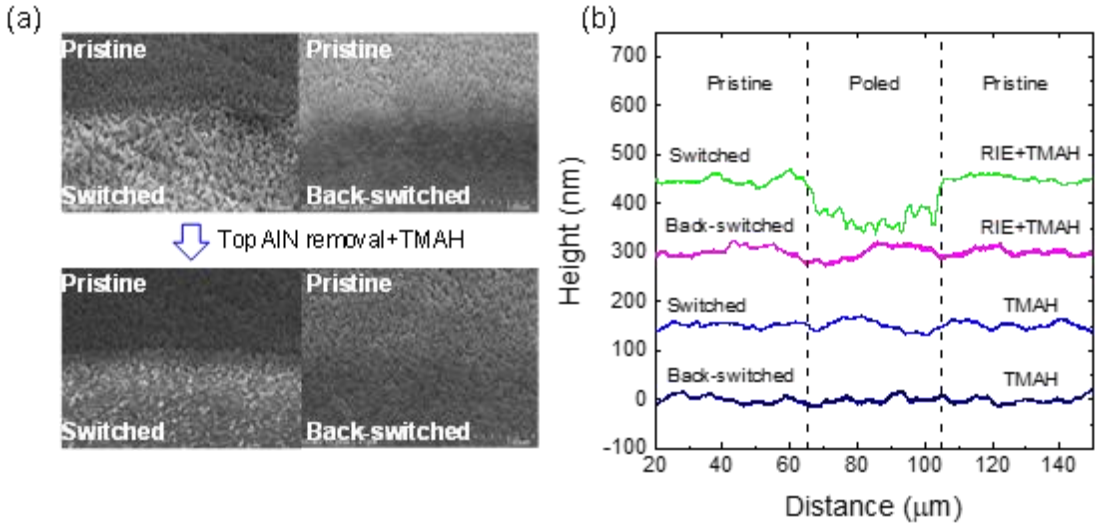

Fig. 4.13: Polarity-sensitive etching results of the trilayer study. (a) SEM images and (b) height profiles of the trilayer structure subject to TMAH etching before and after removing the top AlN layer. Switched regions were only etched by TMAH after top AlN removal, indicating that only the ScAlN layer was switched. Reproduced from [80].

switching between metal (M-) and nitrogen (N-) polar states involves wet etching in either acid (H_3PO_4) or base solutions (potassium hydroxide, KOH, and tetramethylammonium hydroxide, TMAH) [17]. As the etching rate of ScAlN film is highly dependent on the polarity of the film, experimental results utilizing this etch technique verifies poling of the ScAlN even in a trilayer (AlNScAlN-AlN) structure, as described herein [80]. Fig. 4.13 describes the wet etchant selectivity of ScAlN, dependent on the its polarity with TMAH based etching. The experiment also verifies that solely the ScAlN layer poles and there is no noticeable ferroelectric behavior of AlN [81]. While a good indicator of switching, material etch tests are destructive to the device; therefore, an alternative method is required for the trilayer FBARs. A PUND electric field excitation and measurement on the film is another well-known, popularized method to validate ferroelectric film switching, as described in multiple ScAlN research articles [79], [80], [82]. The process involves sending to two similar polarity pulses to 1) differentiate between the switching and leakage current and 2) determine the polarization of the film.

As the released trilayer ScAlN devices (i.e. FBARs) are more fragile, the ferroelectric switching waveform requires fine tuning based on a number of failure mechanisms that were observed during poling, including joules heating, mechanical deformation, and breakdown. Previous work demonstrated that ScAlN film are able to gradually invert polarization through a number of pulses at reduced voltages [79]. To the best of the author's knowledge, there is few or no reported literature that discusses *complete* ferroelectric switching of ScAlN using multiple cycles of voltage pulses at levels lower than the required coercive field. To verify complete trilayer ScAlN switching on resonators, an alternative process is utilized as depicted in Fig. 4.14, where during the negative cycle of the switching waveform is adjusted to lower voltage, greater number of cycles pulses than standard PUND measurements. These measurements are conducted on a

trilayer unreleased device (i.e. capacitor) that is capable of handling higher voltages compared to resonator. To verify complete switching with a longer pulse train, another PU cycle is conducted following the negative pulse train. From this, the remanent polarization on unreleased trilayer ScAlN devices obtain from a modified waveform with greater number of negative triangular pulses at lower voltages matches closely with the remanent polarization obtained from a higher voltage PUND measurement, which verifies complete ScAlN switching. The extracted remanent polarization for modified waveform on the device is around the same range of approximately **130 µC/cm²**. Slight variations between the two polarizations are attributed to traps from the film.

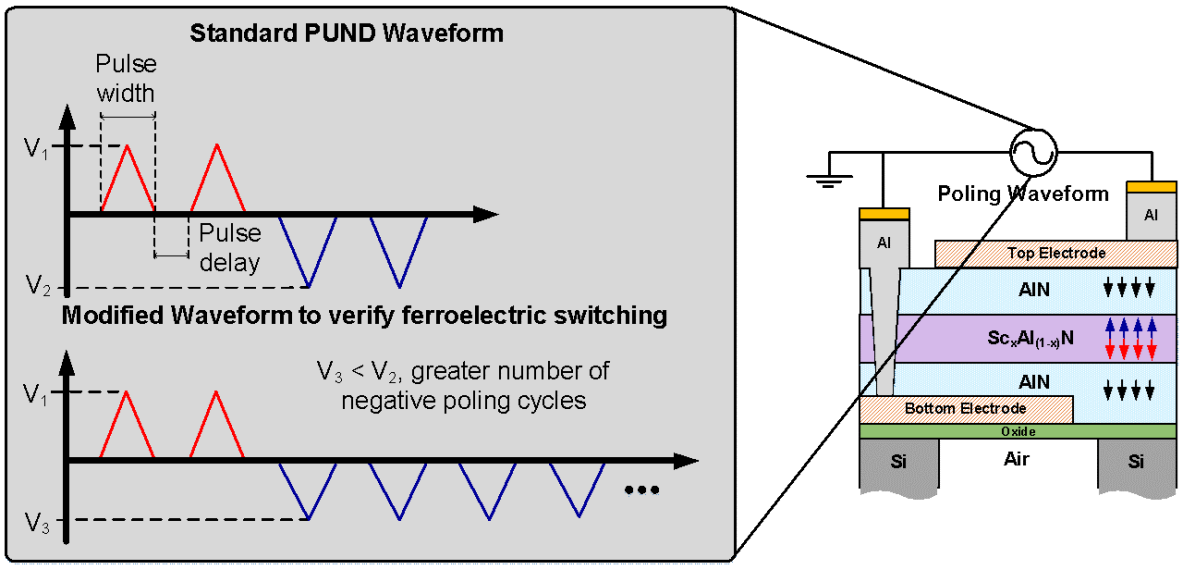

Fig. 4.14: Polarization switching procedure employed for trilayer FBARs, which utilized a number of reduced triangular pulses.

4.7.Experimental Results and Discussion

Aside from remanent polarization and wet etch confirmation of ScAlN polarization switching, another test for the trilayer FBAR structure involves the disappearance of the

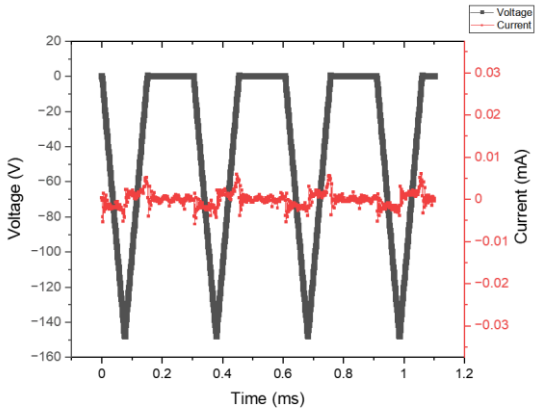

Fig. 4.15: Voltage and current waveform employed on a trilayer AlN-ScAlN-AlN FBAR with no transient current spike.

fundamental mode as the ScAlN film changes polarity. After release, the fabricated trilayer AlN/ScAlN/AlN resonators on Mo are also poled using the same ferroelectric tester and two DC needle probes. Similar waveform discussed in the previous section (150 µs, reduced voltages of 150 V) triangular waves are used. Fig. 4.15 depicts the current and voltage response from PUND measurement for the trilayer resonators, but as the resonators are gradually poled, there is no distinct transient current spike. Frequency response of the trilayer FBAR from its pristine,

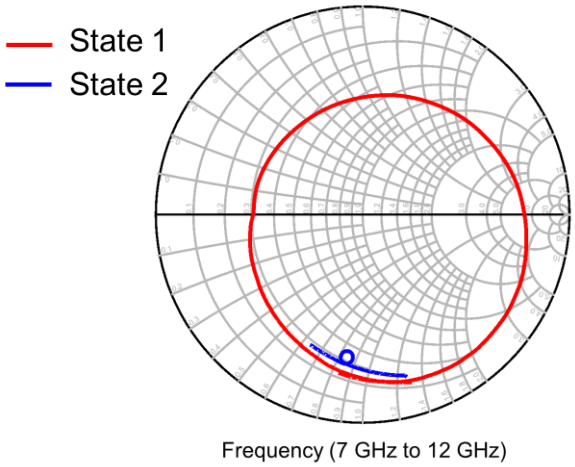

Fig. 4.16: Disappearance of the fundamental mode of the trilayer FBAR as the ScAlN switches polarization.

untouched state directly after release to states after a number of poling waveform cycle is applied have been measured. From Fig. 4.16, it is evident that the original fundamental mode of the resonator gradually disappears, although not completely, but to a low k_t^2 (<0.5%). Simultaneous to the disappearance of the fundamental mode, a higher order mode becomes excited with greater magnitude.

Fig. 4.17 and Fig. 4.18 denote the trilayer response for fundamental and higher order mode for two iterations of trilayer AlN-ScAlN-AlN FBAR, where the second iteration improves upon optimized material parameters, device design, and thicknesses of the structure. For the second iteration, A fitted mBVD model is provided for both modes in Table 4.2. The second trilayer FBAR

Table 4.2
mBVD model parameters

Parameter	Mode 1 (P)	Mode 3 (S)
C_e (pF)	0.341	0.373
C_m (pF)	0.020	0.011
L_m (nH)	12.95	2.41
R_m (Ω)	3.113	6.682
Q_m	264	82

occupies an active area of approximately 1024 μm^2, where the fundamental mode is measured

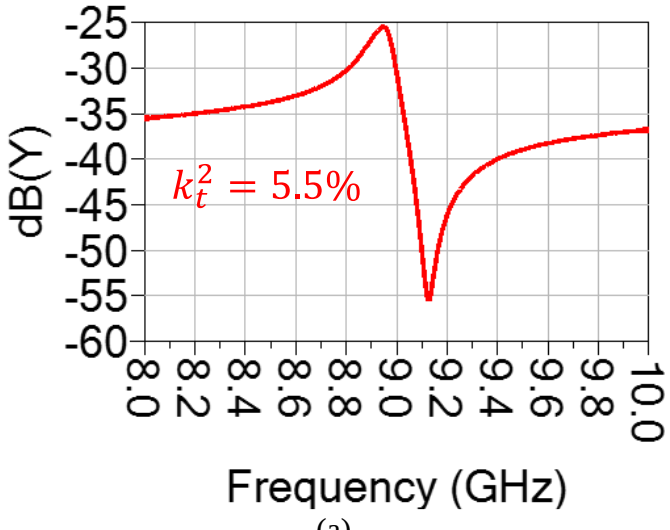

(a)

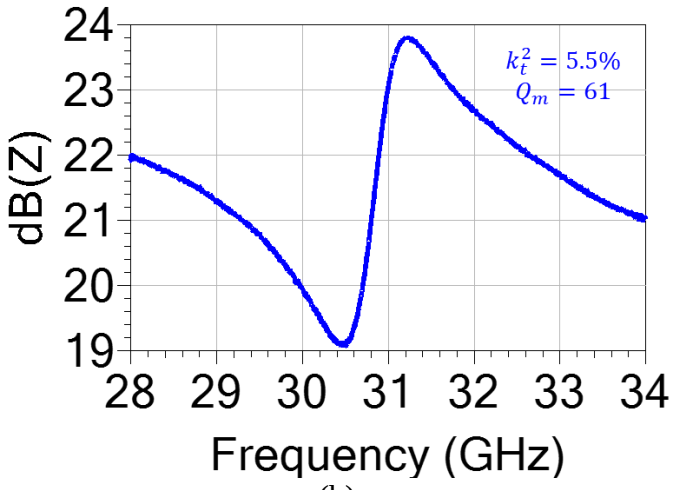

(b)

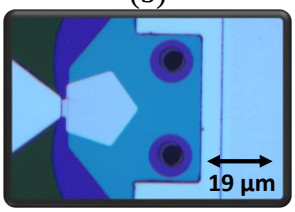

(c)

Fig. 4.17: Measured (a) fundamental and (b) third mode response of the first iteration trilayer FBAR along with (c) optical photograph of the device.

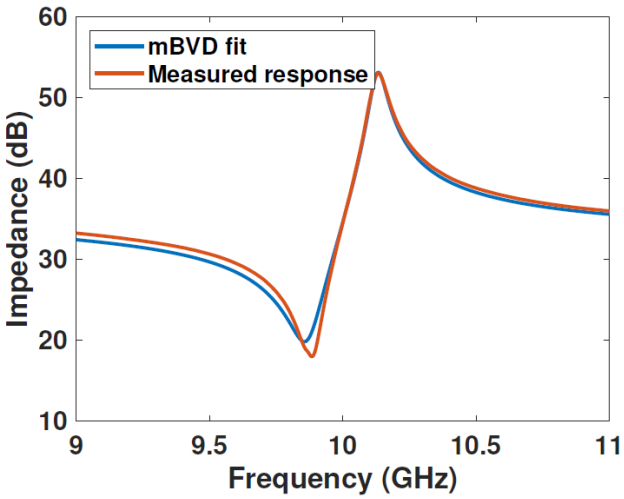

(a)

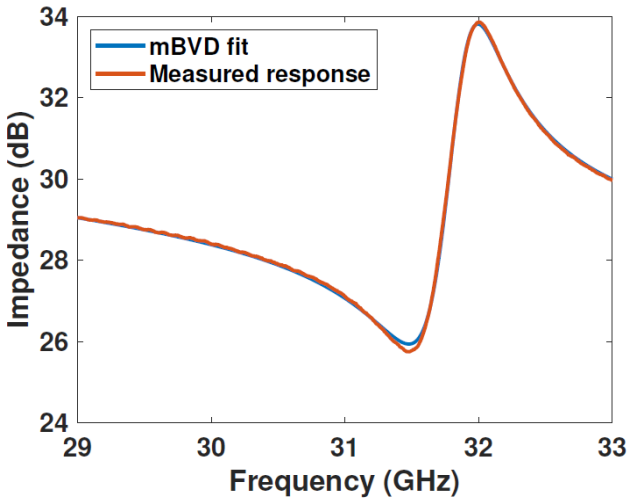

(b)

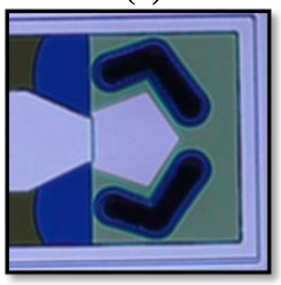

(c)

Fig. 4.18: Measured (a) fundamental and (b) third mode response of the trilayer FBAR along with (c) optical photograph of the device.

directly after release. The fundamental mode for the trilayer AlN-ScAlN-AlN FBAR, as depicted in Fig. 4.17 (a), resonates at 9.9 GHz with a k_t^2 of 5.8%. After poling through multiple cycles, the same device displayed a measured third mode response shown in Fig. 4.17 (b) with a k_t^2 of 4.7% at 31.4 GHz. The polarization of the ScAlN is maintained for a period of over five months. To the best of the author's knowledge at the time, this is comparable coupling factor among AlN and ScAlN based BAW resonators at the mm-Wave regime; moreover, the work conducted herein is the first demonstrated performance of a switched ScAlN layer, sandwiched between AlN films, in order to achieve a higher order mode FBAR. Fig. 4.19 offers a comparison to state-of-the-art AlN and ScAlN based BAW resonators, where Table 4.3 summarizes the results for resonators above 24 GHz.

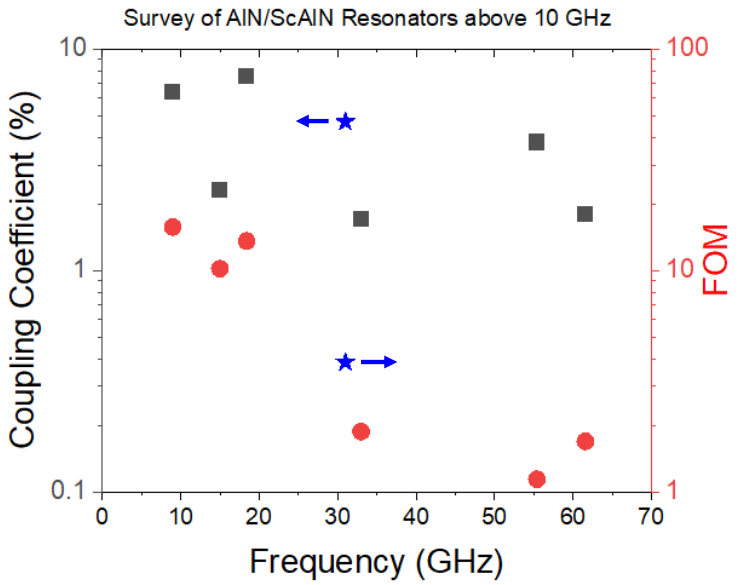

Fig. 4.19: k_t^2 and FOM for ScAlN/AlN BAW Resonators.

Table 4.3
Figure of Merit ($Q_m \bullet k_t^2$) of AlN/ScAlN BAW resonators in mm-Wave regime

Work	***f* (GHz)**	Q_m	k_t^2 **(%)**
This	31	82	4.7
[83]	55.4	30	3.8
[84]	55	90	2.2
[85]	33	110	1.7

The designed trilayer resonator has comparable performance to other AlN/ScAlN resonators. The datapoints shown in figure 4.18 to the left of the reported trilayer with greater coupling utilized multiple layers of solely ScAlN, where poling is conducted during each ScAlN layer growth, complicating the fabrication process. A similar increase in coupling for the presented trilayer can be achieved by slightly doping the AlN layers; however, more investigation into residual stress of the multilayer structure, growth conditions, etc. are required.

4.8. Conclusion

Modern wireless communication systems are increasingly complex with greater functionality and imposes new challenges on the RF front end design. One of the major challenges involves filtering beyond the sub-6 GHz regime with increased FBW. Within this chapter, new BAW resonators that are capable of overcoming fundamental frequency scaling limitations, specifically thickness, lateral area, and k_t^2, are presented. Based on composite alternating layers of AlN and ScAlN, a multilayer FBAR that can switch between a fundamental to a higher order mode is presented. Trilayer FBARs (AlN-ScAlN-AlN) are designed, fabricated, and measured, where polarization switching of the middle ScAlN is achieved through applied voltages on two electrodes (bottom Mo and top Al). The electromechanical coupling coefficient for multilayer structure are calculated based on modal analysis, and structural analysis of the trilayer is presented based on COMSOL Multiphysics simulation. Measurement results of the resonator demonstrate that the device is capable of operating in two different states either at 9.9 GHz or 31.4 GHz with k_t^2 values exceeding 4% in both states. Complete polarization switching of the ScAlN within trilayer resonator has been validated based on comparison between a conventional PUND measurement and a modified waveform with reduced voltages, but greater number of cycles.

The presented switchable BAW resonator remains attractive for applications in the mm-Wave regime, due to its capability to maintain electromechanical coupling at higher order modes. The trilayer ScAlN resonator has fabrication requirements that are compatible to currently employed commercial BAW device technologies (two metal electrode deposition along with patterning and one etch for the entire transducer film). Further improvement of the ScAlN growth conditions for better ScAlN crystallinity and domain orientation would significantly enhance the proposed structures' figure of merit (FOM). With optimization of the material parameters of the

transduction layers, overmoded FBARs with high k_t^2 that can satisfy FBW and coupling requirements for new 5G standards in the mm-Wave regime can be realized.

Chapter 5

Conclusion and Future Work

5.1.Summary of contribution

The work presented in this thesis focuses on development of RF acoustic resonator and filters for next generation RF front-ends in wireless communication systems through the use of ferroelectric materials. Ferroelectrics as a class of multifunctional materials exhibit several desirable characteristics that can be employed for the design of intrinsically switchable and tunable filters. Two different ferroelectric materials are studied within this work, barium strontium titanate and scandium aluminum nitride. The main property exploited for the first material BST is its large electrostriction coefficient, otherwise referred to as the electric field induced piezoelectricity, in order to switch on or off BST thin film bulk acoustic wave resonators.

The switchable BST FBARs serve as the building block for intrinsically reconfigurable RF filters. The integration of both filtering and switching functionality onto a single device offers a key advantage to other competing technologies, as it reduces the complexity, loss in the RF signal path, and cost of the RF front-end. In Chapter 2, a quad band BST filter bank employing a manifold configuration is designed, fabricated, and characterized. Design approach

involve mBVD and Mason modeling to represent the resonators used in the ladder type filters, where transitioning between different bands occurred solely through DC electric field across the BST FBARs. In Chapter 3, work is presented on the design, fabrication, and realization of hybrid BST based reconfigurable circuits directly on a silicon chip. These circuits employ the electrostrictive properties of thin film BST within an acoustic resonator structure in order to adjust their filter transfer function. The design methodology is based on microwave all-pass network synthesis. For the first time, RF filters with unique reconfigurable transfer function characteristics (all-pass-to-bandstop response and bandpass-to-all-reject response) are presented at operational frequencies as high as 2 GHz.

For the second material, ScAlN, the effective 'negative' piezoelectricity has been utilized in the design of multilayer FBARs that are scalable to the mm-Wave regime. For the first time, a polarity controlled trilayer FBAR with 3rd mode operation is demonstrated in Chapter 4. Design approach for the structure is based on modal analysis of electromechanical coupling in the structure. The measured FBAR maintains fabrication complexity similar to single layer BAW resonators, where only top and bottom electrodes are required for polarization inversion and RF excitation. Unlike BST, there is no sustained DC bias voltage requirement, as the polarization state of ScAlN will hold depending on the biasing history. The design provides a method to scale FBARs to higher frequency limits, beyond the sub-6 GHz regime, while maintaining total piezoelectric and electrode thicknesses comparable to their lower frequency counterparts.

5.2.Future Direction

5.2.1. Multimode Ferroelectric based FBARs

Within this thesis, a dual mode multilayer AlN-ScAlN-AlN FBAR has been investigated. Towards the development of multimode filters with increased number of reconfigurable states, an alternative FBAR structure is shown in Fig. 5.1. The multilayer BAW resonator consists of several layers of ferroelectrics sandwiched between thin intermediate electrode layers. In such a structure, thin interlayer electrodes (thicknesses much less than the top and bottom conductors) serve to set up a DC electric field within the corresponding transduction layer, thereby controlling their

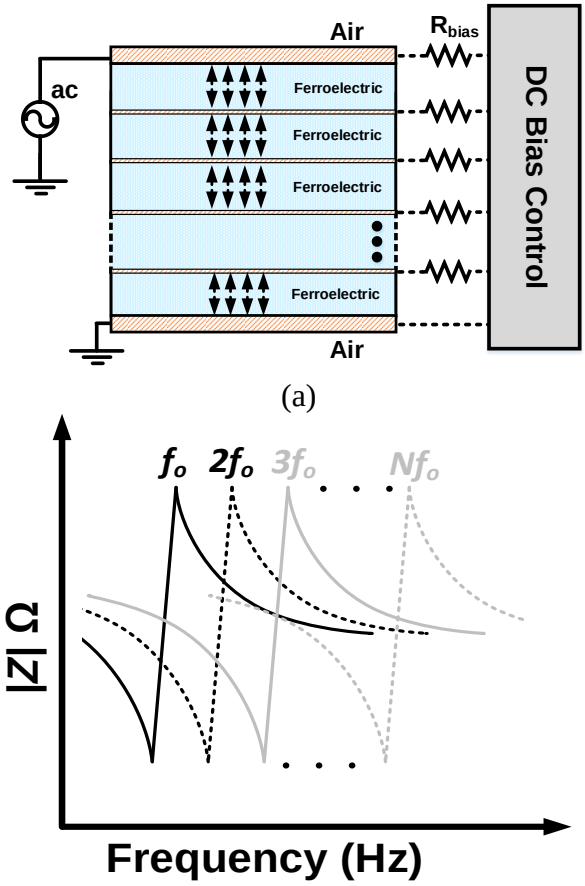

Fig. 5.1: (a) Ferroelectric mode-switchable multilayer resonator structure supporting n modes. Conceptualized frequency response is depicted in (b).

effective piezoelectric coefficient (+/-). The device is capable of resonating up to N different modes, selectable based on the electrically controlled piezoelectric coefficients across the ferroelectric layers. Through application of appropriate DC biasing, any of these desired resonator

modes can be selected by generating an appropriate pattern of effective piezoelectric coefficients that matches to the stress profile of the desired mode. For the resonator with intermediate electrodes, a fabrication process requires development to 1) deposit high quality ferroelectric *in situ* with metal electrodes and 2) appropriate pattern intermediate electrodes to avoid layout associated parasitics that degrade mode excitation.

As a preliminary example, COMSOL Multiphysics simulations have been performed for the FBAR structure. Fig. 5.2 depicts the structure and simulation results for an eight-layer ScAlN FBAR that allows for optimal excitation of mode 1, 2, 4, and 8 based on the piezoelectric profile

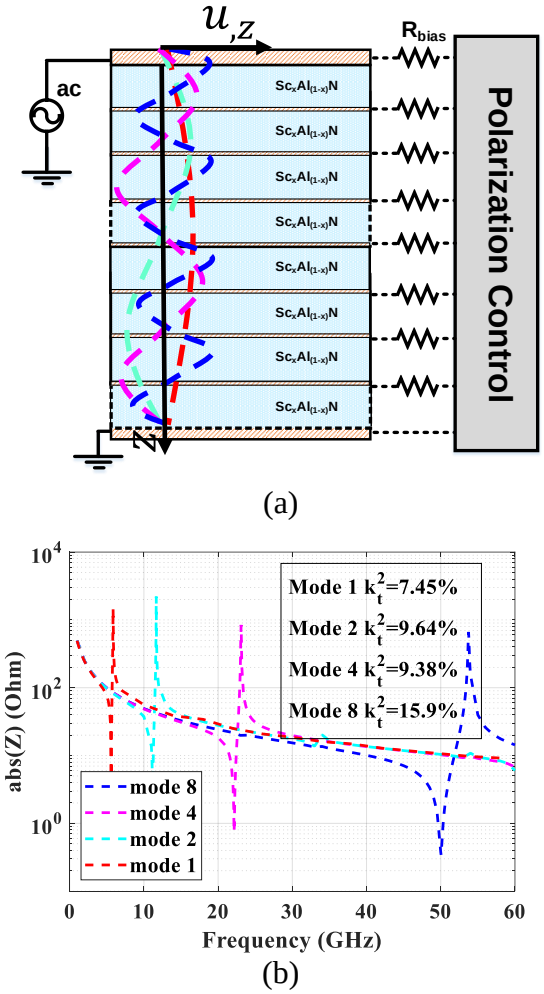

Fig. 5.2: (a) Eight-layer ScAlN FBAR structure and mode shapes with (b) simulated frequency response in COMSOL.

of the structure. Thicknesses of 30% doped ScAlN are set to 70 nm thick, aside from the top and bottom layers set at 50 nm each with Al electrodes. Variation in the electromechanical coupling across the four modes occur due to the contribution of intermediate electrodes to the high strain energy. As discussed in chapter 4, this degrades the k_t^2 more prominently in the lower ordered modes.

5.2.2. Multilayer and Mode-Switchable Ferroelectric based FBAR Filters and Filter Banks

The RF front-end of modern wireless communication systems must support a large number of frequency bands and wireless standards while providing interference immunity within a crowded electromagnetic environment. It has been pointed out that frequency agile RF filters are required for the development of reconfigurable radios, where a communication system can flexibly select the optimum band and protocol based on the real-time electromagnetics environment, fading, channel conditions, and link budget. Utilizing the intermediate electrode, N-mode resonators from the previous section, design electronically controlled multimode filters and filter banks can be realized. By incorporating a number of multimode ferroelectric filters in parallel, filter banks can be designed that allow for seamless transition between single or multiband simultaneous operation without the use of switchplexers. Each of the filters within the filter bank provide switchable multiband operation based on the selection of one of several resonant frequencies within the multimode resonators described earlier. The added functionality provided by multimode resonators allows for extremely compact filters operating across a wide frequency range without introducing additional hardware complexity.

Considering the limited available circuit real estate to support an increasing number of bands, there is a continuous trend towards current RF front-end miniaturization and approaches to

simplify their architecture. More stringent requirements, such as power handling, minimal loading effect, low levels of cross-isolation, and nonlinear mixing products (IMDx), mandate proper design of the matching networks between different filter paths on the RF front-end.

As a preliminary example of a multimode FBAR filter performance, Fig. 5.3 shows the response of a BST-based quad mode 2.5 stage filter, capable of switching between four different frequency bands. By biasing all the resonators within the filter to select a particular resonance mode, the filter will exhibit a corresponding bandpass response at the desired band. The resonators here are simulated based on material parameters of BST (Q = 400, K_t^2 = 10%), along with the

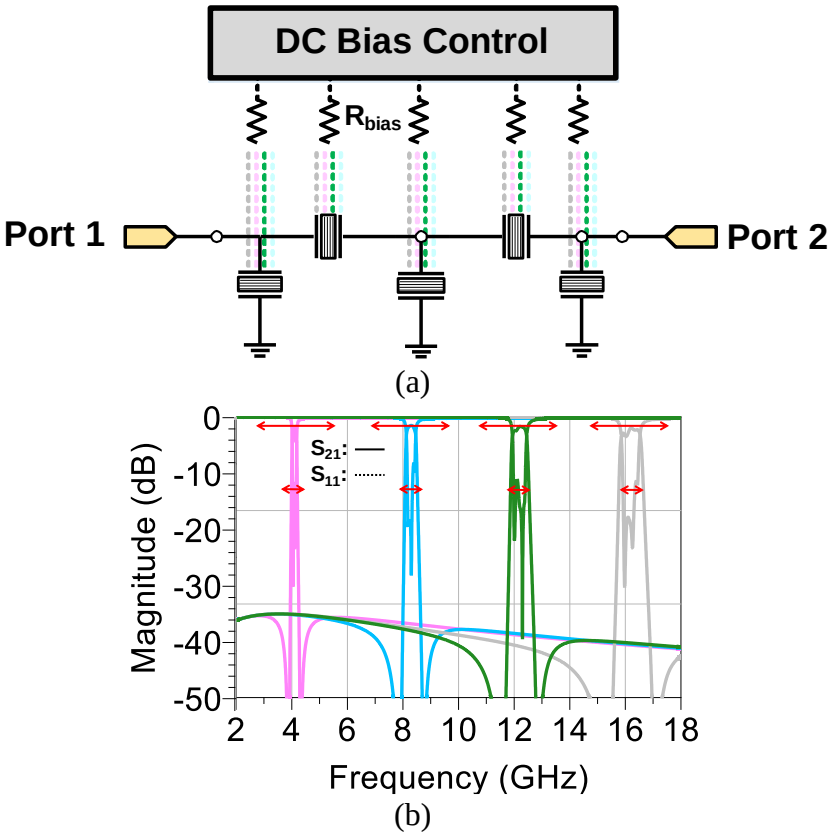

Fig. 5.3: (a) Circuit schematic and (b) simulation response of the multimode resonators, which can provide one of the four bandpass filters (all bands provide approximately 5% FBW) based on the selection of biasing voltages. Simulation conducted with a stackup of four (N) BST layers with five (N+1) electrodes to support the biasing setup for each transduction layer.

properties of the electrodes and other supporting layers. The next step for this future work is to fabricate fully integrated ferroelectric-based filter banks with these multimode filters.

References

[1] Ericsson, “Ericsson Mobility Report November 2023,” 2023. [Online]. Available: https://www.ericsson.com/en/reports-and-papers/mobility-report/

[2] Accton, “The Emergence of 5G mmWave,” 2022. [Online]. Available: https://www.accton.com/Technology-Brief/the-emergence-of-5g-mmwave/#:~:text=Although%20the%20mmWave%20bands%20extend,together%20for%20higher%20data%20throughput.

[3] S. Mahon,” The 5G Effect on RF Filter Technologies”, CS Mantech conference, May 23, 2017, Indian Wells, CA.

[4] S. Gong, R. Lu, Y. Yang, L. Gao and A. E. Hassanien, "Microwave Acoustic Devices: Recent Advances and Outlook," *IEEE Journal of Microwaves*, vol. 1, no. 2, pp. 601-609, Spring 2021.

[5] M. Schaefer, R. Rothemund and G. Fattinger, "Process and Design Challenge for SMR-type Bulk Acoustic Wave (BAW) Filters at Frequencies Above 5 GHz,"2019 IEEE International Ultrasonics Symposium (IUS), 2019, pp. 1696-1699.

[6] R. Ruby, “A snapshot in time: The future in filters for cell phones,” IEEE Microw. Mag., vol. 16, no. 7, pp. 46–59, Aug. 2015.

[7] K. Hashimoto, *RF Bulk Acoustic Wave Filters for Communications*. Boston, MA, USA: Artech House, 2009.

[8] N. Setter, D. Damjanovic, L. Eng, G. Fox, S. Gevorgian, S. Hong, et al., "Ferroelectric thin films: Review of materials, properties, and applications," *Journal of Applied Physics*, vol. 100, pp. 051606-051606-46, 2006.

[9] R. A. York, “4 Tunable Dielectrics for RF Circuits,” Scitech Publishing, 2009.

[10] H. Budzier and G. Gerlach, *Thermal infrared sensors: theory, optimisation and practice:* Wiley. com, 2010.

[11] Franco Jona and G. Shirane, “Ferroelectric Crystals”, *International Series of Monographs on Solid State Physics*, Pergamon Press 1962.

[12] Thakre A, Kumar A, Song HC, Jeong DY, Ryu J. Pyroelectric Energy Conversion and Its Applications-Flexible Energy Harvesters and Sensors. Sensors (Basel). 2019 May 10;19(9):2170.

[13] N. Setter, D. Damjanovic, L. Eng, G. Fox, S. Gevorgian, S. Hong, et al., "Ferroelectric thin films: Review of materials, properties, and applications," *Journal of Applied Physics*, vol. 100, pp. 051606-051606-46, 2006.

[14] N. K. Pervez, P. J. Hansen, and R. A. York, “High tunability barium strontium titanate thin films for rf circuit applications,” in Applied Physics Letters, Nov. 2004, vol. 85, no. 19, pp. 4451–4453.
[15] A. Tombak et al., “Tunable barium strontium titanate thin film capacitors for RF and microwave applications,” IEEE Microw. Wirel. Components Lett., vol. 12, no. 1, pp. 3–5, Jan. 2002.
[16] D.-Y. Chen and J. D. Phillips, "Electric field dependence of piezoelectric coefficient in ferroelectric thin films," Journal of electroceramics, vol. 17, pp. 613-617, 2006.
[17] S. Fichtner, N. Wolff, F. Lofink, L. Kienle, and B. Wagner, “AlScN: A III-V semiconductor based ferroelectric,” Journal of Applied Physics, vol. 125, no. 11, p. 114103, 03 2019.
[18] Akiyama, M., Kamohara, T., Kano, K., Teshigahara, A., Takeuchi, Y. and Kawahara, N. (2009), Enhancement of Piezoelectric Response in Scandium Aluminum Nitride Alloy Thin Films Prepared by Dual Reactive Cosputtering. Adv. Mater., 21: 593-596.
[19] R. Aigner, G. Fattinger, M. Schaefer, K. Karnati, R. Rothemund and F. Dumont, "BAW Filters for 5G Bands," 2018 IEEE International Electron Devices Meeting (IEDM), San Francisco, CA, USA, 2018, pp. 14.5.1-14.5.4.
[20] M. Z. Koohi and A. Mortazawi, "Negative Piezoelectric-Based Electric-Field-Actuated Mode-Switchable Multilayer Ferroelectric FBARs for Selective Control of Harmonic Resonances Without Degrading $Keff^2$," in IEEE Transactions on Ultrasonics, Ferroelectrics, and Frequency Control, vol. 67, no. 9, pp. 1922-1930, Sept. 2020.
[21] P. Warder and A. Link, "Golden Age for Filter Design: Innovative and Proven Approaches for Acoustic Filter, Duplexer, and Multiplexer Design," in IEEE Microwave Magazine, vol. 16, no. 7, pp. 60-72, Aug. 2015, doi: 10.1109/MMM.2015.2431236.
[22] X. Zhu, J. D. Phillips, and A. Mortazawi, "A DC voltage dependant switchable thin film bulk wave acoustic resonator using ferroelectric thin film," in IEEE MTT-S Int. Microw. Symp. Dig., Jun. 2007, pp. 671-674.
[23] S. Sis, S. Lee, V. Lee, A. Bayraktaroglu, J. Phillips, and A. Mortazawi, “Intrinsically switchable, high-Q ferroelectricon-silicon composite film bulk acoustic resonators,” *IEEE Trans. Ultrason. Ferroelectr. Freq. Control*, vol. 61, no. 2, pp. 231–238, 2014.
[24] S. A. Sis, “Ferroelectric-on-Silicon Switchable Bulk Acoustic Wave Resonators and Filters for RF Applications,” 2014.
[25] V. Lee, S. A. Sis, J. D. Phillips, and A. Mortazawi, “Intrinsically switchable ferroelectric contour mode resonators,” *IEEE Trans. Microw. Theory Tech.*, vol. 61, no. 8, pp. 2806–2813, 2013.
[26] V. C. Lee, “Switchable and Tunable Ferroelectric Devices for Adaptive and Reconfigurable RF Circuits,” University of Michigan, 2014.
[27] S. Lee, “Design and Modeling of Ferroelectric BST FBARs for Switchable RF Bulk Acoustic Wave Filters”, PhD dissertation, the University of Michigan, 2016.
[28] S. Lee, M. Zolfagharloo Koohi, S. A. Sis, V. Lee, and A. Mortazawi, “Temperature dependent characteristics of intrinsically switchable ferroelectric composite FBARs,” Jul. 2015.

[29] M. Z. Koohi, S. Lee, and A. Mortazawi, “High Qm×K2t intrinsically switchable BST thin film bulk acoustic resonators,” in *IEEE MTT-S International Microwave Symposium Digest*, Oct. 2017, pp. 296–299.

[30] M. Z. Koohi, S. Nam, and A. Mortazawi, “Linearity Measurements of Intrinsically Switchable BST FBAR Filters,” in *2018 48th European Microwave Conference, EuMC 2018*, Nov. 2018, pp. 830–832.

[31] J. Berge, A. Vorobiev, W. Steichen, and S. Gevorgian, “Tunable solidly mounted thin film bulk acoustic resonators based on Ba xSr1-xTiO3 films,” *IEEE Microw.Wirel. Components Lett.*, vol. 17, no. 9, pp. 655–657, Sep. 2007.

[32] A. Vorobiev, S. Gevorgian, M. Löffler, and E. Olsson, “Correlations between microstructure and Q-factor of tunable thin film bulk acoustic wave resonators,” in *Journal of Applied Physics*, Sep. 2011, vol. 110, no. 5, p. 054102.

[33] S. Gevorgian, *Ferroelectrics in Microwave Devices, Circuits and Systems: Physics, Modeling, Fabrication and Measurements*. New York, NY, USA: Springer-Verlag, 2009.

[34] S. Gevorgian, A. K. Tagantsev, and A. Vorobiev, “Tuneable Film Bulk Acoustic Wave Resonators,” Springer London, 2013, pp. 1–15.

[35] G. N. Saddik, D. S. Boesch, S. Stemmer, and R. A. York, “Dc electric field tunable bulk acoustic wave solidly mounted resonator using SrTiO3,” *Appl. Phys. Lett.*, vol. 91, no. 4, p. 043501, Jul. 2007.

[36] G. N. Saddik and R. A. York, “An L-section DC electric field switchable bulk acoustic wave solidly mounted resonator filter based on Ba0.5Sr0.5TiO 3,” 2011.

[37] S. Lee and A. Mortazawi, “BAW filter design method based on intrinsically switchable ferroelectric BST FBARs,” in IEEE MTT-S Int. Microw. Symp. Dig., May 22-27, 2016, pp. 1-4.

[38] V. Lee, S. Lee, S. A. Sis, and A. Mortazawi, “Intrinsically Switchable Frequency Reconfigurable Barium Strontium Titanate Resonators and Filters,” *IEEE Trans. on Microw. Theory Techniq.*, vol. 65, no. 9, pp. 3221-3229, May 2017.

[39] S. Lee and A. Mortazawi, "An Intrinsically Switchable Ladder-Type Ferroelectric BST-on-Si Composite FBAR Filter," in *IEEE Trans. on Ultrason., Ferroelectr. Freq. Control*, vol. 63, no. 3, pp. 456-462, March 2016.

[40] M. Zolfagharloo Koohi, S. Lee and A. Mortazawi, "Compact Intrinsically Switchable FBAR Filters Utilizing Ferroelectric BST," in *IEEE Trans. on Ultrason. Ferroelectr. Freq. Control*, vol. 65, no. 8, pp. 1468-1474, Aug. 2018.

[41] M. Z. Koohi and A. Mortazawi, "Intrinsically Switchable Filter Bank Employing Ferroelectric Barium Strontium Titanate," in *IEEE Transactions on Microwave Theory and Techniques*, vol. 66, no. 12, pp. 5501-5507, Dec. 2018.

[42] M. Z. Koohi, S. Nam and A. Mortazawi, "Intrinsically Switchable and Bandwidth Reconfigurable Ferroelectric Bulk Acoustic Wave Filters," *IEEE Trans. Ultrason., Ferroelectr. Freq. Control*, 2019.

[43] M. Z. Koohi, W. Peng and A. Mortazawi, "An Intrinsically Switchable Balanced Ferroelectric FBAR Filter at 2 GHz," *2020 IEEE/MTT-S International Microwave Symposium (IMS)*, Los Angeles, CA, USA, 2020, pp. 131-134.

[44] J. Larson, P. Bradley, S. Wartenberg, and R. Ruby, "Modified butterworth-van dyke circuit for FBAR resonators and automated meas-urement system," IEEE Ultrasonic Symp., pp. 863-868,2000.
[45] T. Jamneala, P. Bradley, U. B. Koelle and A. Chien, "Modified Mason model for bulk acoustic wave resonators," in *IEEE Transactions on Ultrasonics, Ferroelectrics, and Frequency Control*, vol. 55, no. 9, pp. 2025-2029, September 2008.
[46] M.Z. Koohi, "Reconfigurable Bulk Acoustic Wave Resonators and Filters Employing Electric-field-induced Piezoelectricity and Negative Piezoelectricity for 5G", PhD dissertation, the University of Michigan, 2020.
[47] A. Kumar, S. Ketkar, and V. Gurumurthy, (2011). Integration Issues of Barium Strontium Titanate thin Film for Tunable Microwave Applications. *In Ceramic Integration and Joining Technologies*, (2011).
[48] J. Kaitila, "3C-1 Review of Wave Propagation in BAW Thin Film Devices - Progress and Prospects," *2007 IEEE Ultrasonics Symposium Proceedings*, New York, NY, USA, 2007, pp. 120-129.
[49] T. Jamneala, C. Kirkendall, B. Ivira, R. K. Thalhammer, P. Bradley, and R. Ruby, "The main lateral mode approximation of a film bulk acoustic resonator with perfect metal electrodes," *IEEE Transactions on Ultrasonics, Ferroelectrics, and Frequency Control*, vol. 65, no. 9, pp. 1703–1716, 2018.
[50] NXP, "DC-to-DC Boost Converters are changing the Face of Mobile Commerce." www.nxp.com (accessed Dec. 1, 2023).
[51] G. G. Fattinger et al., "Carrier aggregation and its challenges - Or: The golden age for acoustic filters," in IEEE MTT-S International Microwave Symposium Digest, Aug. 2016, vol. 2016-August.
[52] M. Li, M. El-Hakiki, D. Kalim, T-Y. Kim, A. Link, B. Schumann, and R. Aigner "A fully matched LTE-A carrier aggregation quadplexer based on BAW and SAW technologies," in Proc. IEEE Int. Ultrasonics Symp., Sept. 2014, pp. 77–80.
[53] Y. Liu, Y. Cai, Y. Zhang, A. Tovstopyat, S. Liu, and C. Sun, "Materials, design, and characteristics of bulk acoustic wave resonator: A review," Micromachines, vol. 11, no. 7, p. 630, Jun. 2020.
[54] T. Komatsu, K. Hashimoto, T. Omori, and M. Yamaguchi, "Tunable radio-frequency filters using acoustic wave resonators and variable capacitors," *Jpn. J. Appl. Phys*., vol. 49, no. 7, 2010, Art. no. 07HD24.
[55] K. Matsutani et al., "A novel switchable SAW duplexer for band 28," in *IEEE MTT-S Int. Microw. Symp. Dig*., Jun. 2017, pp. 1679–1682.
[56] Ruby, R.; Merchant, P. Micromachined thin film bulk acoustic resonators. In *Proceedings of the IEEE 48th Annual Symposium on Frequency Control*, Boston, MA, USA, 1–3 June 1994; pp. 135–138.
[57] S. Gong and G. Piazza, "Design and Analysis of Lithium–Niobate-Based High Electromechanical Coupling RF-MEMS Resonators for Wideband Filtering," in *IEEE Transactions on Microwave Theory and Techniques*, vol. 61, no. 1, pp. 403-414, Jan. 2013.
[58] D. Psychogiou, R. Gómez-García, R. Loeches-Sánchez and D. Peroulis, "Hybrid Acoustic-Wave-Lumped-Element Resonators (AWLRs) for High- Q Bandpass Filters With Quasi-

Elliptic Frequency Response," in IEEE Transactions on Microwave Theory and Techniques, vol. 63, no. 7, pp. 2233-2244, July 2015.
[59] D. R. Jachowski, "Compact, frequency-agile, absorptive bandstop filters," *IEEE MTT-S International Microwave Symposium Digest*, 2005., Long Beach, CA, USA, 2005, pp. 513-516.
[60] T. R. Billeter, "EPR frequency-selective limiter," *Proc. IEEE*, vol. 56, no. 3, pp. 370–371, Mar. 1968.
[61] A. Wolf and J. Pippin, "A passive parametric limiter," in *IEEE Int. Solid-State Circuits Conf. Dig.*, vol. 3. Feb. 1960, pp. 90–91.
[62] D. Psychogiou, R. Gómez-García, and D. Peroulis, "Single and multiband acoustic-wave-lumped-element-resonator (AWLR) bandpass filters with reconfigurable transfer function," IEEE Trans. Microw. Theory Techn., vol. 64, no. 12, pp. 4394–4404, Dec. 2016.
[63] D. Psychogiou, R. Gómez-García, and D. Peroulis, "Acoustic-wave lumped-element-resonator filters with equi-ripple absorptive stopbands," IEEE Microw. Wireless Compon. Lett., vol. 26, no. 3, pp. 177–179, Mar. 2016.
[64] A. Hagelauer et al., "From Microwave Acoustic Filters to Millimeter-Wave Operation and New Applications," in IEEE Journal of Microwaves, vol. 3, no. 1, pp. 484-508, Jan. 2023.
[65] M. Kadota, F. Yamashita, and S. Tanaka, "9.5 GHz Solidly Mounted Bulk Acoustic Wave Resonator using Third Overtone of Thickness Extension Mode in LiNbO3," *IEEE International Ultrasonics Symposium*, IUS, vol. 2022-October, 2022.
[66] J. Kramer et al., "57 GHz Acoustic Resonator with k2of 7.3 % and Q of 56 in Thin-Film Lithium Niobate," Technical Digest -International Electron Devices Meeting, IEDM, vol. 2022-December, pp. 1641–1644, 2022.
[67] M. Henry, R. Timon, T. Young, C. Nordquist, and B. Griffin, "AlN and ScAlN Contour Mode Resonators for RF Filters," ECS Trans. 77, 23.
[68] Berlincourt, D. A., D. R. Curran, and H. Jaffe, "Piezolelectric and Piezomagnetic Materials and Their Function in Transducers," *Physical Acoustics*, Vol. I-A, ed. W. P. Mason, Academic Press, New York, 1964.
[69] M. G´eradin and D. J. Rixen, "Continuous systems," in *Mechanical vibrations: theory and application to structural dynamics*. John Wiley & Sons, 2014, pp. 211–334.
[70] L. Meirovitch, "Undamped system response," in *Analytical methods in vibrations*, 1967, pp. 274–327.
[71] E. H. Dowell and D. Tang, "Normal forms for kinetic and potential energy," in *Dynamics of very high dimensional systems*. World Scientific, 2003, pp. 55–58.
[72] M. A. Caro, S. Zhang, T. Riekkinen, M. Ylilammi, M. A. Moram, O. Lopez-Acevedo, J. Molarius, and T. Laurila, "Piezoelectric coefficients and spontaneous polarization of ScAlN," Journal of Physics: Condensed Matter, vol. 27, no. 24, p. 245901, 2015.
[73] O. Ambacher, B. Christian, N. Feil, D. Urban, C. Els¨asser, M. Prescher, and L. Kirste, "Wurtzite ScAlN, InAlN, and GaAlN crystals, a comparison of structural, elastic, dielectric, and piezoelectric properties," *J. Appl. Phys.*, vol. 130, no. 4, 2021.
[74] R. Ruby, J. Larson, C. Feng, and S. Fazzio, "The effect of perimeter geometry on fbar resonator electrical performance," in *IEEE MTT-S International Microwave Symposium* Digest, 2005., 2005, pp. 217–220.

[75] G. Fattinger, S. Marksteiner, J. Kaitila, and R. Aigner, “Optimization of acoustic dispersion for high performance thin film baw resonators,” in *IEEE Ultrasonics Symposium*, 2005., vol. 2. IEEE, 2005, pp. 1175–1178.
[76] T. Jamneala, C. Kirkendall, B. Ivira, R. K. Thalhammer, P. Bradley, and R. Ruby, “The main lateral mode approximation of a film bulk acoustic resonator with perfect metal electrodes,” *IEEE Transactions on Ultrasonics, Ferroelectrics, and Frequency Control*, vol. 65, no. 9, pp. 1703–1716, 2018.
[77] R. Pinto, V. Gund, C. Calaza, K.K. Nagaraja, K.B. Vinayakumar, Piezoelectric aluminum nitride thin-films: A review of wet and dry etching techniques, *Microelectron. Eng*. 257, C (Mar 2022).
[78] R. James *et. al*. 2019 *J. Phys.: Conf. Ser.* 1407 012083.
[79] D. Mo, S. Rassay, C. Li, and R. Tabrizian, “Intrinsically switchable dual-band scandium-aluminum nitride lamb-wave filter,” *physica status solidi (RRL)–Rapid Research Letters*, p. 2200135, 2022.
[80] D. Wang, P. Wang, S. Mondal, J. Liu, M. Hu, M. He, S. Nam, W. Peng, S. Yang, D. Wang, Y. Xiao, Y. Wu, A. Mortazawi, and Z. Mi, “Controlled ferroelectric switching in ultrawide bandgap AlN/ScAlN multilayers,” *Applied Physics Letters*, vol. 123, no. 10, p. 103506, 09 2023.
[81] M. L. Kao, Y. K. Liang, Y. Lin, Y. C. Weng, C. F. Dee, P. T. Liu, C. T. Lee, and E. Y. Chang, *Ieee Electr Device L 43* (12), 2105 (2022).
[82] R. Nie, S. Shao, Z. Luo, X. Kang, and T. Wu, “Characterization of Ferroelectric Al0.7Sc0.3N Thin Film on Pt and Mo Electrodes,” *Micromachines*, vol. 13, no. 10, p. 1629, 09 2022.
[83] S. Cho, O. Barrera, P. Simeoni, J. Kramer, V. Chulukhadze, W. Zhao, and R. Lu, “55.4 GHz bulk acoustic resonator in thin-film scandium aluminum nitride,” in *2023 IEEE International Ultrasonics Symposium (IUS)*, 2023, pp. 1–4.
[84] Z. Schaffer, A. Hassanien, M. A. Masud, and G. Piazza, “A solidly mounted 55 GHz overmoded bulk acoustic resonator,” in *2023 IEEE International Ultrasonics Symposium (IUS)*, 2023, pp. 1–4.
[85] Z. Schaffer, P. Simeoni, and G. Piazza, “33 GHz overmoded bulk acoustic resonator,” IEEE *Microw. Wireless Compon. Lett.*, vol. 32, no. 6, pp. 656–659, 2022.
[86] W. Peng, M. Z. Koohi, S. Nam and A. Mortazawi, "Phenomenological Circuit Modeling of Ferroelectric-Driven Bulk Acoustic Wave Resonators," in *IEEE Transactions on Microwave Theory and Techniques*, vol. 70, no. 1, pp. 919-925, Jan. 2022.
[87]] E. R. Crespin et al., “Fully integrated switchable filter banks,” in *IEEE MTT-S Int. Microw. Symp. Dig.*, Jun. 2012, pp. 1–3.
[88] A. Fouladi Azarnaminy and R. R. Mansour, "Switched Dual-Band SAW Filters Using Hybrid and Monolithically Integrated Vanadium Oxide Switches," in *IEEE Transa. on Microw. Theory and Techniq*, vol. 70, no. 1, pp. 876-885, Jan. 2022.
[89] Iriarte, G.F.; Rodriguez, J.; Calle, F.; Gomez, F.C. Synthesis of c-axis oriented AlN thin films on different substrates: A review. *Mater. Res. Bull*. 2010, 45, 1039–1045.

[90] P. Wang, D. A. Laleyan, A. Pandey, Y. Sun, and Z. Mi, “Molecular beam epitaxy and characterization of wurtzite ScxAl1−xN,” *Applied Physics Letters*, vol. 116, no. 15, p. 151903, 2020.

[91] [30] Yasuoka, S., Shimizu, T., Tateyama, A., Uehara, M., Yamada, H., Akiyama, M., Hiranaga, Y., Cho, Y. and Funakubo, H., 2020. “Effects of deposition conditions on the ferroelectric properties of (Al1−xScx)N thin films.” *J. of Appl. Phys.*, 128 (11), p.114103.

[92] D. Wang, P. Wang, S. Mondal, M. T. Hu, D. H. Wang, Y. P. Wu, T. Ma, and Z. T. Mi, "Thickness scaling down to 5 nm of ferroelectric ScAlN on CMOS compatible molybdenum grown by molecular beam epitaxy,"*Applied Physics Letters*, vol. 122, no. 5, p. 052101, 2023.